Hybride elektromagnetische simulatietechnieken
voor het computerondersteund ontwerp van flexibele antennes

Hybrid Electromagnetic Simulation Techniques
for the Computer-Aided Design of Flexible Antennas

Freek Boeykens

Promotor: prof. dr. ir. H. Rogier
Proefschrift ingediend tot het behalen van de graad van
Doctor in de Ingenieurswetenschappen: Elektrotechniek

Vakgroep Informatietechnologie
Voorzitter: prof. dr. ir. D. De Zutter
Faculteit Ingenieurswetenschappen en Architectuur
Academiejaar 2013 - 2014

UNIVERSITEIT
GENT

ISBN 978-90-8578-643-6
NUR 959
Wettelijk depot: D/2013/10.500/76

Hybrid Electromagnetic Simulation Techniques for the Computer-Aided Design of Flexible Antennas

Freek Boeykens

Dissertation submitted to obtain the academic degree of
Doctor of Electrical Engineering

Publicly defended at Ghent University on November 12, 2013

Research funded by a doctoral grant from the Agency for Innovation by Science and Technology in Flanders (IWT).

Supervisor:

prof. dr. ir. H. Rogier
Electromagnetics group
Department of Information Technology
Faculty of Engineering and Architecture
Ghent University
St.-Pietersnieuwstraat 41
B-9000 Ghent, Belgium
`http://emweb.intec.ugent.be`

Members of the examining board:

prof. dr. ir. L. Taerwe (chairman)	Ghent University, Belgium
prof. dr. ir. D. Botteldooren (secretary)	Ghent University, Belgium
prof. dr. ir. H. Rogier (supervisor)	Ghent University, Belgium
prof. dr.-ing. T. Eibert	Technische Universität München, Germany
prof. dr. ir. D. De Zutter	Ghent University, Belgium
prof. dr. ir. L. Dupré	Ghent University, Belgium
dr. ir. J. Sercu	Agilent Technologies, Belgium

Dankwoord

Het is zover! Na vier jaar vertoeven in een gezellig bureautje langs de oevers van de Schelde is er dan toch een einde gekomen aan de periode die in de volksmond ook wel eens een verlengd studentenleven genoemd wordt. Toen ik in de zomer van 2009 mijn doctoraat aanvatte, had ik geen flauw benul van hoe ik er precies aan zou beginnen of hoe ik ooit een boek zou kunnen volschrijven. Gelukkig kon ik hiervoor rekenen op de steun van verschillende personen, zonder wie deze thesis nooit tot stand zou gekomen zijn. Deze mensen wil ik hier dan ook graag bedanken.

Eerst en vooral gaat mijn dank uit naar mijn promotor, Hendrik. Hij wist mij te overtuigen om een doctoraat te beginnen bij de elektromagnetismegroep. Zijn klare kijk en visie hebben het schip van deze garnaalvisser steevast langs de juiste wateren gestuurd zonder daarbij het einddoel uit het zicht te verliezen. Ook bij Dries en Daniël kon ik steeds terecht wanneer ik eens moeilijkheden had met integraalvergelijkingen of het formuleren van wetenschappelijk verantwoorde zinnen. Een speciale dank gaat uit naar Isabelle, het kloppend hart van onze onderzoeksgroep, die mijn administratieve zorgen telkens weer tot het minimum wist te herleiden.

Tijdens mijn onderzoek werkte ik deels met Agilent Technologies samen. Hun eindige elementensolver lag aan de basis van mijn hybride FE-BIE methode en zonder hen zou ik nooit tot dit resultaat gekomen zijn. Jan, Jeannick en Tim, bedankt!

In het Technicum had ik de eer en het genoegen om een bureau te delen met enkele opmerkelijke collega's. Bart, hét Belgisch schaaktalent bij uitstek en voor zover ik weet de enige doctoraatsstudent met een Wikipediapagina (die je blijkbaar enkel mag aanpassen mits correcte bronvermelding), startte zijn onderzoek gelijktijdig met mij en slaagde er moeiteloos in om het vier jaar op ons bureau uit te houden. Wanneer hij eens geen zin had om onvrijwillig slachtoffer te spelen van de nodige office pranks, leerde hij mij enkele kneepjes van het schaakvak zoals penning, dubbele aanval of *en passant*, waarvan de termen alleen al menig vrouwenharten sneller doen slaan. Alessandro vertoefde slechts een half jaar bij ons, maar slaagde er wonderwel in om onze Italiaanse woordenschat naar het volgende niveau te tillen. Zijn vertrek werd ingelost door Mykola. Deze wereldvreemde Oekraïner kan met één enkele zin iedereen verbijsteren, affronteren of huilend doen weglopen. Het zou me sterk verbazen indien ik later ooit nog iemand van dit kaliber tegenkom. Zijn animo en filosofische uitspattingen zorgden evenwel voor de luchtige sfeer en broederschap die stiekem in onze bureau gegroeid is. Bedankt jongens!

Voorts bestaat de altijd veranderende EM-groep uit een bende enthousiaste jongelingen die ik voor het gemak even onderverdeel in de oude en de jonge garde. De oude garde leerde ik kennen toen ik aan mijn onderzoek begon en kon mij steeds uit de nood helpen met IT- of EM-gerelateerde problemen. Ook op conferenties bleken sommige individuen te transformeren in grootse entertainers. De jonge garde werkt momenteel naarstig aan hun eigen onderzoek en zorgt voor de frisse wind die steeds opnieuw in de gang op -T waait. Bedankt collega's voor de oneindige discussies over gitaren, jamsessies op +3, robotcompetities, Pita Wednesdays, International Thursdays, Social Fridays en nog zoveel meer!

Ook mijn ouders wil ik heel graag bedanken. Mama en papa, merci voor de kans die jullie mij geboden hebben om aan de unief te gaan studeren en uiteindelijk op dit punt te kunnen raken. Het is normaal dat jullie mijn luide gitaarmuziek missen sinds ik niet meer thuis woon, maar weet dat de *Sound of Silence* even mooi kan zijn.

In mijn vrije tijd heb ik altijd graag met het juiste gezelschap een pintje verzet, een restaurant bezocht, tegen een squashbal gemept of gewoon luid muziek gespeeld. Anne, Jerre, Wim, Ruben, Quinten, Mohsan, Jørgen, Despa-bende, Shuffled en Sonder, bedankt!

Ik wil ook graag jou, lezer, bedanken om eens in dit boek te snuisteren. Laat je niet afschrikken door de formules of vreemde symbolen en blader gerust eens verder dan deze eerste twee pagina's. De Poincaré-Steklov operator is trouwens de perfecte aanrader voor het slapengaan.

Tot slot wil ik me richten tot die ene persoon rond wie het voor mij allemaal draait. Stefanie, mijn schat, we hebben al veel leuke momenten beleefd. Van een Metallica-concert in Lissabon tot het kwijtspelen van ons huurbootje in Kroatië. Bedankt om er altijd voor mij te zijn, mij te steunen in wat ik doe en het (al dan niet met wat tegenzin) strijken van mijn hemden voor conferenties, doctoraatsverdedigingen en andere deftige aangelegenheden... Met jou is het altijd feest in huis en ik kijk al uit naar ons volgend avontuur in juli!

Gent, oktober 2013
Freek Boeykens

Knowledge speaks, but wisdom listens.

Jimi Hendrix

Contents

Samenvatting

Recent onderzoek heeft geleid tot een nieuwe generatie planaire antennes die flexibel zijn en conform kunnen worden gemaakt aan allerhande oppervlakken zonder verlies aan antenneprestatie. Dergelijke antennes worden vaak onopvallend geïntegreerd in verschillende devices en worden steeds dichter bij mekaar of bij elektronica geplaatst waardoor er vaak ongewenste interactie optreedt. Om deze antennes snel en nauwkeurig te kunnen ontwerpen is zogenaamde 2.5-dimensionale (2.5D) simulatiesoftware ideaal. Dergelijke software brengt het vlakgelaagd karakter van het antennesubstraat zeer efficiënt in rekening zonder een volledige 3D-discretisatie te vergen. Deze simulatoren hebben echter sterke beperkingen. Zo laten ze niet toe om buigingen of het eindige karakter van een substraat mee in rekening te brengen. Ook de aanwezigheid van objecten in het reactieve nabije veld, zoals het object waarop de antenne wordt aangebracht, met name het menselijk lichaam, een wagen, een vliegtuig, een meer uitgebreid elektronisch systeem ..., kan slechts zeer benaderend worden meegenomen. Bij het onopvallend integreren van deze antennes kunnen ook de lagen die de antenne bedekken slechts op zeer benaderende wijze worden gemodelleerd. Hierdoor worden deze antennes op dit moment ontworpen in een geïdealiseerde toestand, waarna een prototype wordt gefabriceerd dat vervolgens wordt getest in niet-ideale omstandigheden. Dit leidt vaak tot herontwerp of het overspecificeren van de ontwerpcriteria.

Als antwoord op de vernoemde beperkingen van de 2.5D-simulatiesoftware wordt in het eerste deel van deze thesis onderzocht hoe het antenneontwerp kan worden uitgebreid aan de hand van metingen en analytische modellen. Het a posteriori verifiëren van de antenneprestaties in realistische omstandigheden via metingen wordt gedemonstreerd aan de hand van het ontwerp van een intra-vehicle antenne die in het dashboard van een wagen moet worden geïntegreerd. Om de ideale positie van de antenne in het dashboard te kunnen bepalen, wordt het dashboard nagebootst door verschillende lagen op de antenne te plaatsen en de hele module opnieuw door te meten.

Het uitbreiden van de 2.5D-simulatiesoftware aan de hand van analytische modellen wordt uitgewerkt voor gebogen antennes, meer bepaald voor flexibele antennes die cilindrisch gebogen worden. Dit komt voor in situaties waarbij een textielantenne gedragen wordt op een arm of een been. Er wordt daarom een cilindrisch caviteitsmodel opgesteld, dat de antenneprestaties modelleert als functie van de buigingsstraal. De resonantiefrequentie voor een bepaalde buigingsstraal kan dan berekend worden door de dispersierelatie van het caviteitsmodel numeriek op te lossen, terwijl de verre-veldpatronen analytisch bekomen worden in gesloten vorm. Het voordeel van deze methode is dat ze snel en accuraat tot een

resultaat leidt, zonder dat het probleem daarvoor eerst moet worden gediscretiseerd. Dit is immers wel het geval voor numerieke simulatiesoftware. Typisch voor dergelijke flexibele antennes is ook de compressie die de antennesubstraten ondervinden als ze gebogen worden. Dit wordt in rekening gebracht door de permittiviteit van het substraat als functie van de buigingsstraal aan te passen. Hierbij wordt bovendien een onderscheid gemaakt tussen antennes met een rekbare en een niet-rekbare patch.

Het cilindrisch caviteitsmodel wordt vervolgens verder uitgebreid voor situaties waar de buigingsstraal stochastisch kan variëren, maar waarvoor een statistische distributie gekend is of gefit kan worden. Dit is bijvoorbeeld het geval voor textielantennes die op de armen van mensen met verschillende lichaamsafmetingen geïmplementeerd worden. Aan de hand van een techniek die gebaseerd is op een veralgemeende polynomiale chaosexpansie is het dan mogelijk de waarschijnlijkheidsdistributie van de resonantiefrequentie te bepalen, vertrekkende van de distributie van de buigingsstraal van de arm. Hierbij moet de dispersierelatie van het analytisch model slechts enkele keren doorgerekend worden, in tegenstelling tot een naïeve Monte Carlo techniek, waarbij aan de hand van een groot aantal simulaties een statistische distributie benaderd wordt.

In het tweede deel van deze thesis verschuift de focus naar het rigoureus modelleren aan de hand van de Maxwellvergelijkingen van de antennes samen met meer algemene, complexere structuren ingebed in de vrije ruimte. Om ook de eindige dimensies van de substraten in rekening te brengen richten we ons op 3D-numerieke technieken als verbetering t.o.v de 2.5D-simulatiesoftware. Algemeen kunnen we stellen dat er twee grote numerieke technieken bestaan om dergelijke antennes computerondersteund te ontwerpen in het frequentiedomein (hier worden de antennekarakteristieken berekend in functie van de frequentie). Deze zijn de eindige elementen (FE) methode en de randintegraalvergelijkingsmethode (BIE). De FE-methode discretiseert het simulatiedomein in kleine elementen en berekent dan de lokale elektromagnetische interacties tussen deze elementen. Dit heeft als voordeel dat inhomogene materialen gemakkelijk gemodelleerd kunnen worden, maar als nadeel dat een stelsel met een zeer groot aantal onbekenden moet opgelost worden. Ook wordt het simulatiedomein getrunceerd, aangezien het onmogelijk is om de volledige 3D-ruimte te discretiseren. De BIE-methode lost de elektromagnetische interacties eerst gedeeltelijk analytisch op om zo de dimensies van het probleem met één te verlagen. Het voordeel van deze aanpak is dat enkel de randen van objecten moeten gediscretiseerd worden en dat nu wel de volledige open vrije ruimte kan gemodelleerd worden. De nadelen aan deze methode zijn enerzijds dat dit enkel werkt voor configuraties waarvoor een Greense functie analytisch beschikbaar is, zoals homogene materialen, en anderzijds dat de interacties nu globaal worden berekend, wat leidt tot een dichtbezette systeemmatrix.

Een oplossing voor de problemen van de FE- en de BIE-methode bestaat erin deze twee technieken te combineren in één hybride FE-BIE formulering. Hierbij wordt

elke techniek toegepast in de domeinen waar ze het efficiëntst zijn om zo de computationele vereisten te minimaliseren. Dergelijke hybride methode wordt ontwikkeld in het tweede deel van deze thesis, met als bijkomende voorwaarde dat de FE- en BIE-simulatiedomeinen volledig ontkoppeld moeten zijn. Dit wil zeggen dat ze onafhankelijk van elkaar moeten kunnen gediscretiseerd worden en dat andere types basisfuncties moeten kunnen aangewend worden. Aan de hand van snelle multipooltechnieken kunnen de BIE-interacties bovendien ook versneld worden, zodat de 3D hybride FE-BIE techniek competitief wordt met de 2.5D-simulatiesoftware. De correctheid en enkele eigenschappen van de hybride methode worden gedemonstreerd aan de hand van numerieke voorbeelden.

Een probleem bij zulke hybride formuleringen is dat de oplossing niet altijd uniek bepaald is. Bij bepaalde frequenties is het mogelijk dat er interne resonanties optreden, waardoor ongewenste parasitaire oplossingen het eindresultaat verstoren. Dit is een gekend probleem in de literatuur, maar werd in 3D nog nooit fundamenteel theoretisch onderzocht. Daarom is er ook onderzoek verricht naar de stabiliteit van verschillende hybride FE-BIE methodes op operatorniveau. Door de identificatie van een Poincaré-Steklov (PS) of Dirichlet-to-Neumann (DtN) operator in zowel de FE- als BIE-methode kan er theoretisch worden aangetoond welke formuleringen vrij zijn van dergelijke interne resonanties en welke niet. Bovendien is het mogelijk om voor eenvoudige structuren te voorspellen bij welke frequenties deze resonanties kunnen voorkomen. De theorie wordt daarna gestaafd aan de hand van numerieke voorbeelden.

Summary

Recent research has led to a new generation planar antennas, which are flexible and can be made conformal to different surfaces without loss in performance. Such antennas are unobtrusively integrated into different devices and are placed closer and closer to each other and to electronics, leading to undesirable interactions. In order to design these antennas efficiently and accurately, so-called 2.5-dimensional (2.5D) simulation software is most suited, since those tools allow modelling multi-layered planar surfaces without requiring a full 3D discretisation. However, such simulators have strong limitations. They do not allow bending the antenna, nor taking into account the finite dimensions of a substrate. Also, the presence of objects in the reactive near field, such as the object on which the antenna is deployed, being the human body, a car, an airplane, a more comprehensive electronic system ..., can only very approximately be included. When integrating such antennas unobtrusively, the layers that cover the antenna are also modelled in a very approximate fashion. Therefore, up to now, these antennas are designed in an idealised state, after which a prototype is produced that is subsequently tested in non-ideal conditions. This eventually leads to a redesign of the antenna or overspecification of the design criteria.

In the first part of this thesis, it is therefore investigated how the antenna design via 2.5D simulation software can be extended by means of measurements and analytical models. Via the design of an intra-vehicle antenna that is specifically implemented for integration into the dashboard of a car, we demonstrate how a posteriori measurements validate the antenna performance in realistic conditions. In order to determine the ideal position of the antenna in the dashboard, the dashboard is imitated by placing different layers onto the antenna and the whole module is remeasured.

The extension of 2.5D simulation software by means of analytical models is elaborated for bent antennas, and more specifically for flexible antennas that are cylindrically bent. This occurs in situations where a textile antenna is deployed on an arm or a leg. A cylindrical cavity model is therefore developed as a function of the bending radius and the resonance frequencies as a function of the bending radius are obtained by numerically solving the cavity's dispersion relations, while the far field patterns are given in closed-form expressions. The advantage of such a method is that it quickly leads to an accurate result, without first discretising the problem (which is required for numerical simulation software). Typical for such flexible antennas is that they also undergo compression when bent. This is accounted for by adapting the permittivity of the substrate as a function of the bending radius. A distinction between antennas with a stretchable and a non-stretchable patch is made.

The cylindrical cavity model is further expanded for situations where the bending radius can fluctuate stochastically, but where a statistical distribution of the radius is known or can be fitted, which is, for example, the case when textile antennas are deployed on persons with different body morphologies. By means of a technique based on a generalised polynomial chaos expansion it then becomes possible to determine the probability distribution of the resonance frequency, given the distribution of the bending radius. In this formalism, the dispersion relation of the cavity model is solved only a few times, in contrast to a brute-force Monte Carlo technique, where the statistical distribution is approximated by performing a large number of simulations.

The second part of this thesis focuses on modelling antennas together with more general, complex structures in the free space in a rigorous manner using the Maxwell equations. In order to also take into account the finite dimensions of the substrates, we focus on 3D numerical techniques as an improvement over 2.5D simulation software. In general, two major numerical techniques are considered for the computer-aided design of such antennas in the frequency domain (where the antenna characteristics are computed as a function of frequency), i.e. the finite element (FE) method and the boundary integral equation (BIE) method. The FE method discretises the simulation domain into small elements and computes local electromagnetic interactions between these elements. The benefit of this approach is that inhomogeneous materials are easily modelled, but the drawback is that a matrix system with a huge number of unknowns needs to be solved. The simulation domain is also truncated, as it is impossible to discretise the full 3D space. The BIE method first solves the Maxwell equations partially analytically in order to reduce the dimensions of the problem with one. The asset of this technique is that it implicitly takes into account the full open space and that only the boundaries of objects need to be discretised. The disadvantages are that this approach only works for configurations for which an analytic expression of the Green's function is known, such as homogeneous materials, and that the boundary elements now interact globally, hence resulting in a dense system matrix.

A solution to the drawbacks of the FE and BIE methods is to combine these two techniques into one hybrid FE-BIE formulation, where each method is employed in the domains where it is the most efficient, thereby minimising the computational requirements. Such a hybrid method is developed in the second part of this thesis, with an extra condition that the FE and BIE simulation domains have to be completely decoupled. This means that they may be discretised independently and may rely on different types of basis functions. By means of fast multipole techniques it is possible to accelerate the computation of the BIE interactions, which makes the 3D hybrid FE-BIE method competitive with the 2.5D simulation software. The accuracy and some properties of the hybrid method are demonstrated by means of numerical examples.

A problem occurring in such hybrid formulations is that the solution is not always uniquely defined. It is possible that, at certain frequencies, internal resonances oc-

cur that lead to spurious solutions. This is a well-known problem in literature, but it was never rigorously theoretically investigated in 3D. Therefore, research was performed on the stability of different hybrid FE-BIE methods at an operator level. By identifying a Poincaré-Steklov (PS) or Dirichlet-to-Neumann (DtN) operator in both the FE and BIE method, it can theoretically be proven which formulations are free of such internal resonances and which are not. Moreover, it becomes possible for simple structures to predict the frequencies at which these resonances occur. Finally, the theory is also verified by means of numerical examples.

List of Abbreviations

2.5D	Two-and-a-half-dimensional
3D	Three-dimensional
AR	Axial Ratio
BC	Buffa-Christiansen
BiCGSTAB	Biconjugate Gradient Stabilised
BIE	Boundary Integral Equation
CDF	Cumulative Distribution Function
CFIE	Combined Field Integral Equation
DtN	Dirichlet-to-Neumann
EFF	Electric Field Formulation
EFIE	Electric Field Integral Equation
EM	Electromagnetic
FDTD	Finite Difference Time Domain
FE	Finite Element
FMM	Fast Multipole Method
ISM	Industrial, Scientific and Medical
MFIE	Magnetic Field Integral Equation
MLFMA	Multilevel Fast Multipole Algorithm
NHANES	National Health and Nutrition Examination Survey
PDF	Probability Distribution Function
PEC	Perfect Electric Conductor
PMC	Perfect Magnetic Conductor
PMCHWT	Poggio-Miller-Chang-Harrington-Wu-Tsai
PS	Poincaré-Steklov
RCS	Radar Cross Section
RWG	Rao-Wilton-Glisson
TFQMR	Transpose Free Quasi Minimal Residual

List of Symbols

Mathematical symbols

j	imaginary unit
∇	nabla operator
$\Re$	real part
$\Im$	imaginary part
$\lvert\cdot\rvert$	magnitude
$\lVert\cdot\rVert$	Euclidean norm
$\cdot^T$	matrix transpose
$\cdot^*$	complex conjugate
$\mathbf{x}$	a vector
$\overline{\overline{x}}$	a tensor

Electromagnetic symbols

$\mathbf{E}$	electric field
$\mathbf{H}$	magnetic field
$\mathbf{D}$	electric induction
$\mathbf{B}$	magnetic induction
$\mathbf{J}$	electric current density
$\mathbf{K}$	magnetic current density
ρ	electric charge density
κ	magnetic charge density
t	time
f	frequency
ω	pulsation
k	wavenumber
λ	wavelength
ϵ	permittivity
μ	permeability

Special functions

$J_n(\cdot)$	n-th order Bessel function of the first kind
$Y_n(\cdot)$	n-th order Bessel function of the second kind
$H_n^{(2)}(\cdot)$	n-th order Hankel function of the second kind

Operators

$\mathcal{S}$	Schur complement
$\mathcal{Y}$	Poincaré-Steklov operator
$\mathcal{T},\mathcal{K},\mathcal{U}$	BIE operators
$\mathcal{P}$	Calderón operator
$\mathcal{I}$	identity operator
$\mathcal{N}$	$\mathbf{n}\times$ operator

List of Publications

Articles in International Journals

- F. Boeykens, H. Rogier and L. Vallozzi, "An efficient technique based on polynomial chaos to model the uncertainty in the resonance frequency of textile antennas due to bending", submitted for publication in *IEEE Transactions on Antennas and Propagation*.
- F. Boeykens, H. Rogier, J. Van Hese, J. Sercu and T. Boonen, "Rigorous analysis of internal resonances in 3D hybrid FE-BIE formulations by means of the Poincaré-Steklov operator", *IEEE Transactions on Microwave Theory and Techniques*, vol. 61, no. 10, pp. 3503–3513, Oct. 2013.
- F. Boeykens, L. Vallozzi and H. Rogier, "Cylindrical bending of deformable textile rectangular patch antennas", *International Journal of Antennas and Propagation*, vol. 2012, Article ID 170420, 11 pages, 2012.
- F. Boeykens, Q. Doolaege, F. Declercq and H. Rogier, "A planar aperture-coupled patch antenna implemented on dashboard foams for intra-vehicle communication", *Microwave and Optical Technology Letters*, vol. 53, no. 5, pp. 1186–1189, May 2011.

Articles in Conference Proceedings

- F. Boeykens, H. Rogier, J. Van Hese, J. Sercu and T. Boonen, "Efficient calculation of coupling matrices for a decoupled FE/BIE formulation", *2012 International Conference on Electromagnetics in Advanced Applications (ICEAA)*, 2-7 September 2012.
- W. Dullaert, H. Rogier and F. Boeykens, "Advantages of PSWF-based models for UWB systems", *2012 International Conference on Electromagnetics in Advanced Applications (ICEAA)*, 2-7 September 2012.
- F. Boeykens, Q. Doolaege, F. Declercq and H. Rogier, "Optimal topology for an intra-vehicle antenna implemented on dashboard foams", *2011 IEEE International Symposium on Antennas and Propagation (APSURSI)*, pp. 453–456, 3-8 July 2011.

Hybrid Electromagnetic Simulation Techniques for the Computer-Aided Design of Flexible Antennas

Introduction

Wireless communication has become ubiquitous in our daily life. Calling via smartphones, navigating with GPS or connecting a laptop to a wireless network are all based on the same principle: to transmit information wirelessly through space between a sender and a receiver. An electric signal is thereby transformed by an antenna at the transmitter into a radiating electromagnetic wave that propagates through space at the speed of light and that is eventually transformed back into an electric signal by the antenna of the receiver.

Depending on the application, different antennas are employed. As an example, consider the two types of antennas shown in Fig. 1. In Fig. 1(a) a parabolic satellite communications antenna is demonstrated. This type of antenna is designed to transmit a highly directive signal to a satellite of which the location is known, whereas Fig. 1(b) displays the internal antenna of a mobile phone, designed to fit in the casing of the phone and to transmit a non-directive signal to a cell phone tower at an unknown location. The antennas of Fig. 1 are typically designed by means of numerical simulators that rely on computational electromagnetics, i.e. they model the interactions of electromagnetic fields with physical objects and the environment. These interactions are computed from a set of equations, described by Maxwell in the 1860s and now (logically) known as the Maxwell equations, providing the necessary relations between electric and magnetic fields, generated by currents and charges.

(a) (b)

Figure 1: A parabolic satellite communications antenna at Erdfunkstelle Raisting, the biggest facility for satellite communication in the world, in Raisting, Bavaria, Germany (a) and the antenna of a Nokia 8810, the first mobile phone to have an internal antenna.

There exist various numerical techniques to solve the Maxwell equations both in time domain, where the behaviour of electromagnetic fields is calculated as a function of time, and in frequency domain, where the interactions are computed as a function of frequency. In this thesis, we focus on solving the Maxwell equations in the frequency domain and we consider two major approaches:

- The **Finite Element** (FE) **method** on the one hand discretises the simulation domain into small elements and computes local interactions between these elements. The benefit of this approach is that inhomogeneous materials are easily modelled and that a sparse system matrix is obtained. The drawbacks are the huge number of unknowns and the truncation of the simulation domain (as it is impossible to discretise the full 3D space).
- The **Boundary Integral Equation** (BIE) **method** on the other hand first solves the Maxwell equations partially analytically in order to reduce the dimensions of the problem by one. The asset of this technique is that it implicitly takes into account the full open space and that only the boundaries of objects need to be discretised, leading to much less unknowns in comparison with the FE method. The disadvantages are that this approach only works for homogeneous materials and that the boundary elements now interact globally, hence resulting in a dense system matrix.

None of the two methods can be seen as the *better* one over the other, because their performance always depends on the problem that is simulated. This can again be illustrated by the antennas of Fig. 1. One could best apply the BIE method for designing the parabolic antenna, as it is constructed using homogeneous materials and electric conductors, whereas the FE method would be more appropriate for the mobile phone antenna, because not only the antenna will have to be modelled, but also the casing of the phone and the electric circuits in it.

In this thesis, we will focus on the design of a new generation of planar antennas, which are flexible and conformal to different surfaces. An example is demonstrated in Fig. 2 [1]. Such antennas are unobtrusively integrated into different devices and are placed closer and closer to each other and to electronics, leading to undesirable interactions. In order to design these antennas, so-called 2.5-dimensional (2.5D) BIE simulation tools are ideal, since they allow modelling multi-layered planar surfaces without requiring a full 3D discretisation. However, these tools suffer from several drawbacks:

- They do not take into account the finite dimensions of the substrates since they assume that the surfaces have an infinite extent.
- It is difficult to incorporate other objects in the reactive near field, e.g. the human body, a car, an electronic system ...
- It is not possible to compute the behaviour of antennas in bent state.

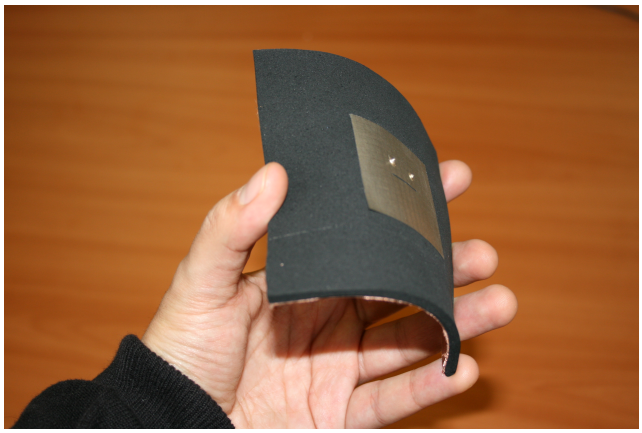

Figure 2: A flexible planar antenna.

As a result, such antennas are simulated in an idealised environment, causing discrepancies between simulation and measurement results. This eventually leads to a redesign of the antenna or overspecification of the design criteria.

The motivation of this thesis is therefore to provide solutions for these problems. This is done in twofold. First, the 2.5D simulation tools can be complemented by a posteriori measurements to validate the antenna performance in realistic conditions and by analytical models in order to describe the behaviour of bent antennas. This is tackled in Part I. Second, in order to take into account the finite dimensions and other objects, a 3D hybrid FE-BIE method is developed in Part II. This method combines the 3D FE and 3D BIE method in order to apply each method where it is most efficient.

Outline of this work

In Chapter 1 the reader is provided with the necessary background knowledge. The Maxwell equations are introduced and some typical electromagnetic (EM) concepts are explained. For a comprehensive analysis of electromagnetism, we refer to [2], [3].

In Part I, we focus on the problems of 2.5D simulation tools. Chapter 2 presents the design of a planar antenna for intra-vehicle communication using 2.5D simulation software. This antenna has to be integrated into a dashboard and therefore non-ideal effects due to the integration of the antenna are investigated by means of a measurement campaign. In Chapter 3, we provide analytical expressions for computing the resonance frequency and the radiation pattern of bent textile antennas. By calculating the Maxwell equations in cylindrical coordinates and by taking into account the effect of compression, a good agreement between simula-

tions and measurements is obtained. This model is further expanded in Chapter 4 for situations where the bending radius can fluctuate, but where a statistical distribution of the radius is known (or can be fitted). By applying the technique of generalised polynomial chaos, it becomes possible to predict the distribution of the resonance frequency.

In Part II, a 3D non-conformal hybrid FE-BIE method is developed. Therefore, we start in Chapter 5 by introducing the individual FE and BIE methods and derive their formulations from the Maxwell equations. Chapter 6 then discusses the hybrid formulation with two different boundary conditions. By means of numerical examples, different properties are explained. Finally in Chapter 7, the stability of different hybrid FE-BIE formulations is investigated by introducing the concept of a Poincaré-Steklov operator. This approach allows us to theoretically prove the existence of internal resonances in some FE-BIE combinations. Both conformal and non-conformal formulations are investigated and the theory is then applied to a scattering problem.

References

[1] P. Van Torre, L. Vallozzi, A. Dierck, H. Rogier, and M. Moeneclaey, "Power-efficient body-centric communications", in *URSI Benelux Forum 2012, Proceedings*, 2012, pp. 8–10.

[2] R. Harrington, *Time-Harmonic Electromagnetic Fields*. New York, US: McGraw-Hill, 1961.

[3] J. G. Van Bladel, *Electromagnetic Fields*, 2nd, D. G. Dudley, Ed. John Wiley and Sons, Inc., 2007.

1 Electromagnetic Theory

★ ★ ★

In this chapter, basic electromagnetic theory is derived from the Maxwell equations. The scalar and vector potentials are defined, which can then be solved analytically in Chapter 3 or numerically via the BIE method in Chapter 5. Also some key properties such as field equivalence, reciprocity and energy conservation are described. These are necessary for the derivation of the hybrid FE-BIE system in Chapter 6.

1.1 The Maxwell equations

The Maxwell equations describe the behaviour of the electric field $\mathbf{E}$ [V/m], the magnetic field $\mathbf{H}$ [A/m], the electric induction $\mathbf{D}$ [C/m^2] and the magnetic induction $\mathbf{B}$ [Wb/m^2] due to an electric current density $\mathbf{J}$ [A/m^2], a magnetic current density $\mathbf{K}$ [V/m^2], an electric charge density ρ [C/m^3] and a magnetic charge density κ [Wb/m^3]. In the frequency domain and at a certain location $\mathbf{r}$, they are given by [1]

$$\nabla \times \mathbf{E}(\mathbf{r}) = -j\omega\mathbf{B}(\mathbf{r}) - \mathbf{K}(\mathbf{r}), \tag{1.1a}$$

$$\nabla \times \mathbf{H}(\mathbf{r}) = j\omega\mathbf{D}(\mathbf{r}) + \mathbf{J}(\mathbf{r}), \tag{1.1b}$$

$$\nabla \cdot \mathbf{D}(\mathbf{r}) = \rho(\mathbf{r}), \tag{1.1c}$$

$$\nabla \cdot \mathbf{B}(\mathbf{r}) = \kappa(\mathbf{r}). \tag{1.1d}$$

This form assumes all entities to be time harmonic, meaning that they all vary sinusoidally. The time-dependent solution can be derived from

$$\mathbf{F}(\mathbf{r}, t) = \mathbf{F}(\mathbf{r})e^{j\omega t}, \tag{1.2}$$

with $\omega = 2\pi f$ the pulsation of the sinusoidal variation and f the frequency.

From the Maxwell equations (1.1), the laws of charge conservation can be derived, which denote that the charge and current densities are not independent from each other:

$$\nabla \cdot \mathbf{J}(\mathbf{r}) + j\omega\rho(\mathbf{r}) = 0, \tag{1.3a}$$
$$\nabla \cdot \mathbf{K}(\mathbf{r}) + j\omega\kappa(\mathbf{r}) = 0. \tag{1.3b}$$

In order to solve an electromagnetic problem, the Maxwell equations (1.1) are not sufficient. We still need some relations between the fields **E** and **H** on the one hand and the inductions **D** and **B** on the other hand. These relations are called the constitutive equations:

$$\mathbf{D}(\mathbf{r}) = \overline{\overline{\epsilon}}(\mathbf{r}) \cdot \mathbf{E}(\mathbf{r}), \tag{1.4a}$$
$$\mathbf{B}(\mathbf{r}) = \overline{\overline{\mu}}(\mathbf{r}) \cdot \mathbf{H}(\mathbf{r}). \tag{1.4b}$$

Here, $\overline{\overline{\epsilon}}(\mathbf{r})$ and $\overline{\overline{\mu}}(\mathbf{r})$ denote the permittivity and the permeability tensors, respectively. In this thesis, only isotropic media are considered, meaning that the tensors can be replaced by scalars ($\overline{\overline{\epsilon}}(\mathbf{r}) = \epsilon$ and $\overline{\overline{\mu}}(\mathbf{r}) = \mu$).

At the interface between two different materials, the fields are no longer continuous and certain boundary conditions must be fulfilled. These boundary conditions can be derived from the Maxwell equations (1.1). At an interface S between two materials 1 and 2, one obtains:

$$\mathbf{n} \times \left(\mathbf{E}_2 - \mathbf{E}_1\right) = -\mathbf{K}_S, \tag{1.5a}$$
$$\mathbf{n} \times \left(\mathbf{H}_2 - \mathbf{H}_1\right) = \mathbf{J}_S, \tag{1.5b}$$
$$\mathbf{n} \cdot \left(\mathbf{D}_2 - \mathbf{D}_1\right) = \rho_S, \tag{1.5c}$$
$$\mathbf{n} \cdot \left(\mathbf{B}_2 - \mathbf{B}_1\right) = \kappa_S, \tag{1.5d}$$

with $\mathbf{K}_S$ and $\mathbf{J}_S$ the magnetic and electric surface current densities, ρ_S and κ_S the electric and magnetic charge densities, and **n** the normal to the interface pointing into material 2.

The boundary condition for open domains is the so-called Sommerfeld radiation condition, which states that energy radiated from sources cannot scatter back from infinity. For an isotropic medium with permittivity ϵ and permeability μ, this means that in any direction (θ, ϕ) of the unit vector $\mathbf{u}_r$ (in a spherical coordinate system), the radiation fields must satisfy [2]

$$\lim_{r\to\infty} \mathbf{u}_r \times \mathbf{H} + \frac{1}{\eta}\mathbf{E} = \mathbf{0},$$
$$\lim_{r\to\infty} \mathbf{u}_r \times \mathbf{E} - \eta\mathbf{H} = \mathbf{0},$$

with the wave impedance being $\eta = \sqrt{\mu/\epsilon}$.

1.2 Scalar and vector potentials

When solving the linear Maxwell equations (1.1), the technique of superposition can be applied. This means that one can solve the equations once with only electric sources, once with only magnetic sources and then combine both solutions. The solution for only electric or magnetic sources can be written in terms of scalar and vector potentials, which are solutions of Helmholtz equations [2], [3].

1.2.1 Electric sources

When only considering electric current and charge densities as excitations, the Maxwell equations (1.1) become

$$\nabla \times \mathbf{E}(\mathbf{r}) = -j\omega\mathbf{B}(\mathbf{r}), \tag{1.6a}$$

$$\nabla \times \mathbf{H}(\mathbf{r}) = j\omega\mathbf{D}(\mathbf{r}) + \mathbf{J}(\mathbf{r}), \tag{1.6b}$$

$$\nabla \cdot \mathbf{D}(\mathbf{r}) = \rho(\mathbf{r}), \tag{1.6c}$$

$$\nabla \cdot \mathbf{B}(\mathbf{r}) = 0. \tag{1.6d}$$

The zero divergence of the magnetic induction in (1.6d) implies the existence of a vector potential $\mathbf{A}(\mathbf{r})$, such that

$$\frac{1}{\mu}\mathbf{B}(\mathbf{r}) = \nabla \times \mathbf{A}(\mathbf{r}), \tag{1.7}$$

since the divergence of the curl of any vector field is always zero. Remark that this vector potential is normally introduced for the magnetic induction without the factor $1/\mu$, but here we follow the convention used in [3]. Substitution of (1.7) in (1.6a) then yields

$$\nabla \times \big(\mathbf{E}(\mathbf{r}) + j\omega\mu\mathbf{A}(\mathbf{r})\big) = \mathbf{0}. \tag{1.8}$$

This, in turn, implies the existence of a scalar potential $\phi(\mathbf{r})$, defined by

$$\nabla\phi(\mathbf{r}) = -\mathbf{E}(\mathbf{r}) - j\omega\mu\mathbf{A}(\mathbf{r}), \tag{1.9}$$

because the curl of the gradient of any scalar field is always zero.

Expressions for the electric induction and the magnetic field follow from the constitutive equations (1.4). We get

$$\mathbf{D}(\mathbf{r}) = -j\omega\epsilon\mu\mathbf{A}(\mathbf{r}) - \epsilon\nabla\phi(\mathbf{r}), \tag{1.10a}$$

$$\mathbf{H}(\mathbf{r}) = \nabla \times \mathbf{A}(\mathbf{r}). \tag{1.10b}$$

In order to define the potentials $\mathbf{A}(\mathbf{r})$ and $\phi(\mathbf{r})$, we substitute (1.10) into (1.6b) and (1.6c). This leads to

$$\nabla^2\mathbf{A}(\mathbf{r}) + k^2\mathbf{A}(\mathbf{r}) - \nabla\big(\nabla \cdot \mathbf{A}(\mathbf{r}) + j\omega\epsilon\phi(\mathbf{r})\big) = -\mathbf{J}(\mathbf{r}), \tag{1.11a}$$

$$\nabla^2\phi(\mathbf{r}) + k^2\phi(\mathbf{r}) + j\omega\mu\big(\nabla \cdot \mathbf{A}(\mathbf{r}) + j\omega\epsilon\phi(\mathbf{r})\big) = -\frac{1}{\epsilon}\rho(\mathbf{r}), \tag{1.11b}$$

with the wave number being $k = \omega\sqrt{\epsilon\mu}$. Since $\mathbf{A}(\mathbf{r})$ and $\phi(\mathbf{r})$ are not uniquely defined, an additional restriction can be imposed. Here, we apply the Lorentz gauge

$$\nabla \cdot \mathbf{A}(\mathbf{r}) + j\omega\epsilon\phi(\mathbf{r}) = 0. \tag{1.12}$$

Then (1.11a) and (1.11b) become the following Helmholtz equations

$$\nabla^2\mathbf{A}(\mathbf{r}) + k^2\mathbf{A}(\mathbf{r}) = -\mathbf{J}(\mathbf{r}), \tag{1.13a}$$

$$\nabla^2\phi(\mathbf{r}) + k^2\phi(\mathbf{r}) = -\frac{1}{\epsilon}\rho(\mathbf{r}). \tag{1.13b}$$

1.2.2 Magnetic sources

When only considering magnetic current and charge densities as excitations, the Maxwell equations (1.1) become

$$\nabla \times \mathbf{E}(\mathbf{r}) = -j\omega\mathbf{B}(\mathbf{r}) - \mathbf{K}(\mathbf{r}), \tag{1.14a}$$

$$\nabla \times \mathbf{H}(\mathbf{r}) = j\omega\mathbf{D}(\mathbf{r}), \tag{1.14b}$$

$$\nabla \cdot \mathbf{D}(\mathbf{r}) = 0, \tag{1.14c}$$

$$\nabla \cdot \mathbf{B}(\mathbf{r}) = \kappa(\mathbf{r}). \tag{1.14d}$$

Now the zero divergence of the electric induction (1.14c) implies the existence of a vector potential $\mathbf{F}(\mathbf{r})$, such that

$$\frac{1}{\epsilon}\mathbf{D}(\mathbf{r}) = -\nabla \times \mathbf{F}(\mathbf{r}). \tag{1.15}$$

The minus sign in (1.15) is introduced to keep the formulas more symmetric. Substitution of (1.15) in (1.14b) then yields

$$\nabla \times \big(\mathbf{H}(\mathbf{r}) + j\omega\epsilon\mathbf{F}(\mathbf{r})\big) = \mathbf{0}. \tag{1.16}$$

Again, this implies the existence of a scalar potential $\psi(\mathbf{r})$, such that

$$\nabla\psi(\mathbf{r}) = -\mathbf{H}(\mathbf{r}) - j\omega\epsilon\mathbf{F}(\mathbf{r}). \tag{1.17}$$

The magnetic induction and the electric field are derived from the constitutive equations (1.4). We get

$$\mathbf{B}(\mathbf{r}) = -j\omega\epsilon\mu\mathbf{F}(\mathbf{r}) - \mu\nabla\psi(\mathbf{r}), \tag{1.18a}$$

$$\mathbf{E}(\mathbf{r}) = -\nabla \times \mathbf{F}(\mathbf{r}). \tag{1.18b}$$

In order to determine the potentials $\mathbf{F}(\mathbf{r})$ and $\psi(\mathbf{r})$, the equations of (1.18) are substituted into (1.14a) and (1.14d). This leads to

$$\nabla^2\mathbf{F}(\mathbf{r}) + k^2\mathbf{F}(\mathbf{r}) - \nabla\big(\nabla \cdot \mathbf{F}(\mathbf{r}) + j\omega\mu\psi(\mathbf{r})\big) = -\mathbf{K}(\mathbf{r}), \tag{1.19a}$$

$$\nabla^2\psi(\mathbf{r}) + k^2\psi(\mathbf{r}) + j\omega\epsilon\big(\nabla \cdot \mathbf{F}(\mathbf{r}) + j\omega\mu\psi(\mathbf{r})\big) = -\frac{1}{\mu}\kappa(\mathbf{r}). \tag{1.19b}$$

Similar as for electric sources, the potentials $\mathbf{F}(\mathbf{r})$ and $\psi(\mathbf{r})$ are not uniquely defined, so the Lorentz gauge can be applied

$$\nabla \cdot \mathbf{F}(\mathbf{r}) + j\omega\mu\psi(\mathbf{r}) = 0. \tag{1.20}$$

Then (1.19a) and (1.19b) become the following Helmholtz equations

$$\nabla^2\mathbf{F}(\mathbf{r}) + k^2\mathbf{F}(\mathbf{r}) = -\mathbf{K}(\mathbf{r}), \tag{1.21a}$$

$$\nabla^2\psi(\mathbf{r}) + k^2\psi(\mathbf{r}) = -\frac{1}{\mu}\kappa(\mathbf{r}). \tag{1.21b}$$

1.2.3 Total fields

With the use of the potentials defined in Section 1.2.1 and Section 1.2.2, the electric and magnetic field in the presence of both electric and magnetic sources can be computed. Applying superposition leads to

$$\mathbf{E}(\mathbf{r}) = -\nabla \times \mathbf{F}(\mathbf{r}) - j\omega\mu\mathbf{A}(\mathbf{r}) - \nabla\phi(\mathbf{r}), \tag{1.22a}$$

$$\mathbf{H}(\mathbf{r}) = \nabla \times \mathbf{A}(\mathbf{r}) - j\omega\epsilon\mathbf{F}(\mathbf{r}) - \nabla\psi(\mathbf{r}). \tag{1.22b}$$

The electric and magnetic field can also be determined from the vector potentials only. Inserting the Lorentz gauges (1.12) and (1.20) into (1.22) yields

$$\mathbf{E}(\mathbf{r}) = -\nabla \times \mathbf{F}(\mathbf{r}) - j\omega\mu\mathbf{A}(\mathbf{r}) + \frac{1}{j\omega\epsilon}\nabla\left(\nabla \cdot \mathbf{A}(\mathbf{r})\right), \tag{1.23a}$$

$$\mathbf{H}(\mathbf{r}) = \nabla \times \mathbf{A}(\mathbf{r}) - j\omega\epsilon\mathbf{F}(\mathbf{r}) + \frac{1}{j\omega\mu}\nabla\left(\nabla \cdot \mathbf{F}(\mathbf{r})\right). \tag{1.23b}$$

1.3 The equivalence theorem

The equivalence theorem allows to construct new solutions of the Maxwell equations, starting from a given solution. In this section, we discuss the equivalence theorem of Love [4], which allows to construct integral kernels in the BIE formulation. It is a consequence of the uniqueness property of electromagnetic fields and of the source equivalence principle. Therefore, these are described here first.

Consider the configuration of Fig. 1.1(a) where the sources $\mathbf{J}_1$, $\mathbf{K}_1$, $\mathbf{J}_2$ and $\mathbf{K}_2$ generate an electromagnetic field $(\mathbf{E}, \mathbf{H})$. A volume V, with boundary ∂V, is also defined and encloses the sources $\mathbf{J}_1$ and $\mathbf{K}_1$. The uniqueness property and the radiation condition then state that the field $(\mathbf{E}, \mathbf{H})$ is the *only* solution of the Maxwell equations, given these sources. This can be proven by assuming that there are two possible solutions $(\mathbf{E}_1, \mathbf{H}_1)$ and $(\mathbf{E}_2, \mathbf{H}_2)$ which eventually have to be equal [3], [5]. It can also be demonstrated that it is sufficient to know the tangential components of $\mathbf{E}$ and $\mathbf{H}$ on ∂V in order to uniquely determine the field inside V [6], [7].

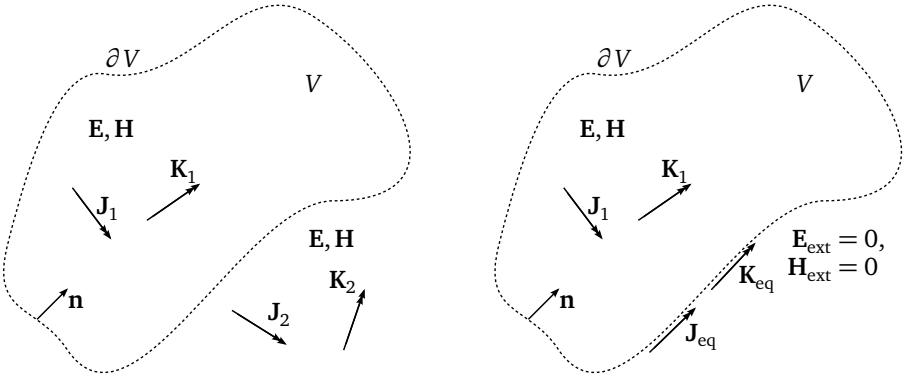

Figure 1.1: The sources $\mathbf{J}_1$, $\mathbf{K}_1$, $\mathbf{J}_2$ and $\mathbf{K}_2$ generate a unique electromagnetic field $(\mathbf{E}, \mathbf{H})$ (a). In order to find the same field inside V, the sources $\mathbf{J}_2$ and $\mathbf{K}_2$ can be replaced by the equivalent Huygens sources $\mathbf{J}_{\text{eq}}$ and $\mathbf{K}_{\text{eq}}$ (b) on the boundary ∂V.

Hence, it is clear that two different fields always require two different sources. However, the reverse is not true, i.e. there may well be different sources that give rise to the same field inside V. Such sources are then called equivalent with respect to V. This is demonstrated in Fig. 1.1(b), where the field in V is generated by a contribution of the original sources $\mathbf{J}_1$ and $\mathbf{K}_1$ and a contribution of equivalent sources on ∂V, which represent the effect of $\mathbf{J}_2$ and $\mathbf{K}_2$. These equivalent sources are defined by

$$\mathbf{J}_{\text{eq}} = \mathbf{n} \times \mathbf{H}, \tag{1.24a}$$

$$\mathbf{K}_{\text{eq}} = \mathbf{E} \times \mathbf{n}, \tag{1.24b}$$

and they correspond to the Huygens sources. Inside V we then find the unique solution $(\mathbf{E}, \mathbf{H})$ and outside V we obtain a zero field, which means that $\mathbf{J}_{\text{eq}}$ and $\mathbf{K}_{\text{eq}}$ are non-radiating sources. This also follows from the boundary conditions (1.5a) and (1.5b):

$$\mathbf{n} \times \left(\mathbf{E} - \mathbf{E}_{\text{ext}}\right) = -\mathbf{K}_{\text{eq}}, \tag{1.25a}$$

$$\mathbf{n} \times \left(\mathbf{H} - \mathbf{H}_{\text{ext}}\right) = \mathbf{J}_{\text{eq}}, \tag{1.25b}$$

resulting in $\mathbf{E}_{\text{ext}} = 0$ and $\mathbf{H}_{\text{ext}} = 0$ in the complete space outside V by invoking the uniqueness theorem. Therefore, one is allowed to omit the original materials outside V and add new materials in order to simplify the original problem. This is the main idea behind the field equivalence theorem of Love, where the outside materials are replaced by a homogeneous isotropic medium with permittivity ϵ_{ext} and permeability μ_{ext}. This is beneficial if the inner domain is also filled with a homogeneous material. One can then choose the outer and inner materials to be

equal and create a full homogeneous space. This allows us to construct a Green's function (see Chapter 5), that can be used in a BIE formulation.

1.4 Reciprocity

In its simplest sense, a reciprocity theorem states that a response of a system to a source is unchanged when source and measurer are interchanged [3]. Its properties are pioneered by H.A. Lorentz [8] and play a fundamental role in electromagnetic theory.

Assume there are two separate source distributions, $(\mathbf{J}_1, \mathbf{K}_1)$ and $(\mathbf{J}_2, \mathbf{K}_2)$ in a medium. The fields produced by these sources are $(\mathbf{E}_1, \mathbf{H}_1)$ and $(\mathbf{E}_2, \mathbf{H}_2)$, respectively. The Maxwell curl equations (1.1a) and (1.1b), together with the constitutive equations (1.4) then imply

$$\nabla \times \mathbf{E}_1 = -j\omega\mu\mathbf{H}_1 - \mathbf{K}_1, \tag{1.26a}$$
$$\nabla \times \mathbf{H}_1 = j\omega\epsilon\mathbf{E}_1 + \mathbf{J}_1, \tag{1.26b}$$
$$\nabla \times \mathbf{E}_2 = -j\omega\mu\mathbf{H}_2 - \mathbf{K}_2, \tag{1.26c}$$
$$\nabla \times \mathbf{H}_2 = j\omega\epsilon\mathbf{E}_2 + \mathbf{J}_2, . \tag{1.26d}$$

Now, we calculate

$$\nabla \cdot \left(\mathbf{E}_1 \times \mathbf{H}_2\right) = -j\omega\mu\mathbf{H}_2 \cdot \mathbf{H}_1 - \mathbf{H}_2 \cdot \mathbf{K}_1 - j\omega\epsilon\mathbf{E}_1 \cdot \mathbf{E}_2 - \mathbf{E}_1 \cdot \mathbf{J}_2, \tag{1.27}$$
$$\nabla \cdot \left(\mathbf{E}_2 \times \mathbf{H}_1\right) = -j\omega\mu\mathbf{H}_1 \cdot \mathbf{H}_2 - \mathbf{H}_1 \cdot \mathbf{K}_2 - j\omega\epsilon\mathbf{E}_2 \cdot \mathbf{E}_1 - \mathbf{E}_2 \cdot \mathbf{J}_1. \tag{1.28}$$

Subtracting the last two equations results in:

$$\nabla \cdot \left(\mathbf{E}_1 \times \mathbf{H}_2 - \mathbf{E}_2 \times \mathbf{H}_1\right) = \mathbf{H}_1 \cdot \mathbf{K}_2 - \mathbf{H}_2 \cdot \mathbf{K}_1 + \mathbf{E}_2 \cdot \mathbf{J}_1 - \mathbf{E}_1 \cdot \mathbf{J}_2. \tag{1.29}$$

After integration over a volume V with surface S, this becomes:

$$\oint_S \left(\mathbf{E}_1 \times \mathbf{H}_2 - \mathbf{E}_2 \times \mathbf{H}_1\right) \cdot \mathbf{n} \, \mathrm{d}S = \int_V \mathbf{H}_1 \cdot \mathbf{K}_2 - \mathbf{H}_2 \cdot \mathbf{K}_1 + \mathbf{E}_2 \cdot \mathbf{J}_1 - \mathbf{E}_1 \cdot \mathbf{J}_2 \, \mathrm{d}V. \tag{1.30}$$

If the integration domain V is the entire space, the surface integral is cancelled out thanks to the radiation condition and we obtain the reciprocity theorem:

$$\int_V \mathbf{E}_1 \cdot \mathbf{J}_2 - \mathbf{H}_1 \cdot \mathbf{K}_2 \, \mathrm{d}V = \int_V \mathbf{E}_2 \cdot \mathbf{J}_1 - \mathbf{H}_2 \cdot \mathbf{K}_1 \, \mathrm{d}V. \tag{1.31}$$

1.5 Energy conservation at an interface

Define the Poynting vector $\mathbf{S}$ as

$$\mathbf{S} = \frac{1}{2}\left(\mathbf{E} \times \mathbf{H}^*\right). \tag{1.32}$$

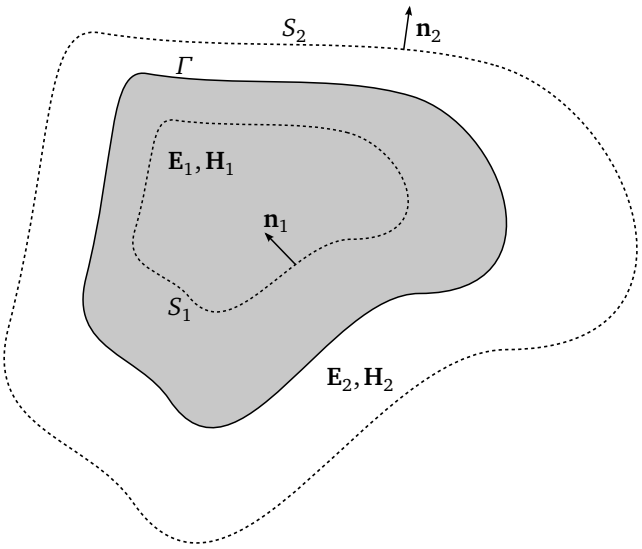

Figure 1.2: The field $(\mathbf{E}_1, \mathbf{H}_1)$ inside a material and field $(\mathbf{E}_2, \mathbf{H}_2)$ outside the material respect the law of energy conservation at the interface Γ.

The integral of this vector over a surface then represents the time-averaged complex power flux through this surface [9]. Now, consider the configuration of Fig. 1.2. In a material, with boundary Γ, a field $(\mathbf{E}_1, \mathbf{H}_1)$ exists. Outside the material we have the field $(\mathbf{E}_2, \mathbf{H}_2)$. A volume V can now be created, that encloses Γ and is bounded by the two surfaces S_1 and S_2. The outward normal on the boundary $S_1 \cup S_2$ of V is $\mathbf{n}$, which is equal to $\mathbf{n}_1$ on S_1 and $\mathbf{n}_2$ on S_2. From the divergence theorem, the outward power flux $P_\mathbf{S}$ can then be written as:

$$P_\mathbf{S} = \frac{1}{2} \oint_{S_1 \bigcup S_2} \left(\mathbf{E} \times \mathbf{H}^*\right) \cdot \mathbf{n} \, \mathrm{d}S = \frac{1}{2} \int_V \nabla \cdot \left(\mathbf{E} \times \mathbf{H}^*\right) \, \mathrm{d}V. \tag{1.33}$$

Given the fields $(\mathbf{E}_1, \mathbf{H}_1)$ in the first domain and $(\mathbf{E}_2, \mathbf{H}_2)$ in the second domain, (1.33) becomes

$$P_\mathbf{S} = \frac{1}{2} \oint_{S_1} \left(\mathbf{E}_1 \times \mathbf{H}_1^*\right) \cdot \mathbf{n}_1 \, \mathrm{d}S + \frac{1}{2} \oint_{S_2} \left(\mathbf{E}_2 \times \mathbf{H}_2^*\right) \cdot \mathbf{n}_2 \, \mathrm{d}S = \frac{1}{2} \int_V \nabla \cdot \left(\mathbf{E} \times \mathbf{H}^*\right) \, \mathrm{d}V, \tag{1.34}$$

with $\mathbf{n}_i$ the outward normal of S_i. Now let the volume go to zero, then S_1 and S_2 go to the boundary Γ and the law of energy conservation states:

$$\oint_{S_1} \left(\mathbf{E}_1 \times \mathbf{H}_1^*\right) \cdot \mathbf{n}_1 \, \mathrm{d}S + \oint_{S_2} \left(\mathbf{E}_2 \times \mathbf{H}_2^*\right) \cdot \mathbf{n}_2 \, \mathrm{d}S = 0. \tag{1.35}$$

This means that the total power flux passing through Γ is identical on both sides of the interface and thus no power is dissipated in Γ.

References

[1] J. C. Maxwell, *A Treatise on Electricity and Magnetism*. Oxford: Clarendon Press, 1973.

[2] J. G. Van Bladel, *Electromagnetic Fields*, 2nd, D. G. Dudley, Ed. John Wiley and Sons, Inc., 2007.

[3] R. Harrington, *Time-Harmonic Electromagnetic Fields*. New York, US: McGraw-Hill, 1961.

[4] A. Love, "The integration of the equations of propagation of electric waves", *Phil. Trans. Roy. Soc. London, Ser. A*, vol. 197, pp. 1–45, 1901.

[5] Q. Chu and C. Liang, "The uniqueness theorem of electromagnetic fields in lossless regions", *IEEE Trans. Antennas Propag.*, vol. 41, no. 2, pp. 245–246, Feb. 1993.

[6] I. V. Lindell, *Methods for Electromagnetic Field Analysis*, D. G. Dudley, Ed. Oxford University Press, 1992.

[7] H. Rogier, "Numerical solution of maxwell's equations by combining finite elements or finite differences with integral equations", PhD thesis, Ghent University, 1998.

[8] H. Lorentz, "The theorem of Poynting concerning the energy in the electromagnetic field and two general propositions concerning the propagation of light", *Amsterdammer Akademie der Wetenschappen*, vol. 4, p. 176, 1896.

[9] J. Poynting, "On the transfer of energy in the electromagnetic field", *Phil. Trans. Roy. Soc. London*, vol. 175, pp. 343–361, 1884.

Part I

Advanced Antenna Design

2

A Planar Aperture-Coupled Patch Antenna Implemented on Dashboard Foams for Intra-Vehicle Communication

Freek Boeykens, Quinten Doolaege, Frederick Declercq and Hendrik Rogier

Published in Microwave and Optical Technology Letters

★ ★ ★

A robust low-profile aperture-coupled quasi-circularly polarised patch antenna was designed for intra-vehicle communication in the unlicensed 2.45 GHz ISM band (2.4 GHz - 2.485 GHz). Since dashboards offer a large platform for invisible integration, the antenna is implemented using materials compatible with the production process of dashboards. This also allows easy, invisible and low-cost integration inside a car's dashboard. A measured gain of 6.437 dBi and nearly circular polarisation were obtained with the antenna covered by the different dashboard layers.

2.1 Introduction

There is a growing interest towards integration of wireless networks in vehicles for intra-vehicle, vehicle-to-vehicle and vehicle-to-roadside communication. The purpose of these new technologies is to increase the safety on the road and to share several types of information. Some examples are Forward Collision Warning, Green Light Optimal Speed Advisory and Remote Diagnostics [1]. We focus on intra-vehicle communication and introduce hereby the concept of the Cable Free Car. Within this concept it becomes possible to connect certain wireless devices such as PDAs and GSMs to a central infotainment console of the car. These wireless connections use protocols such as Bluetooth, Wifi and Zigbee that operate in the unlicensed 2.45 GHz ISM band (2.4 GHz - 2.485 GHz). This requires an antenna for the console that has to be unobtrusively and invisibly integrated in the vehicle. The best location for integration is in the dashboard, with the main lobe of the antenna's radiation pattern towards the centre of the car [2], [3].

Integration of an antenna into the dashboard has already been attempted in the past, but with rigid materials as substrates and a via for connecting different layers [4]. This approach suffers from several disadvantages such as the extra effort needed for incorporating the non-flexible antenna in the flexible dashboard and the use of a via, making the antenna vulnerable to pressure, shock and vibration. Therefore we present, for the first time in literature, the design of a patch antenna using flexible foams compatible with the production process of dashboards, suitable for this type of integration. The use of vias is avoided by relying on aperture coupling as a feed technique. The antenna is quasi-circularly polarised to minimise the effect of polarisation mismatch between a device and the antenna. In this case, the device doesn't have to be oriented along a certain direction to obtain an optimal communication link.

The organisation of this chapter is as follows. Section 2.2 describes the antenna topology, the material selection and the design. In Section 2.3, the simulated and measured return loss and axial ratio are presented. Section 2.4 describes the integration of the antenna into a dashboard and also presents the measured return loss and axial ratio for different configurations. The conclusions are drawn in Section 2.5.

2.2 Antenna topology and design

2.2.1 Antenna topology

The antenna must have a planar low-profile structure for easy integration in the dashboard. This leads to the use of patch antennas, which are also light in weight, compact and easy to fabricate in mass production. It also has to be shock and stress resistant, so the use of vias connecting different layers should be avoided. For this reason an aperture-coupled feeding structure is proposed, which has the

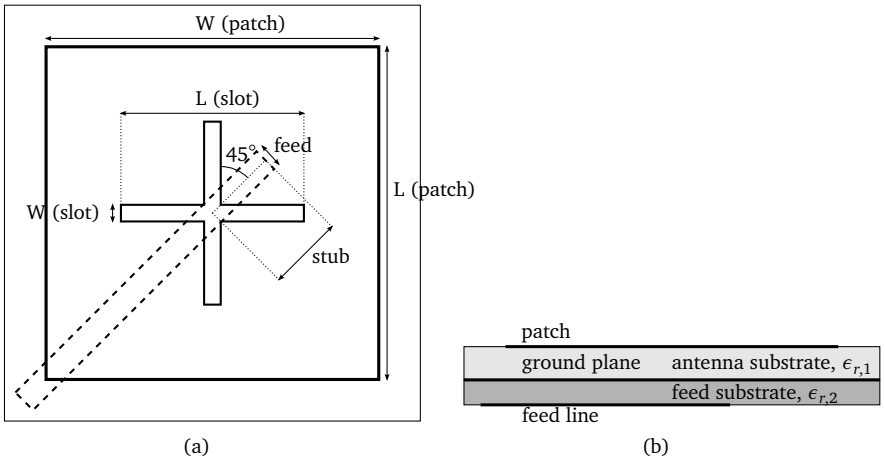

Figure 2.1: Topology A: top view (a) and side view (b).

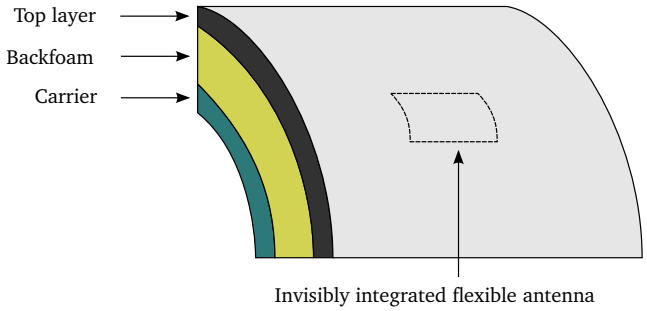

Figure 2.2: Layout of a dashboard

extra advantage of allowing the use of different materials as feed and antenna substrate, minimising back radiation [5]. Moreover, an active circuit may easily be integrated onto the feed substrate. The realised antenna topology is shown in Fig. 2.1. It consists of a nearly-square patch, a crossed slot and a feed line placed along the diagonal of the cross. Quasi-circular polarisation is obtained by the excitation of two orthogonal modes in the crossed slot [6], [7].

2.2.2 Integration in the dashboard

First, a sensitivity analysis was performed to check the influence of the alignment of the different layers on the quasi-circular polarisation. The alignment appeared to be crucial and hence, the best solution is to integrate the antenna as a separate module in the dashboard, which consists of three layers: a carrier, a backfoam and a top layer, as demonstrated in Fig. 2.2 [8]. This leads to two possible configura-

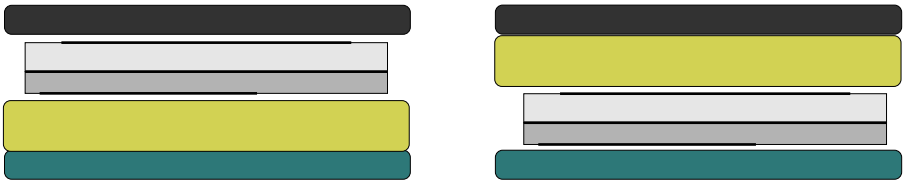

(a) (b)

Figure 2.3: Two possible schemes for integrating the antenna in the dashboard. Integration between the backfoam and the top layer (a) and integration between the carrier and the backfoam (b).

Table 2.1: Possible substrates for the antenna.

Type foam	Description	ϵ_r	$\tan\delta$
1	Aromatic polyurethane	2.55	0.07
2	Aliphatic polyurethane	2.59	0.08
3	Two-layer complex aromatic + aliphatic polyurethane	2.53	0.065
4	Aromatic polyurethane with blown air bubbles	1.45	0.03
5	Aromatic polyurethane with blown air bubbles	1.12	0.01

tions for the integration. In a first configuration, the module is placed between the backfoam and the top layer, so only the top layer covers the antenna. In a second configuration, the module is integrated between the carrier and the backfoam, so both the backfoam and the top layer are on top of the antenna. These two integration schemes are shown in Fig. 2.7. Both configurations were tested and are discussed further in this chapter.

2.2.3 Material selection

As depicted in Fig. 2.1, the aperture-coupled patch antenna consists of an antenna substrate and a feed substrate. The feed substrate is preferably thin with a high relative permittivity ϵ_r, whereas the antenna substrate must have a low ϵ_r [9], [10]. In order to find the right materials for these substrates, we were provided by Recticel® with some flexible materials typically used in the production process for dashboards. Their material parameters were determined using the measurement method described in [11] and are shown in Table 2.1. All substrates are polyurethane based foams, but only type 4 and 5 have encapsulated air bubbles, providing a low ϵ_r. These substrates are also open-cell foams, which means that the pores are connected, keeping a good flexibility. Types 1, 2 and 3 are closed-

Table 2.2: Optimised parameters of the intra-vehicle antenna.

Parameter	Size [mm]
Patch ($L \times W$)	50.1×45.2
Slot ($L \times W$)	21.8×2.2
Stub	6.17
Feed	2.8

cell foams, which means that the pores are not connected, resulting in a denser polyurethane substrate providing a high ϵ_r. The chosen substrates are type 5 as antenna substrate and type 3 as feed substrate. The choice for the feed substrate was also determined by the loss tangent, because the relative permittivity of the first three types are almost equal. The feed substrate has a thickness of 1 mm and the antenna substrate has a thickness of 5.1 mm.

The antenna patch, feed line and ground plane are etched copper layers on a very thin polyimide carrier.

2.2.4 Antenna design

The design was carried out by imposing design criteria for the reflection coefficient (S_{11}) and the axial ratio (AR) in the 2.45 GHz ISM band:

$$S_{11} < -10\,\text{dB}, \tag{2.1}$$

$$\text{AR} < 3\,\text{dB}. \tag{2.2}$$

The 2.5D full-wave field simulator ADS Momentum® was used for the optimisation. The optimised parameters are shown in Table 2.2.

2.3 Simulations and measurements in open space

After fabrication, a measurement of the reflection coefficient was performed using an HP8510C network analyser. The comparison between the simulated and measured reflection coefficient is shown in Fig. 2.4. The simulated bandwidth is 385 MHz and the measured bandwidth is 435 MHz. The entire 2.45 GHz ISM band is covered.

The axial ratio as a function of the frequency was obtained by means of a transmission measurement in an anechoic chamber. The resulting curve, for the broadside direction, is shown in Fig. 2.5. One observes a shift of the curve towards lower frequencies. The centre frequency is 2.41 GHz and the AR-bandwidth is about

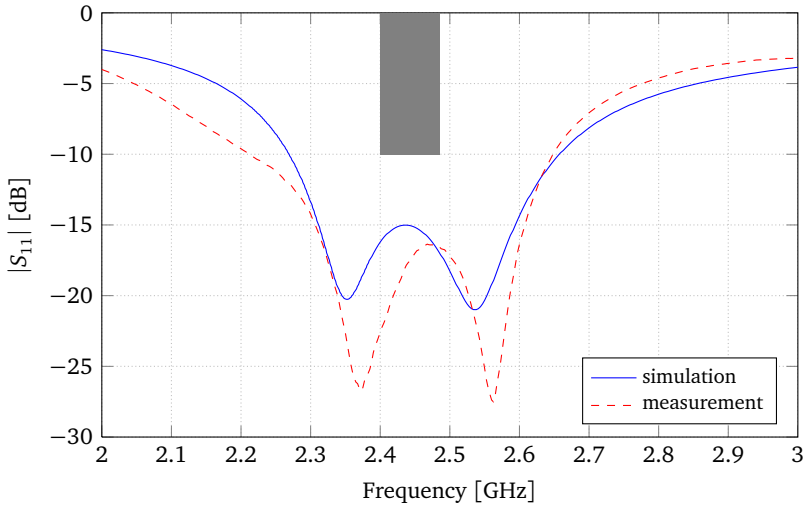

Figure 2.4: Simulated and measured reflection coefficient for the antenna in open space.

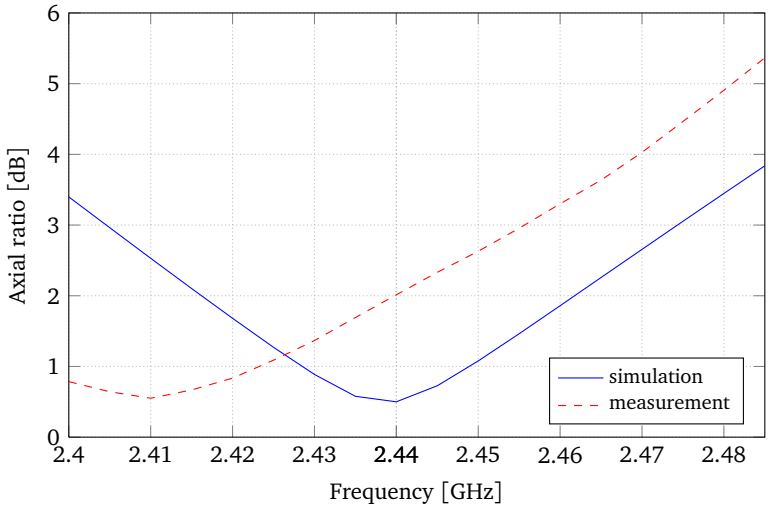

Figure 2.5: Simulated and measured axial ratio for the antenna in open space.

85 MHz. As can be seen in Fig. 2.5, the antenna is not fully circularly polarised in the entire 2.45 GHz ISM band, but this is not an absolute requirement as quasi-circular polarisation is only used to minimise the polarisation mismatch between transmitter and receiver.

The fabricated antenna exhibits a measured radiation efficiency of 64.3% and the

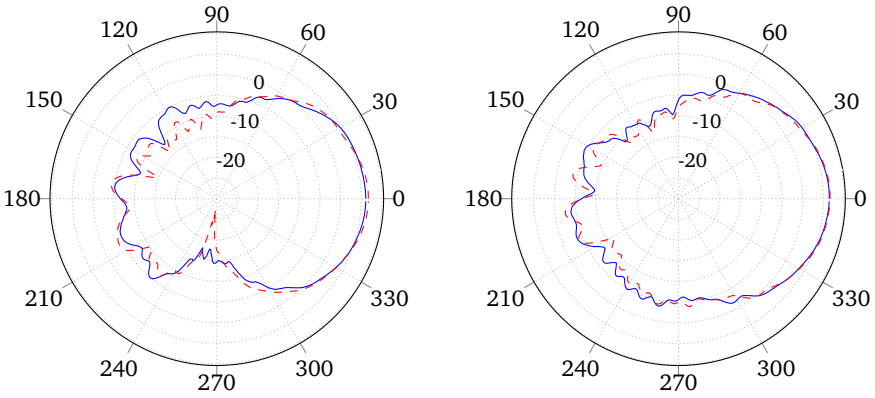

(a) (b)

Figure 2.6: Radiation pattern in the xz-plane (a) and the yz-plane (b). The radiation pattern in open space is given by the dashed line, whereas the radiation pattern for the antenna placed between the carrier and the backfoam is plotted by the solid line.

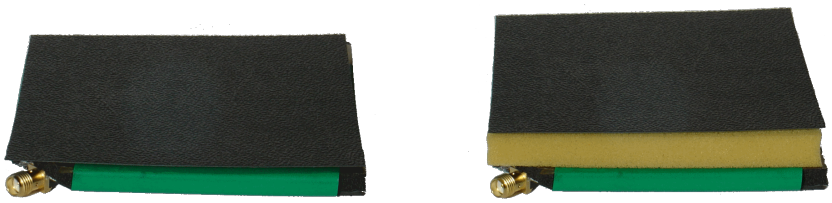

(a) (b)

Figure 2.7: Picture of the antenna in configuration a (a) and configuration b (b).

maximal gain is 6.714 dBi. The 3 dB beam width is 62° in both the xz-plane and yz-plane and the forward/backward ratio is 14 dB. The radiation patterns in the xz-plane and the yz-plane are shown in Fig. 2.6.

2.4 Simulations and measurements in the car

As mentioned before, there are two possible configurations for integrating the antenna into a vehicle's dashboard. These two configurations were tested by means of covering the antenna with the appropriate layers provided by Recticel®, as shown in Fig. 2.7.

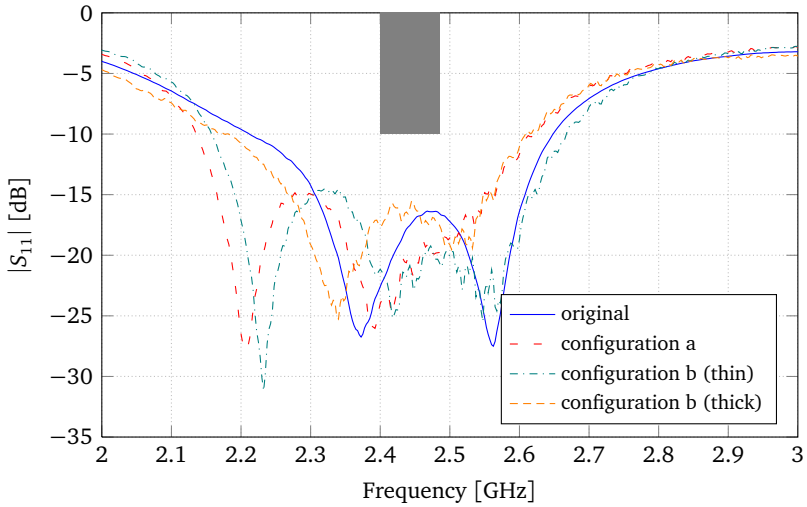

Figure 2.8: Measured reflection coefficient for the antenna in open space and in the different configurations. Configuration a has only the top layer on the antenna, whereas configuration b has both the top layer and the backfoam on the antenna.

2.4.1 Integration between the backfoam and the top layer

This configuration was imitated by placing the top layer on the antenna. The measured reflection coefficient, compared to the return loss in open space, can be seen in Fig. 2.8. One notices a -10 dB bandwidth of 480 MHz with the 2.45 GHz ISM still entirely covered.

The measured axial ratio in broadside direction is shown in Fig. 2.9. The curve has shifted towards lower frequencies and there is no circular polarisation anymore in the ISM band.

This configuration clearly affects the antenna characteristics too much and hence will not be a good solution.

2.4.2 Integration between the carrier and the backfoam

The integration between the carrier and the backfoam was imitated by placing both the backfoam and the top layer on the antenna. We were provided with backfoams of different thicknesses, so we did measurements with the thickest (9.12 mm) and the thinnest (4.37 mm) ones.

The measured reflection coefficient is shown in Fig. 2.8 and one notices that both configurations cover the entire ISM band. The configuration with the thinnest

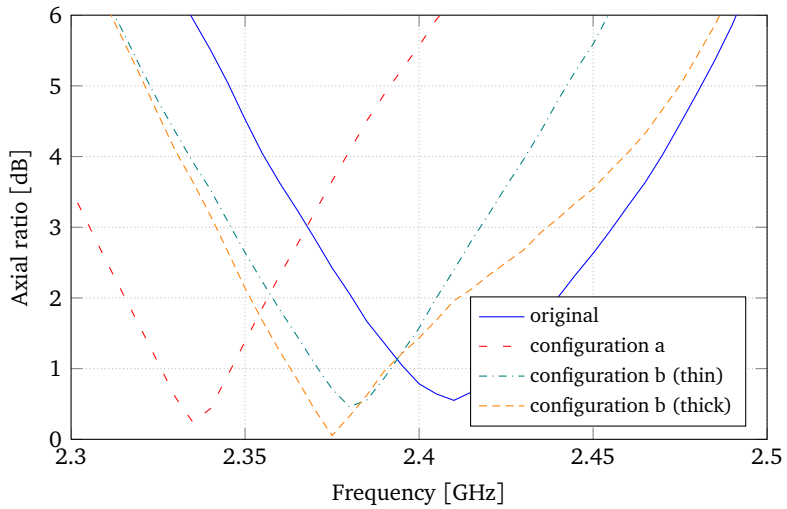

Figure 2.9: Measured axial ratio for the antenna in open space and in the different configurations. Configuration a has only the top layer on the antenna, whereas configuration b has both the top layer and the backfoam on the antenna.

backfoam has a -10 dB bandwidth of 505 MHz, the other one a bandwidth of 425 MHz.

Fig. 2.9 shows the measured axial ratio in broadside direction. The curve is the least affected in the configuration with the thickest backfoam. One notices that the antenna is quasi-circularly polarised in the ISM band.

The configuration with the thickest backfoam exhibits a measured radiation efficiency of 63.7% and the maximal gain is 6.437 dBi. The 3 dB beam width is 68° in both the xz-plane and yz-plane and the forward/backward ratio is 13 dB. The radiation patterns in the xz-plane and the yz-plane are shown in Fig. 2.6.

2.4.3 Comparison between the two configurations

The configuration with the antenna integrated between the carrier and the backfoam leads to the best results. The dense top layer affects the characteristics the most, so this layer has to be as far away from the antenna as possible. This can be done by placing the backfoam in between the antenna and the top layer. This backfoam acts as an air gap and will not have a large influence on the antenna characteristics.

2.5 Conclusion

The proposed antenna is capable of covering the entire 2.45 GHz ISM band (spanning 2.4 GHz - 2.485 GHz). Also the requirement for quasi-circular polarisation has been fulfilled.

When integrating the antenna into a dashboard, there is only a small deterioration in antenna characteristics if the antenna is integrated between the carrier and the backfoam. This demonstrates the feasibility of invisibly integrating the antenna into the dashboard of a vehicle.

References

[1] (Aug. 2007). C2C-CC manifesto, Car to car communication consortium, [Online]. Available: http://www.car-to-car.org/.

[2] H.-M. Tsai, C. Saraydar, T. Talty, M. Ames, A. Macdonald, and O. Tonguz, "Zigbee-based intra-car wireless sensor network", in *Communications, 2007. ICC '07. IEEE International Conference on*, 2007, pp. 3965–3971.

[3] R. de Francisco, L. Huang, G. Dolmans, and H. de Groot, "Coexistence of zigbee wireless sensor networks and bluetooth inside a vehicle", in *Personal, Indoor and Mobile Radio Communications, 2009 IEEE 20th International Symposium on*, 2009, pp. 2700–2704.

[4] K. Yegin, "Instrument panel mount GPS antenna", *Microwave and Optical Technology Letters*, vol. 49, no. 8, pp. 1979–1981, Aug. 2007.

[5] D. Pozar, "Microstrip antenna aperture-coupled to a microstripline", *Electronics Letters*, vol. 21, no. 2, pp. 49–50, Jan. 1985.

[6] T. Vlasits, E. Korolkiewicz, A. Sambell, and B. Robinson, "Performance of a cross-aperture coupled single feed circularly polarised patch antenna", *Electronics Letters*, vol. 32, no. 7, pp. 612–613, Mar. 1996.

[7] B. Al-Jibouri, H. Evans, E. Korolkiewicz, E. Lim, A. Sambell, and T. Viasits, "Cavity model of circularly polarised cross-aperture-coupled microstrip antenna", *Microwaves, Antennas and Propagation, IEE Proceedings*, vol. 148, no. 3, pp. 147–152, 2001.

[8] Recticel. (2007), [Online]. Available: http://www.recticel.com/.

[9] D. Pozar, "A review of aperture coupled microstrip antennas: history, operation, development, and application", *Microwave Online System Company world wide web site*, Jul. 1996.

[10] R. Garg, P. Bhartia, I. Bahl, and A. Ittipiboon, *Microstrip antenna design handbook*. Artech House Antennas and Propagation Library, Jan. 2001.

[11] F. Declercq, H. Rogier, and C. Hertleer, "Permittivity and loss tangent characterization for garment antennas based on a new matrix-pencil two-line method", *IEEE Trans. Antennas Propag.*, vol. 56, no. 8, pp. 2548–2554, Aug. 2008.

3

Cylindrical Bending of Deformable Textile Rectangular-Patch Antennas

Freek Boeykens, Luigi Vallozzi and Hendrik Rogier

Published in International Journal of Antennas and Propagation

★ ★ ★

Textile patch antennas are well known as basic components for wearable systems that allow communication between a human body and the external world. Due to their flexibility, textile antennas are subjected to bending when worn, causing a variation in resonance frequency and radiation pattern with respect to the flat state in which their nominal design is performed. Hence, it is important for textile antenna engineers to be able to predict these performance parameters as a function of the bending radius. Therefore, we propose a a comprehensive analytical model that extends the cylindrical cavity model for conformal rigid patch antennas by incorporating the effects of patch stretching and substrate compression. It allows us to predict the resonance frequency and the radiation pattern as a function of the bending radius. Its validity has been verified experimentally. Unlike previous contributions, which concerned only qualitative studies by means of measurements and numerical full-wave simulations, the proposed model offers advantages in terms of physical insight, accuracy, speed and cost.

3.1 Introduction

Textile antennas emerged during the last decade as a new promising class of antennas that are particularly suitable for use in wearable applications [1]–[5]. These antennas can be fully integrated into intelligent garments, known as *wearable electronic systems* [6], enabling the transmission of data collected by wearable sensors or the reception of signals sent to wearable actuators integrated into clothing. The applications of wearable systems and textile antennas are numerous, ranging from rescue workers interventions' coordination to monitoring of dependent patients in hospital and sports applications.

In order to allow an optimal integration into garments without hindering the wearer's movements and comfort, the most suitable topology for a textile antenna is the planar patch. This flexible patch may be subjected to bending when the garment is worn, conforming its shape to the surface on which it is placed. As a result, also stretching of the patch (resulting in an elongation of the resonant length) and substrate compression (leading to a variation of the dielectric permittivity as a function of the bending radius) can occur.

Since the beginning of textile antenna design, these effects have been taken into account, however, they were not well-known and were compensated for by increasing the antenna bandwidth and validating the design afterwards by experiments [4]. Hence, it is essential to model the behaviour of the antenna under bent conditions and to predict the influence of bending on the resonance frequency and the radiation pattern. Full-wave simulation approaches are a potential solution, but most available commercial software tools do not offer the possibility of building a conformal mesh for bent structures, which results in inaccuracies in the obtained results. Moreover, these simulations do not offer physical insight into the bending mechanisms and may require high computational effort and time. Therefore, we propose analytical formulas that help the designer to assess a priori the effects of bending, stretching and compression. The focus is on cylindrical bending in particular, since, for wearable applications, textile antennas are usually deployed on cylindrical surfaces such as a human arm, a leg or a torso.

This study starts from past research efforts on rigid *conformal* antennas attached to cylindrical surfaces, of which several contributions can be found in literature. Krowne started by extending the popular cavity model for the rectangular patch antenna (introduced by Lo *et al.* in 1979 [7]) to the cylindrical case [8]. Resonance frequencies for the TE_z and TM_z modes were theoretically derived, though radiation patterns were not calculated in this model. A more comprehensive study was performed by Dahele *et al.* [9] and Luk *et al.* [10]. Their cavity model is only valid for patch antennas with a very thin substrate, but resonance frequencies, far fields, input impedances and Q-factors were derived analytically. Other analytical approaches were also introduced, which allow to calculate radiation patterns of antennas with patches of arbitrary shape [11]–[13]. However, they are based on an electric surface current model and assume the surface current distribution to

be known on the patch.

Cylindrical bending of *deformable* textile antennas has been an important subject in recent papers, but exclusively from an experimental point of view [4], [5], [14]–[16]. The general conclusions drawn from these contributions are that bending causes an upward shift of the resonance frequency, a broadening of the radiation pattern, a decrease in gain along broadside and an alteration of the polarisation (in case of a circularly polarised antenna). Yet, these studies are rather qualitative and do not provide physical insight into the complex mechanisms occurring due to antenna bending.

Here, we try to overcome all drawbacks of the previous analysis methods by proposing a comprehensive study on cylindrical bending of rectangular textile patch antennas. An analytical model based on the cylindrical cavity model for conformal antennas, which allows to calculate both the resonance frequency and the radiation pattern, is constructed. This offers the advantage of requiring only small computational effort for calculating the main antenna performance parameters.

In order to model deformable textile patch antennas, some novel extensions to rigid conformal antenna models are proposed:

1. Wearable textile antennas are usually realised with electrotextiles as conductive patch materials, which are subjected to stretching when the antenna is bent. This causes an elongation of the patch along one direction and shifts the resonance frequency [17]. This behaviour is integrated into the model by introducing a factor that determines the location of the original patch width.

2. Textile antennas are subjected to compression when bent, which causes a variation of its dielectric permittivity. This can be tackled by proposing an expression for the compressed permittivity $\epsilon_{r,\text{comp}}$ as a function of the bending radius.

The model is validated in twofold.

1. A theoretical validation is performed for large curvature radii using Debye's expansion for large-order Bessel functions. By doing so, the expressions for the planar cavity should be found.

2. Experimental validation is carried out by measuring five prototypes based on different substrates with different thicknesses, patch materials and operation frequencies.

The organisation of this chapter is as follows. First, the cavity model for cylindrical-rectangular antennas is described in Section 3.2. The expressions for

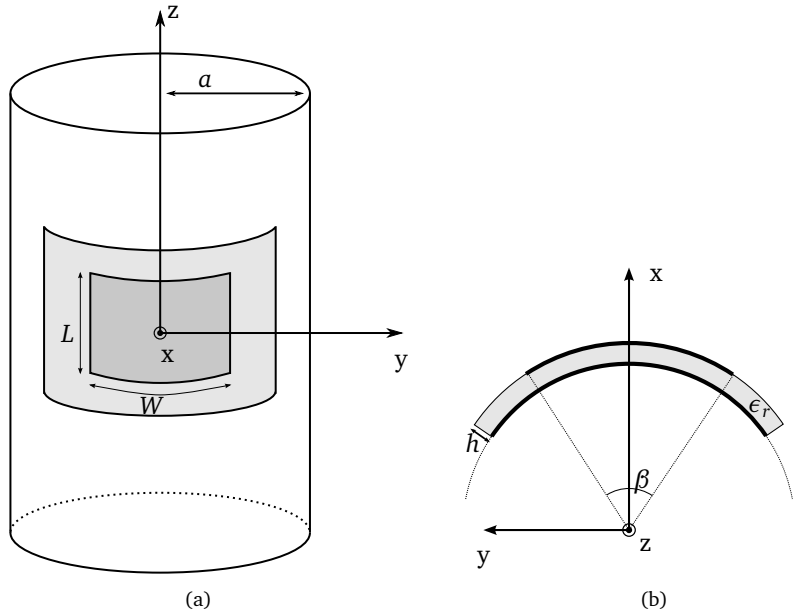

Figure 3.1: Geometry of the cavity: top view (a) and side view (b).

the resonant fields inside the cavity are calculated, from which the resonance frequencies and radiation patterns are derived. In Section 3.3, the cavity model is verified for large curvature radii by comparing the obtained dispersion relations with the expression for resonance frequencies in rectangular cavities. Section 3.4 presents the experimental results. The proposed model is verified by means of five textile antenna prototypes with different geometries and material characteristics. Both resonance frequencies and radiation patterns are compared. Finally, the general conclusions are summarised in Section 3.5.

3.2 Theory

The geometry of the cylindrical cavity representing the textile antenna is shown in Fig. 3.1. The length and width of the wearable antenna are denoted by L and W and the flexible dielectric substrate has a height h and relative permittivity ϵ_r. The curvature radius is a and the angle formed by the edges of the patch is β.

In order to obtain a relationship between W, a and β, one has to take into account whether the antenna patch is stretchable or not. According to [17], the following

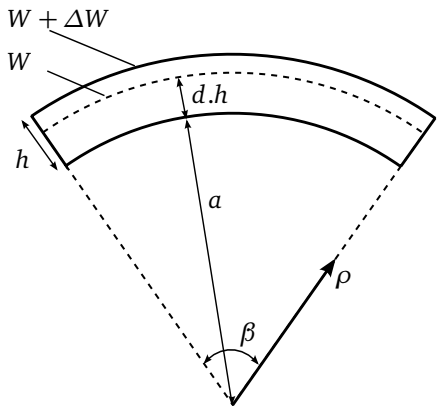

Figure 3.2: Patch elongation.

relations exist for stretchable patches:

$$\frac{\Delta W}{W} = \frac{h}{2a+h}, \tag{3.1a}$$

$$\beta(a+h) = W + \Delta W, \tag{3.1b}$$

with $W + \Delta W$ the width of the bent patch. This is shown in Fig. 3.2. Combining (3.1a) and (3.1b) leads to

$$\beta\left(a + \frac{h}{2}\right) = W. \tag{3.2}$$

This means that the original patch width is located at $\rho = a + \frac{h}{2}$ due to patch elongation. If the patch is non-stretchable, the patch length does not vary when bending the antenna and ground plane crumpling occurs. The original width W is then still located at $\rho = a + h$.

Because textile antennas can be constructed using both stretchable as non-stretchable patches, we introduce a factor d (Fig. 3.2) that determines the location of the original width:

$$W = \beta\,(a + hd)\,. \tag{3.3}$$

This factor d can take values between 0.5 and 1. For perfectly stretchable patches we find that $d = 0.5$ and for perfectly non-stretchable patches $d = 1$.

3.2.1 The cavity model

We now proceed with the derivation of the cylindrical cavity model [8]. Similar as for planar cavity models, the cavity is bounded by electric walls at $\rho = a$ and $\rho = a + h$ and magnetic walls at $\phi = \pm\frac{\beta}{2}$ and $z = \pm\frac{L}{2}$.

The electric and magnetic fields inside the cavity are given by (1.23):

$$\mathbf{E} = -\nabla \times \mathbf{F} - j\omega\mu\mathbf{A} + \frac{1}{j\omega\epsilon}\nabla(\nabla \cdot \mathbf{A}), \tag{3.4a}$$

$$\mathbf{H} = \nabla \times \mathbf{A} - j\omega\epsilon\mathbf{F} + \frac{1}{j\omega\mu}\nabla(\nabla \cdot \mathbf{F}), \tag{3.4b}$$

where, given the translation invariance of the structure, the vector potentials are defined by

$$\mathbf{A} = A_z \mathbf{u}_z,$$
$$\mathbf{F} = F_z \mathbf{u}_z.$$

The scalar wave functions A_z and F_z obey the scalar Helmholtz equation

$$\nabla^2\psi + k^2\psi = 0, \tag{3.5}$$

with $k^2 = \epsilon_r k_0^2$. In cylindrical coordinates (ρ, ϕ, z), this translates into

$$\frac{1}{\rho}\frac{\partial}{\partial\rho}\left(\rho\frac{\partial\psi}{\partial\rho}\right) + \frac{1}{\rho^2}\frac{\partial^2\psi}{\partial\phi^2} + \frac{\partial^2\psi}{\partial z^2} + k^2\psi = 0. \tag{3.6}$$

It is well-known that equations like this can be solved by separation of variables. Therefore, we substitute $\psi(\rho,\phi,z) = R(\rho)\Phi(\phi)Z(z)$ into the wave equation (3.6), what leads to the following system:

$$Z''(z) + k_z^2 Z(z) = 0, \tag{3.7a}$$

$$\Phi''(\phi) + k_\phi^2 \Phi(\phi) = 0, \tag{3.7b}$$

$$R''(\rho) + \frac{1}{\rho}R'\rho + \left(k^2 - k_z^2 - \frac{k_\phi^2}{\rho^2}\right)R(\rho) = 0, \tag{3.7c}$$

for which the following solutions are found:

$$Z(z) = A\cos(k_z z) + B\sin(k_z z), \tag{3.8a}$$

$$\Phi(\phi) = C\cos(k_\phi \phi) + D\sin(k_\phi \phi), \tag{3.8b}$$

$$R(\rho) = EJ_{k_\phi}(k_\rho \rho) + FY_{k_\phi}(k_\rho \rho). \tag{3.8c}$$

Here are J and Y the Bessel functions of the first and second kind, respectively, and is $k_\rho = \sqrt{k^2 - k_z^2}$.

TE mode

The TE_z mode is found by choosing $\mathbf{A} = 0$. From (3.4a), it is clear that the z-component of the electric field then disappears. After applying the boundary conditions on (3.8), we obtain

$$\psi = R_{k_\phi}(k_\rho\rho)\sin\left(k_\phi\phi + \frac{m\pi}{2}\right)\cos\left(k_z z + \frac{n\pi}{2}\right), \tag{3.9}$$

where

$$R_{k_\phi}(k_\rho\rho) = c_{\mathrm{TE}}\Big(Y'_{k_\phi}(k_\rho a)J_{k_\phi}(k_\rho\rho) - J'_{k_\phi}(k_\rho a)Y_{k_\phi}(k_\rho\rho)\Big), \tag{3.10}$$

and

$$k_\phi = \frac{m\pi}{\beta}, \tag{3.11a}$$

$$k_z = \frac{n\pi}{L}. \tag{3.11b}$$

The constant c_{TE} is a proportionality coefficient for the TE_z mode. Further in this chapter, we will also refer to the TE_z mode as the TE_{mn} mode.

TM mode

The TM_z solution can be found by choosing $\mathbf{F} = 0$. It is now clear from (3.4b) that the magnetic field has no z-component. Applying the boundary conditions on (3.8) leads to

$$\psi = R_{k_\phi}(k_\rho\rho)\cos\left(k_\phi\phi + \frac{m\pi}{2}\right)\sin\left(k_z z + \frac{n\pi}{2}\right), \tag{3.12}$$

where

$$R_{k_\phi}(k_\rho\rho) = c_{\mathrm{TM}}\Big(Y_{k_\phi}(k_\rho a)J_{k_\phi}(k_\rho\rho) - J_{k_\phi}(k_\rho a)Y_{k_\phi}(k_\rho\rho)\Big) \tag{3.13}$$

and the wave numbers k_ϕ and k_z are the same as in (3.11). The constant c_{TM} is a proportionality coefficient for TM_z mode. Similar as for the TE_z mode, further in this chapter, the TM_z mode will also be referred to as the TM_{mn} mode.

3.2.2 Resonance frequency

In order to find the expressions for ψ for the TE_{mn} and the TM_{mn} modes, all boundary conditions were applied, except one for each mode. In order to invoke this last boundary condition, ψ must satisfy a dispersion relation. For the TE_{mn} modes, this dispersion relation becomes

$$J'_{k_\phi}(k_\rho a)Y'_{k_\phi}\left(k_\rho(a+h)\right) = J'_{k_\phi}\left(k_\rho(a+h)\right)Y'_{k_\phi}(k_\rho a). \tag{3.14}$$

For the TM_{mn} modes, one finds

$$J_{k_\phi}(k_\rho a)Y_{k_\phi}\left(k_\rho(a+h)\right) = J_{k_\phi}\left(k_\rho(a+h)\right)Y_{k_\phi}(k_\rho a). \tag{3.15}$$

The resonance frequencies of the antenna in bent state are found as zeros of these transcendental equations.

3.2.3 Radiation pattern

The radiation pattern can be calculated from the equivalent magnetic currents $\mathbf{M} = E_\rho \mathbf{u}_\rho \times \mathbf{u}_n$ along the edges of the curved patch [10], [18].

In general, E_ρ can be written as

$$E_\rho = \lambda(\rho)\cos\left(\frac{m\pi}{\beta}\phi + \frac{m\pi}{2}\right)\cos\left(\frac{n\pi}{L}z + \frac{n\pi}{2}\right), \tag{3.16}$$

where $\lambda(\rho)$ is a mode-dependent factor. For the $\mathrm{TE_z}$ modes, $\lambda(\rho)$ is defined as

$$\lambda_{\mathrm{TE}}(\rho) = -\frac{1}{\rho}\frac{m\pi}{\beta} R_{\frac{m\pi}{\beta}}\left(\sqrt{k^2 - \left(\frac{n\pi}{L}\right)^2}\,\rho\right).$$

For the $\mathrm{TM_z}$ modes, $\lambda(\rho)$ becomes

$$\lambda_{\mathrm{TM}}(\rho) = -\frac{j\omega}{\epsilon}\frac{n\pi}{L}\sqrt{k^2 - \left(\frac{n\pi}{L}\right)^2} R'_{\frac{m\pi}{\beta}}\left(\sqrt{k^2 - \left(\frac{n\pi}{L}\right)^2}\,\rho\right).$$

The far-field components then follow from:

$$E_\theta = j\omega\mu_0 \frac{e^{-jk_0 r}}{\pi r}\sin\theta \sum_{p=-\infty}^{+\infty} e^{jp\phi} j^{p+1} f_p\left(-k_0\cos\theta\right), \tag{3.17a}$$

$$E_\phi = -jk_0 \frac{e^{-jk_0 r}}{\pi r}\sin\theta \sum_{p=-\infty}^{+\infty} e^{jp\phi} j^{p+1} g_p\left(-k_0\cos\theta\right). \tag{3.17b}$$

Remark that, according to the convention of Harrington, the elevation angle θ is measured from the z-axis. The auxiliary functions $f_p(u)$ and $g_p(u)$ are defined as follows:

$$f_p(u) = \frac{j\omega\epsilon_0 \tilde{M}_\phi(p,u)}{\left(k_0^2 - u^2\right) H_p^{(2)}\left((a+h)\sqrt{k_0^2 - u^2}\right)}, \tag{3.18a}$$

$$g_p(u) = \frac{1}{\sqrt{k_0^2 - u^2}\, H_p^{(2)\prime}\left((a+h)\sqrt{k_0^2 - u^2}\right)} \cdot\left(-\tilde{M}_z(p,u) + \frac{pu}{(a+h)\left(k_0^2 - u^2\right)}\tilde{M}_\phi(p,u)\right), \tag{3.18b}$$

with

$$\tilde{M}_\phi(p,u) = \frac{1}{2\pi}\int_0^{2\pi}\int_{-\infty}^{+\infty} M_\phi\left(a+h,\phi,z\right) e^{-jp\phi} e^{-juz}\,\mathrm{d}z\,\mathrm{d}\phi, \tag{3.19a}$$

$$\tilde{M}_z(p,u) = \frac{1}{2\pi}\int_0^{2\pi}\int_{-\infty}^{+\infty} M_z\left(a+h,\phi,z\right) e^{-jp\phi} e^{-juz}\,\mathrm{d}z\,\mathrm{d}\phi. \tag{3.19b}$$

In order to find $M_\phi\left(\rho,\phi,z\right)$ and $M_z\left(\rho,\phi,z\right)$, it is important to know that the structure radiates from the fringing fields that are exposed above the substrate at the edges of the patch. Hence, these equivalent magnetic currents need to be found at $\phi=\pm\frac{\beta}{2}$ and $z=\pm\frac{L}{2}$.

At $\phi=-\frac{\beta}{2}$, we find with $\mathbf{u}_n=-\mathbf{u}_\phi$ that $\mathbf{M}=M_z\mathbf{u}_z$. The components M_z and $\tilde{M}_z$ are then

$$M_z\left(\rho,\phi,z\right)=-\lambda\left(\rho\right)\cos\left(\frac{n\pi}{L}z+\frac{n\pi}{2}\right), \tag{3.20a}$$

$$\tilde{M}_z(p,u)=-\lambda\left(a+h\right)e^{jp\frac{\beta}{2}}\frac{1}{2\pi}\int_{-\frac{L}{2}}^{\frac{L}{2}}\cos\left(\frac{n\pi}{L}z+\frac{n\pi}{2}\right)e^{-juz}\,\mathrm{d}z. \tag{3.20b}$$

Similarly, at $\phi=\frac{\beta}{2}$, we find with $\mathbf{u}_n=\mathbf{u}_\phi$:

$$M_z\left(\rho,\phi,z\right)=\lambda\left(\rho\right)(-1)^m\cos\left(\frac{n\pi}{L}z+\frac{n\pi}{2}\right), \tag{3.21a}$$

$$\tilde{M}_z(p,u)=-\lambda\left(a+h\right)(-1)^m e^{-jp\frac{\beta}{2}}\frac{1}{2\pi}\int_{-\frac{L}{2}}^{\frac{L}{2}}\cos\left(\frac{n\pi}{L}z+\frac{n\pi}{2}\right)e^{-juz}\,\mathrm{d}z. \tag{3.21b}$$

At $z=-\frac{L}{2}$, $\mathbf{M}=M_\phi\mathbf{u}_\phi$, because $\mathbf{u}_n=-\mathbf{u}_z$. The components M_ϕ and $\tilde{M}_\phi$ then become

$$M_\phi\left(\rho,\phi,z\right)=\lambda\left(\rho\right)\cos\left(\frac{m\pi}{\beta}\phi+\frac{m\pi}{2}\right), \tag{3.22a}$$

$$\tilde{M}_\phi(p,u)=\lambda\left(a+h\right)e^{ju\frac{L}{2}}\frac{1}{2\pi}\int_{-\frac{\beta}{2}}^{\frac{\beta}{2}}\cos\left(\frac{m\pi}{\beta}\phi+\frac{m\pi}{2}\right)e^{-jp\phi}\,\mathrm{d}\phi. \tag{3.22b}$$

Finally, at $z=\frac{L}{2}$, $\mathbf{u}_n=\mathbf{u}_z$ and we obtain:

$$M_\phi\left(\rho,\phi,z\right)=-\lambda\left(\rho\right)(-1)^n\cos\left(\frac{m\pi}{\beta}\phi+\frac{m\pi}{2}\right), \tag{3.23a}$$

$$\tilde{M}_\phi(p,u)=-\lambda\left(a+h\right)(-1)^n e^{-ju\frac{L}{2}}\frac{1}{2\pi}\int_{-\frac{\beta}{2}}^{\frac{\beta}{2}}\cos\left(\frac{m\pi}{\beta}\phi+\frac{m\pi}{2}\right)e^{-jp\phi}\,\mathrm{d}\phi. \tag{3.23b}$$

The components $\tilde{M}_\phi$ and $\tilde{M}_z$ are then

$$\tilde{M}_\phi(p,u)=-\lambda(a+h)\,\sigma\left(n,uL\right)\,I\left(m,p,\beta\right), \tag{3.24a}$$

$$\tilde{M}_z(p,u)=\lambda(a+h)\,\sigma\left(m,p\beta\right)\,I\left(n,u,L\right), \tag{3.24b}$$

with

$$\sigma(q,a) = (-1)^q e^{-j\frac{a}{2}} - e^{j\frac{a}{2}},$$
$$I(q,a,b) = \int_{-\frac{b}{2}}^{\frac{b}{2}} \cos\left(\frac{q\pi}{b}x + \frac{q\pi}{2}\right) e^{-jax}\,\mathrm{d}x = j\frac{ab^2\,\sigma\left(q,ab\right)}{a^2b^2 - q^2\pi^2}.$$

After substitution of these results in (3.18) and in (3.17), the following far-field components are found:

$$E_\theta = \frac{\lambda(a+h)}{2\pi^2\sin\theta}\frac{e^{-jk_0r}}{r}\sigma\left(n,-Lk_0\cos\theta\right)\cdot\sum_{p=-\infty}^{+\infty}\frac{e^{jp\phi}\,j^{p+1}I(m,p,\beta)}{H_p^{(2)}\left((a+h)k_0\sin\theta\right)}, \tag{3.25a}$$

$$E_\phi = j\frac{\lambda(a+h)}{2\pi^2}\frac{e^{-jk_0r}}{r}\cdot\sum_{p=-\infty}^{+\infty}\frac{e^{jp\phi}\,j^{p+1}}{H_p^{(2)\prime}\left((a+h)k_0\sin\theta\right)}\left(\sigma(m,p\beta)I(n,-k_0\cos\theta,L)\right.$$
$$\left. - \frac{p\cos\theta\;\sigma(n,-Lk_0\cos\theta)\;I(m,p,\beta)}{(a+h)k_0\sin^2\theta}\right). \tag{3.25b}$$

3.3 Validation of the model for large curvature radii

Now, the analytical model will be verified for the limit case where the curvature radius a tends to ∞. A rectangular cavity is then obtained and the following relation should be found:

$$k^2 = \left(\frac{m\pi}{W}\right)^2 + \left(\frac{n\pi}{L}\right)^2 + \left(\frac{l\pi}{h}\right)^2. \tag{3.26}$$

By rewriting (3.14) and (3.15) using the substitutions

$$\nu = \frac{m\pi}{\beta}, \tag{3.27a}$$
$$\sec\alpha = \sqrt{k^2 - \left(\frac{n\pi}{L}\right)^2}\frac{W-\beta hd}{m\pi}, \tag{3.27b}$$
$$\sec\gamma = \sqrt{k^2 - \left(\frac{n\pi}{L}\right)^2}\frac{W-\beta h(d-1)}{m\pi}, \tag{3.27c}$$

we obtain

$$J_\nu\left(\nu\sec\alpha\right)Y_\nu\left(\nu\sec\gamma\right) = J_\nu\left(\nu\sec\gamma\right)Y_\nu\left(\nu\sec\alpha\right), \tag{3.28a}$$
$$J'_\nu\left(\nu\sec\alpha\right)Y'_\nu\left(\nu\sec\gamma\right) = J'_\nu\left(\nu\sec\gamma\right)Y'_\nu\left(\nu\sec\alpha\right). \tag{3.28b}$$

When taking the limit for a to ∞, ν also goes to ∞, while α and γ remain constant. Debye's asymptotic expansion for large-order Bessel functions can then be utilised for $\nu \to \infty$ [19]:

$$J_\nu\left(\nu \sec\chi\right) \sim \sqrt{\frac{2}{\pi\nu\tan\chi}}\left(\cos\xi \sum_{k=0}^{\infty} \frac{U_{2k}\left(j\cot\chi\right)}{\nu^{2k}} - j\sin\xi \sum_{k=0}^{\infty} \frac{U_{2k+1}\left(j\cot\chi\right)}{\nu^{2k+1}}\right), \quad (3.29a)$$

$$Y_\nu\left(\nu \sec\chi\right) \sim \sqrt{\frac{2}{\pi\nu\tan\chi}}\left(\sin\xi \sum_{k=0}^{\infty} \frac{U_{2k}\left(j\cot\chi\right)}{\nu^{2k}} + j\cos\xi \sum_{k=0}^{\infty} \frac{U_{2k+1}\left(j\cot\chi\right)}{\nu^{2k+1}}\right), \quad (3.29b)$$

$$J'_\nu\left(\nu \sec\chi\right) \sim \sqrt{\frac{\sin 2\chi}{\pi\nu}}\left(-\sin\xi \sum_{k=0}^{\infty} \frac{V_{2k}\left(j\cot\chi\right)}{\nu^{2k}} - j\cos\xi \sum_{k=0}^{\infty} \frac{V_{2k+1}\left(j\cot\chi\right)}{\nu^{2k+1}}\right), \quad (3.29c)$$

$$Y'_\nu\left(\nu \sec\chi\right) \sim \sqrt{\frac{\sin 2\chi}{\pi\nu}}\left(\cos\xi \sum_{k=0}^{\infty} \frac{V_{2k}\left(j\cot\chi\right)}{\nu^{2k}} - j\sin\xi \sum_{k=0}^{\infty} \frac{V_{2k+1}\left(j\cot\chi\right)}{\nu^{2k+1}}\right), \quad (3.29d)$$

with

$$\xi = \nu\left(\tan\chi - \chi\right) - \frac{\pi}{4},$$

and $U_k(p)$ and $V_k(p)$ polynomials in p of degree $3k$, given by $U_0(p) = V_0(p) = 1$, and

$$U_{k+1}(p) = \frac{1}{2}p^2\left(1-p^2\right)U'_k(p) + \frac{1}{8}\int_0^p \left(1-5t^2\right)U_k(t)\,\mathrm{d}t,$$

$$V_{k+1}(p) = U_{k+1}(p) - \frac{1}{2}p\left(1-p^2\right)U_k(p) - p^2\left(1-p^2\right)U'_k(p).$$

Using the lowest-order Debye's expression, one finds for both the dispersion relations:

$$\sin\xi\cos\xi' = \sin\xi'\cos\xi \quad (3.30)$$

with

$$\xi = \nu\,(\tan\alpha - \alpha) - \frac{\pi}{4},$$
$$\xi' = \nu\,(\tan\gamma - \gamma) - \frac{\pi}{4}.$$

This leads to

$$\xi' = \xi + l\pi, \tag{3.31a}$$
$$\tan\gamma - \gamma = \tan\alpha - \alpha + \frac{l}{m}\beta. \tag{3.31b}$$

Assuming that $h << \lambda$, a first-order Taylor expansion can be performed on $\tan\gamma(h) - \gamma(h)$ and $\tan\alpha(h) - \alpha(h)$ for $h \to 0$. Therefore, we first need to determine $\frac{\mathrm{d}\alpha}{\mathrm{d}h}$ and $\frac{\mathrm{d}\gamma}{\mathrm{d}h}$. By calculating the derivative of the left hand sides of (3.27b) and (3.27c) to α and γ, respectively, and their right hand sides to h, the derivatives are easily found:

$$\frac{\mathrm{d}\alpha}{\mathrm{d}h} = -\sqrt{k^2 - \left(\frac{n\pi}{L}\right)^2}\,\frac{\beta d}{m\pi}\,\frac{\cos^2\alpha}{\sin\alpha}, \tag{3.32a}$$
$$\frac{\mathrm{d}\gamma}{\mathrm{d}h} = -\sqrt{k^2 - \left(\frac{n\pi}{L}\right)^2}\,\frac{\beta(d-1)}{m\pi}\,\frac{\cos^2\gamma}{\sin\gamma}. \tag{3.32b}$$

The first order Taylor expansions around $h = 0$ are then

$$\tan\alpha(h) - \alpha(h) \approx \tan\alpha(0) - \alpha(0) + h\left(-\sqrt{k^2 - \left(\frac{n\pi}{L}\right)^2}\,\frac{\beta d}{m\pi}\sin\alpha(0)\right), \tag{3.33a}$$
$$\tan\gamma(h) - \gamma(h) \approx \tan\gamma(0) - \gamma(0) + h\left(-\sqrt{k^2 - \left(\frac{n\pi}{L}\right)^2}\,\frac{\beta(d-1)}{m\pi}\sin\gamma(0)\right). \tag{3.33b}$$

Since $\alpha(0) = \gamma(0)$, the first order Taylor expansion of expression (3.31b) becomes:

$$\sin\alpha(0) = \frac{l\pi}{h}\,\frac{1}{\sqrt{k^2 - \left(\frac{n\pi}{L}\right)^2}}. \tag{3.34}$$

Combining (3.27b) and (3.34) results in:

$$\sqrt{1 - \frac{1}{\left(k^2 - \left(\frac{n\pi}{L}\right)^2\right)\left(\frac{W}{m\pi}\right)^2}} = \frac{l\pi}{h}\,\frac{1}{\sqrt{k^2 - \left(\frac{n\pi}{L}\right)^2}}, \tag{3.35}$$

which finally leads to (3.26) and verifies the transition to a rectangular cavity.

3.4 Comparison of experimental and theoretical results

Using this model, the resonance frequencies and radiation patterns of flexible textile antennas can be calculated analytically. However, when comparing the measured resonance frequencies of a fabricated textile antenna with the frequencies obtained from our model for different bending radii, a discrepancy is noticed. This is due to the fact that textile antennas are subjected to compression when bent. Consequently, the substrate permittivity will change as a function of the bending radius. This effect needs to be incorporated in our model in order to provide a good prediction of the resonance frequency. In other words, an expression for the permittivity $\epsilon_{r,\text{comp}}$ of a substrate subjected to compression needs to be found.

3.4.1 Experimental setup

By measuring five prototypes with different specifications and constructed on different flexible materials, the effect of several parameters on $\epsilon_{r,\text{comp}}$ is investigated. Their geometry is displayed in Fig. 3.3. All prototypes are fed by a probe feed structure, with the probe located on the perpendicular bisector of the L_p edge.

Prototype 1 and 2 are both fabricated on aramid substrates and are designed for the 1.57 GHz GPS band. The patch material of prototype 1 is the stretchable electro-textile Flectron®, whereas non-stretchable copper foil is used for prototype 2. Prototype 3, 4 and 5 are fabricated on cotton substrates and have copper foil as patch material. Prototypes 3 and 5 are designed for the 1.57 GHz GPS band, whereas prototype 4 operates in the 2.45 GHz ISM band. The difference between prototype 3 and 5 is the thickness of the substrate. The parameters of the prototypes are shown in Table 3.1, where the substrate height h is determined based on the ISO 5084 standard [20].

For these prototypes, the resonance frequencies in flat and bent state are measured by means of a PNA-X vector network analyser. The bent states are realised by attaching the antennas to plastic cylinders with different radii ranging from 31.5 mm to 90 mm. These radii resemble typical curvatures of human body parts.

When the antennas are bent in the W_p-direction, the model is used by setting $L = L_p$ and $W = W_p$. According to the model, the TE_{10} mode is then excited and (3.14) needs to be solved in order to determine the resonance frequency. Similarly, when bending the antennas in the L_p-direction, one has to set $L = W_p$ and $W = L_p$. According to the model, the TM_{01} mode is then excited and the resonance frequency follows from (3.15).

3.4.2 Compression effects on the permittivity

After comparing the measured resonance frequencies of the prototypes for the different bending radii, the following observations are made:

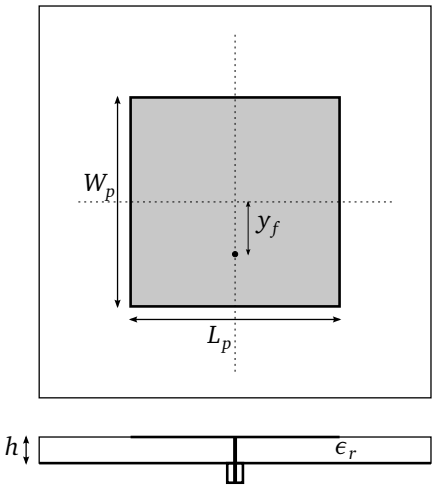

Figure 3.3: Geometry of a prototype.

Table 3.1: Parameters of the prototypes.

Prototype	L_p [mm]	W_p [mm]	h [mm]	y_f [mm]	ϵ_r	d
1	81.2	69.25	2	16	1.75	0.5
2	81.2	69.25	2	16	1.75	1
3	78.5	69.3	2.7	17	1.715	1
4	52.5	43.7	2.7	11	1.715	1
5	78.5	68.3	4.04	16.8	1.715	1

1. The $\epsilon_{r,\text{comp}}$ is inversely proportional to the bending radius a, since compression becomes stronger as the curvature radius decreases. Because of this compression, air is pushed out of the substrate and the permittivity increases.
2. The part of the substrate that undergoes the largest compression has a height $h(d-0.5)$ and $\epsilon_{r,\text{comp}}$ is directly proportional to this.
3. The compression is not frequency dependent.

Based on these observations, an empirical formula for $\epsilon_{r,\text{comp}}$ can be found:

$$\epsilon_{r,\text{comp}} = \epsilon_{r,\text{flat}} \left(1 + \eta \frac{h(d-0.5)}{a}\right). \tag{3.36}$$

The permittivity $\epsilon_{r,\text{flat}}$ is obtained by evaluating (3.26) after measuring the antenna in flat state under well-defined environmental conditions. It therefore cap-

Table 3.2: Proportionality factors η for the compression correction term.

Prototype	TE_{10} mode	TM_{01} mode
2	1.589	0.380
3	1.497	0.214
4	1.472	0.592
5	1.485	0.654

tures effects such as humidity, temperature, fringing effects, etc., while the second term in (3.36) isolates the effect of bending. The parameter h is the height of the flexible substrate in flat state, measured according to the ISO 5084 standard. This simplifies the work of the designer, since he doesn't need to measure the height of the substrates for each bending radius.

Expression (3.36) also takes into account the following remarks:

1. When a tends to ∞, the antenna becomes planar and $\epsilon_{r,\text{flat}}$ is found.
2. For perfectly stretchable antennas, $\epsilon_{r,\text{comp}} = \epsilon_{r,\text{flat}}$. Hence, the resonance frequency will not change when the antenna is bent.

The proportionality factor η can be found for each prototype with a non-stretchable patch by minimising an error function $\tau(\eta)$, defined by

$$\tau(\eta) = \frac{1}{N}\sum_{i=1}^{N}\frac{\left|f_{\text{mod},i}(\eta) - f_{\text{meas},i}\right|}{f_{\text{meas},i}}. \tag{3.37}$$

This function represents the relative mean error between the modelled and measured resonance frequencies of a bent prototype, with N the number of cylinders.

The calculation of η is carried out iteratively by combining MATLAB's minimisation function *fminsearch* with our analytical model in Maple. The obtained values for both the TE_{10} and the TM_{01} modes are shown in Table 3.2. The η-values for the TE_{10} modes are quite similar, whereas the values for the TM_{01} mode exhibit larger differences. Also, there is a significant difference between the values for the TE_{10} mode and the TM_{01} mode. This is due to the geometry and feeding structure of the prototypes. The solid feed points are not located in the centre of the patches and thus produce different compression effects, depending on whether the prototypes are bent in the W_p-direction or the L_p-direction.

Table 3.3 and Table 3.4 display the error values when using $\epsilon_r = \epsilon_{r,\text{flat}}$ (shown as $\tau(0)$) and $\epsilon_r = \epsilon_{r,\text{comp}}$ (shown as $\tau(\eta)$) for the TE_{10} mode and the TM_{01} mode respectively. A constant small error of ca. 0.1% can be found for all prototypes when using the ideal proportionality factor η, validating the use of (3.36).

Table 3.3: Relative mean error between the modelled and measured resonance frequencies of the bent prototypes for the TE_{10} mode.

Prototype	$\tau(0)$ [%]	$\tau(\eta)$ [%]
1	0.09	0.09
2	1.56	0.03
3	1.97	0.09
4	1.94	0.07
5	2.91	0.12

Table 3.4: Relative mean error between the modelled and measured resonance frequencies of the bent prototypes for the TM_{01} mode.

Prototype	$\tau(0)$ [%]	$\tau(\eta)$ [%]
1	0.04	0.04
2	0.37	0.03
3	0.23	0.07
4	0.76	0.10
5	1.28	0.07

3.4.3 Resonance frequency

Fig. 3.4 shows the modelled and measured resonance frequencies of prototypes 1 and 3 as a function of the bending radius when the antennas are bent in the W_p-direction. Prototype 1 has a stretchable patch, so patch elongation occurs and the substrate will not be compressed ($\epsilon_{r,\text{comp}} = \epsilon_{r,\text{flat}}$). Consequently, the resonance frequency does almost not change when the antenna is bent. Prototype 3 has a non-stretchable patch, therefore the resonance frequency will change with varying curvature radii. The resonance frequencies obtained from the model with and without compression correction are displayed, where the model without compression correction can be seen as if the antenna would be conformally attached to the cylinders. Since the prototypes are flexible deformable antennas, the measured curve follows the curve obtained from the model with compression correction. One also notices that the increase in resonance frequency for smaller bending radii is not as distinct as compared to the conformal case. This behaviour is also observed for the other prototypes.

In Fig. 3.5, the modelled and measured resonance frequencies of prototypes 1 and 3 are displayed as a function of the bending radius when the antennas are bent in the L_p-direction. According to the model, the resonance frequency of prototype 1 does not vary since no compression occurs and the resonant length is not bent

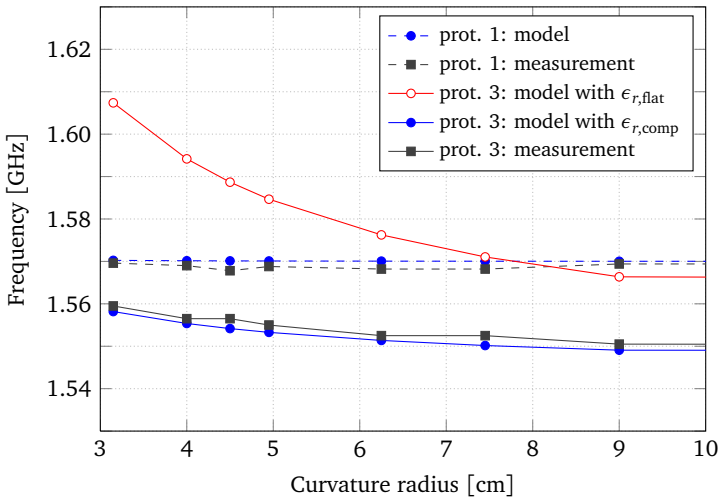

Figure 3.4: Resonance frequencies of prototypes 1 and 3 as a function of the bending radius when the antennas are bent along the W_p-direction.

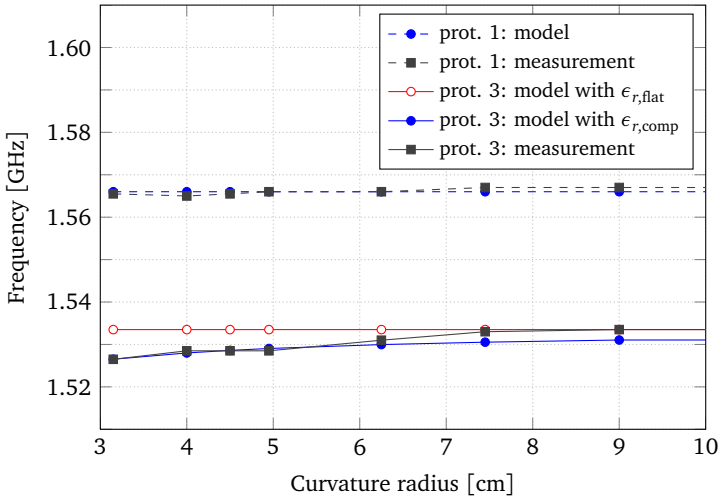

Figure 3.5: Resonance frequencies of prototypes 1 and 3 as a function of the bending radius when the antennas are bent along the L_p-direction.

in TM_z mode. For prototype 3, a decrease in resonance frequency now occurs for smaller bending radii. This effect is purely due to compression of the substrate, which can also be noticed by comparison with the curve obtained from the model without compression correction, where the resonance frequency doesn't change.

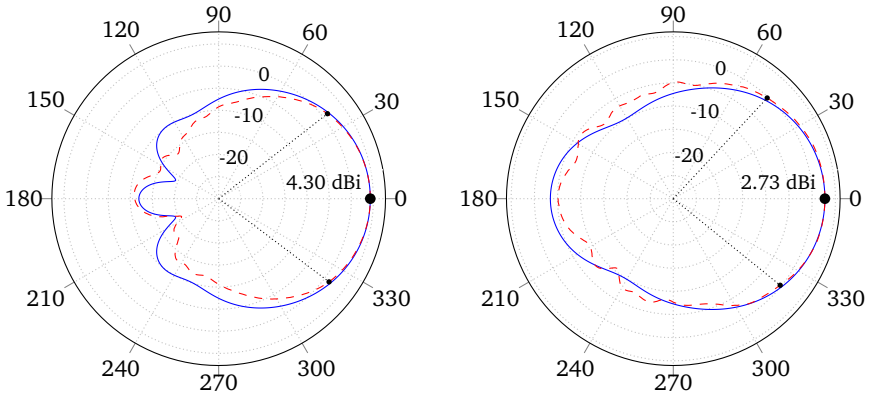

Figure 3.6: Radiation pattern in xy-plane of prototype 1 for 1.567 GHz when bent in the W_p-direction. The bending radii are 90 mm (a) and 31.5 mm (b). The modelled radiation pattern is drawn by the solid line, the measured radiation pattern is plotted by the dashed line.

Again, this result is also observed for the other prototypes.

As a footnote, we like to point out the difference in resonance frequency for the flat state between Fig. 3.4 and Fig. 3.5. The measurements for the TM_z case were performed later in time than those for the TE_z case. As a result, the resonance frequencies of the prototypes have changed due to humidity effects. This effect is larger for prototype 3 than for prototype 1, since the cotton substrate suffers more from this effect than the aramid substrate [21]. However, the model still remains accurate, since it only takes into account bending effects. In other words, using this formulation, the effect of bending on the behaviour of deformable antennas can be isolated.

3.4.4 Radiation pattern

Fig. 3.6 shows the modelled and measured radiation patterns in the xy-plane (as defined in Fig. 3.1) of the stretchable prototype 1 for curvature radii of 90 mm and 31.5 mm at a frequency of 1.567 GHz (the resonance frequency of the planar antenna) when the antenna is bent in the W_p direction. The radiation pattern calculated by the model is normalised w.r.t. the measured gain in broadside direction, since only its shape can be predicted. For a curvature radius of 90 mm, the measured 3 dB beamwidth is 75° and the modelled 3 dB beamwidth is 80°. For a bending radius of 31.5 mm, the measured 3 dB beamwidth is 86° and the modelled 3 dB beamwidth is 84°.

On Fig. 3.7, the modelled and measured radiation patterns in the xy-plane of the non-stretchable prototype 2 are displayed for curvature radii of 90 mm and

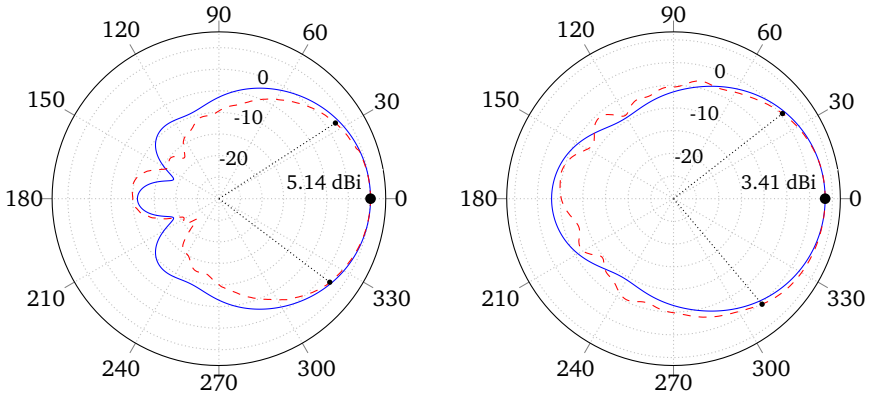

Figure 3.7: Radiation pattern in xy-plane of prototype 2 for 1.573 GHz when bent in the W_p-direction. The bending radii are 90 mm (a) and 31.5 mm (b). The modelled radiation pattern is drawn by the solid line, the measured radiation pattern is plotted by the dashed line.

31.5 mm at a frequency of 1.573 GHz (the resonance frequency of the planar antenna) when the antenna is bent in the W_p-direction. For a curvature radius of 90 mm, the measured 3 dB beamwidth is 70° and the modelled 3 dB beamwidth is 80°. For a bending radius of 31.5 mm, the measured 3 dB beamwidth is 88° and the modelled 3 dB beamwidth is 86°.

There is no distinct difference between the shape of the radiation patterns of prototype 1 and 2. Hence, stretching has almost no influence on the radiation pattern of bent flexible antennas. Also, from the model we conclude that the use of the corrected permittivity due to compression has almost no influence on the radiation pattern.

Fig. 3.8 shows the modelled and measured radiation patterns in the xy-plane of prototype 2 for curvature radii of 90 mm and 40 mm at a frequency of 1.573 GHz when the antenna is bent in the L_p-direction. For a curvature radius of 90 mm, the measured 3 dB beamwidth is 85° and the modelled 3 dB beamwidth is 82°. For a bending radius of 40 mm, the measured 3 dB beamwidth is 94° and the modelled 3 dB beamwidth is 94°.

The influence of bending on the gain along broadside direction and the 3 dB beamwidth is shown in Fig. 3.9. The measured gain and 3 dB beamwidth of prototype 1 and 2 when the antennas are bent in the W_p-direction are displayed. For smaller bending radii, a decrease of the maximum gain and an increase of the 3 dB beamwidth is noticed. This effect is stronger for antennas with non-stretchable patches. The same results can be found when bending the antennas along the L_p direction.

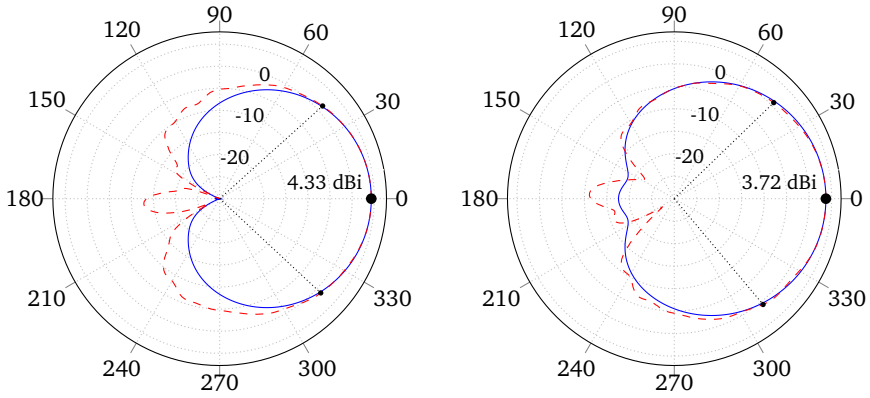

Figure 3.8: Radiation pattern in xy-plane of prototype 2 for 1.573 GHz when bent in the L_p-direction. The bending radii are 90 mm (a) and 40 mm (b). The modelled radiation pattern is drawn by the solid line, the measured radiation pattern is plotted by the dashed line.

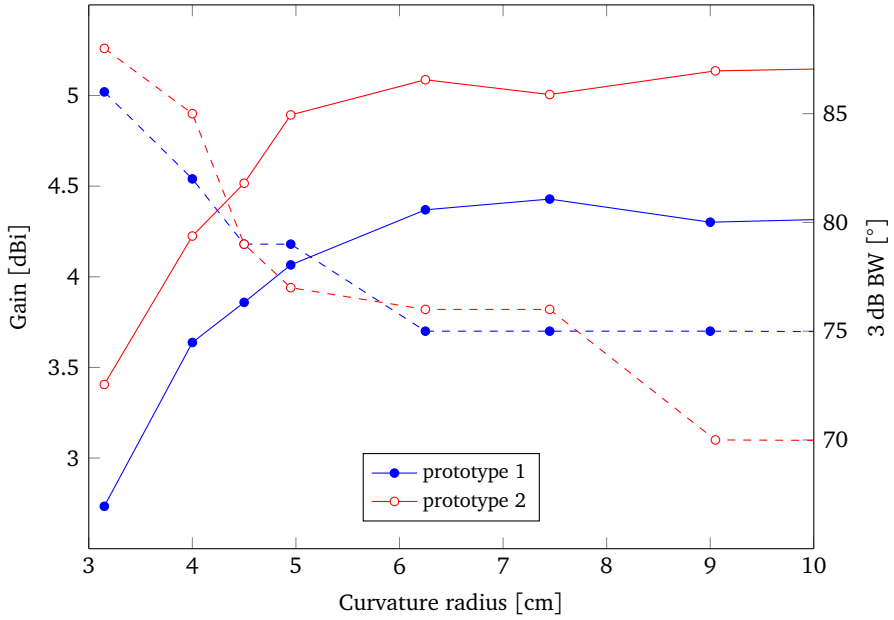

Figure 3.9: Measured gain and 3 dB beamwidth of prototypes 1 and 2 when the antennas are bent in the W_p-direction. The solid lines indicate the gain along broadside, the dashed lines show the 3 dB beamwidths.

3.5 Conclusion

In this chapter, a novel analytical model for cylindrically bent textile patch antennas was proposed. The starting point was the existing analytical model for conformal cylindrical-rectangular patch antennas, in which additional effects due to stretching and compression were incorporated. The model allows to calculate textile antenna performance parameters, such as resonance frequency and radiation pattern, as a function of the bending radius. Moreover, it answers to the need for a fast and accurate prediction tool for bent textile patch antennas, in contrast to previously proposed measurement- or simulation-based analysis methods, which are time consuming, expensive and do not provide physical insight into the mechanisms of bending. The resonance frequencies as a function of the bending radius can be obtained by numerically solving the cavity's dispersion relations, while the far field patterns are given in closed-form expressions. Two main novelties were introduced in the proposed model, dedicated to the particular case of textile antennas:

1. The patch elongation due to stretching has been derived by geometrical considerations and has been taken into account in the model.
2. An expression for the substrate permittivity as a function of the bending radius has been proposed, which isolates the effect of bending from all other external effects.

The validity of the proposed model has been successfully verified in two ways. First, it was analytically demonstrated that for large curvature radii (i.e. for $a \rightarrow \infty$) the dispersion relations converge to the one valid for the flat state. Secondly, an experimental verification of the model was performed by means of a measurement campaign in which the resonance frequencies and the radiation patterns of five different textile patch antenna prototypes were measured for different bending radii. In particular, the new model now captures the following two effects:

1. Concerning the resonance frequency, the measurements showed a significant variation for antennas with a non-stretchable patch and a nearly constant resonance frequency for antennas with a perfectly stretchable patch.
2. Regarding the radiation patterns, the experiments demonstrated that stretching has almost no influence on the radiation pattern of bent flexible antennas.

In summary, an excellent agreement is now obtained between measured results and the new model.

Based on the obtained results, it can be concluded that the proposed model represents a valuable tool for textile antenna design engineers, allowing performance

prediction and analysis of bent textile antennas. The model shows clear advantages with respect to previously employed methods, such as measurements and simulations, in terms of accuracy and computational cost. Moreover, it provides physical insight into bending mechanisms of textile patch antennas.

References

[1] P. Salonen, L. Sydanheimo, M. Keskilammi, and M. Kivikoski, "A small planar inverted-F antenna for wearable applications", in *Wearable Computers, 1999. Digest of Papers. The Third International Symposium on*, 1999, pp. 95–100.

[2] M. Klemm, I. Locher, and G. Troster, "A novel circularly polarized textile antenna for wearable applications", in *Wireless Technology, 2004. 7th European Conference on*, 2004, pp. 285–288.

[3] P. Massey, "Mobile phone fabric antennas integrated within clothing", in *Antennas and Propagation, 2001. Eleventh International Conference on (IEE Conf. Publ. No. 480)*, vol. 1, 2001, pp. 344–347.

[4] A. Tronquo, H. Rogier, C. Hertleer, and L. Van Langenhove, "Robust planar textile antenna for wireless body LANs operating in 2.45 GHz ISM band", *Electronics Letters*, vol. 42, no. 3, pp. 142–143, Feb. 2006.

[5] C. Hertleer, H. Rogier, L. Vallozzi, and L. Van Langenhove, "A textile antenna for off-body communication integrated into protective clothing for firefighters", *IEEE Trans. Antennas Propag.*, vol. 57, no. 4, pp. 919–925, Apr. 2009.

[6] A. Bonfiglio and D. De Rossi, Eds., *Wearable Monitoring Systems*. Springer US, 2011.

[7] Y. Lo, D. Solomon, and W. Richards, "Theory and experiment on microstrip antennas", *IEEE Trans. Antennas Propag.*, vol. 27, no. 2, pp. 137–145, Mar. 1979.

[8] C. Krowne, "Cylindrical-rectangular microstrip antenna", *IEEE Trans. Antennas Propag.*, vol. 31, no. 1, pp. 194–199, Jan. 1983.

[9] J. Dahele, R. Mitchell, K. Luk, and K. Lee, "Effect of curvature on characteristics of rectangular patch antenna", *Electronics Letters*, vol. 23, no. 14, pp. 748–749, Jul. 1987.

[10] K.-M. Luk, K.-F. Lee, and J. Dahele, "Analysis of the cylindrical-rectangular patch antenna", *IEEE Trans. Antennas Propag.*, vol. 37, no. 2, pp. 143–147, Feb. 1989.

[11] J. Ashkenazy, S. Shtrikman, and D. Treves, "Electric surface current model for the analysis of microstrip antennas on cylindrical bodies", *IEEE Trans. Antennas Propag.*, vol. 33, no. 3, pp. 295–300, Mar. 1985.

[12] T. Habashy, S. Ali, and J.-A. Kong, "Input impedance and radiation pattern of cylindrical-rectangular and wraparound microstrip antennas", *IEEE Trans. Antennas Propag.*, vol. 38, no. 5, pp. 722–731, May 1990.

[13] D. Werner, R. Allard, R. Martin, and R. Mittra, "A reciprocity approach for calculating radiation patterns of arbitrarily shaped microstrip antennas mounted on circularly cylindrical platforms", *IEEE Trans. Antennas Propag.*, vol. 51, no. 4, pp. 730–738, Apr. 2003.

[14] T. Kellomäki, J. Heikkinen, and M. Kivikoski, "Effects of bending GPS antennas", in *Microwave Conference, 2006. APMC 2006. Asia-Pacific*, 2006, pp. 1597–1600.

[15] L. Vallozzi, H. Rogier, C. Hertleer, and L. Van Langenhove, "Radiation characteristics of a textile antenna designed for apparal application", in *IEEE Symposium for Space Applications of Wireless & RFID (SWIRF 2007)*, May 2007.

[16] S. Sankaralingam and B. Gupta, "Development of textile antennas for body wearable applications and investigations on their performance under bent conditions", *Progress in Electromagnetics Research B*, vol. 22, pp. 53–71, 2010.

[17] I. Locher, M. Klemm, T. Kirstein, and G. Troster, "Design and characterization of purely textile patch antennas", *IEEE Trans. Adv. Packag.*, vol. 29, no. 4, pp. 777–788, Nov. 2006.

[18] R. Harrington, *Time-Harmonic Electromagnetic Fields*. New York, US: McGraw-Hill, 1961, pp. 246–248.

[19] F. Olver, D. Lozier, R. Boisvert, and C. Clark, Eds., *NIST Handbook of Mathematical Functions*. Cambrigde University Press, 2010, pp. 231–232.

[20] *ISO 5084: determination of thickness of textiles and textile products*, ISO, 1996.

[21] C. Hertleer, A. Van Laere, H. Rogier, and V. La, "Influence of relative humidity on textile antenna performance", *Textile Research Journal*, vol. 80, pp. 177–183, Jan. 2010.

4

Modelling the Uncertainty in the Resonance Frequency of Textile Antennas due to Bending

Freek Boeykens, Hendrik Rogier and Luigi Vallozzi

Submitted for publication in the IEEE Transactions on Antennas and Propagation

★ ★ ★

In the previous chapter, it was shown that textile antennas are subjected to bending when worn, resulting in a shift of the resonance frequency, which can be predicted by solving the correct dispersion relation. However, wearable antennas in garments are actually subjected to varying bending conditions when deployed on persons with different body morphologies. Therefore, a fast and accurate design tools quantifying the uncertainty due to bending along different curvature radii is needed. We present such a technique based on generalised polynomial chaos combined with the cavity model of Chapter 3. The non-intrusive stochastic method solves the corrected dispersion relation for the resonance frequencies of a set of radius of curvature realisations. These radii correspond to the Gauss quadrature points belonging to the orthogonal polynomials having the probability density function of the random variable as a weighting function. The formalism is applied to different distributions for the radius of curvature, either using a priori known or on-the-fly constructed sets of orthogonal polynomials. The accuracy and efficiency of the approach are shown by comparison to Monte Carlo simulations and by experimental validation.

4.1 Introduction

In the last decade, we witnessed a rapid growth of smart textiles and interactive fabrics, where electronic circuits capable of sensing and communicating with their environment are integrated in apparel. As key components of these systems, the design of textile antennas needs special care [1]–[4]. Wearable antenna garments may be subjected to bending and crumpling [5]. Moreover, their radiation efficiency may drop due to proximity of the human body. Whereas the latter problem is easily countered by adopting a microstrip patch antenna topology with a sufficiently large ground plane, the former is typically mitigated by overspecifying the requirements for the antenna in planar state. The designer then aims for a larger bandwidth and a higher return loss than actually required in the intended application. Yet, this approach may increase effects of out-of-band interference and cost of the system. A more judicious design requires that deterministic full-wave electromagnetic solvers be extended with stochastic methods that statistically quantify randomness in the antenna's figures of merit, allowing to capture the effect of uncertainty in the wearable antenna's performance parameters due to variations in, for example, the radius of curvature of the flexible antenna due to

1. movements and activity of one wearer;
2. variations in body morphology when deploying a wearable antenna on different persons.

This chapter specifically focuses on the second scenario, as our experiments demonstrated that movements in the first scenario do not lead to large variations in the curvature radius, resulting in a negligible shift of the resonance frequency.

As Monte-Carlo simulations require many realisations to accurately capture the statistics of the random process, they are too time-consuming to be used as design tools. Therefore, generalised polynomial chaos [6] was introduced as a more effective way to rapidly model uncertainty due to variations in the input parameters. Recently, in addition to techniques that quickly determine lower-order statistical moments [7], many new intrusive and non-intrusive procedures were proposed [8] and applied to transmission lines [9]–[11] and multiport microwave circuits [12]. Yet, none of them is dedicated to antenna design. In particular, the proposed techniques are suitable to describe simple variations in the geometry, but become very complex when modelling curved antennas at different bending radii, to characterise the uncertainty on the resonance frequency due to randomness in the radius of curvature. For this problem, the stochastic full-wave approach is still too CPU-intensive and a designer might want to rely on a faster, albeit more approximate, technique to estimate the probability density function of an antenna performance characteristic due to variations in the antenna geometry.

Therefore, we propose a new efficient formalism that provides a fast and accurate description of the statistics of the resonance frequency thanks to

1. the use of a recently proposed cavity model for curved microstrip patch antennas [13] that empirically accounts for textile substrate compression and subsequent change in substrate height and permittivity occurring when bending textile antennas;

2. the application of a non-intrusive generalised polynomial chaos formalism [14] that takes as inputs the solutions of the dispersion equation of the cavity model for radii of curvature coinciding with the quadrature points that correspond to the orthogonal polynomials having as a weighting function the probability density function of the input random variable.

This set of orthogonal polynomials is either readily available, such as the Legendre polynomials for a uniform distribution, or, for an arbitrary distribution [15], constructed on-the-fly by applying the Modified Chebychev algorithm [16] followed by the Golub-Welsch algorithm [17] to obtain the quadrature points and weights.

In Section 4.2 the non-intrusive polynomial chaos theory is applied to determine the statistics of the resonance frequencies of the textile patch antenna for a given statistical distribution of the radius of curvature. In Section 4.3 the novel technique is validated both numerically and experimentally. First, a numerical verification is performed for different distributions of the input random variable, being a Gaussian, uniform and truncated Gaussian distribution for the radius of curvature of the patch antenna, by comparing the probability density function obtained with the new method to the distribution found by applying Monte Carlo simulations. Next, the technique is experimentally validated by means of a real-life example considering the deployment of textile patch antennas on human arms. The conclusions are summarised in Section 4.4.

4.2 Statistics of the resonance frequency of a curved textile patch antenna

We now combine the dedicated cavity model for curved textile patch antennas with a non-intrusive generalised polynomial chaos algorithm to determine the statistics of the resonance frequency based on a minimal number of realisations.

4.2.1 Non-intrusive generalised polynomial chaos

Assume that an input random variable X, in our case the radius of curvature of a bent textile antenna, is given and that we want to determine the variation on the output variable Y, in our case the resonance frequency of the patch, due to the statistical variation of X, following the cumulative distribution function $\mathcal{P}^X$ and probability density function $d\mathcal{P}^X$ in the sample space Ω. To determine statistics of Y, we rely on the Wiener-Askey scheme [8] to approximate the transformation

$Y = f(X)$ by the polynomial expansion of order P

$$Y \approx f^P(X) = \sum_{k=0}^{P} y_k^X \phi_k^X(X). \tag{4.1}$$

An optimal expansion is obtained when the set of expansion polynomials forms a complete orthogonal basis in Ω with orthogonality relation

$$\begin{aligned} \left\langle \phi_i^X(x), \phi_j^X(x) \right\rangle &= \int_\Omega \phi_i^X(x) \phi_j^X(x) d\mathcal{P}^X(x) \\ &= \left\langle \left(\phi_i^X\right)^2 \right\rangle \delta_{ij}. \end{aligned} \tag{4.2}$$

In this case, the Cameron-Martin's convergence theorem ensures exponential convergence to the function $Y = f(X)$ for $P \to \infty$. By relying on the Askey scheme, we can directly make use of several families of orthogonal polynomials corresponding to well-established distributions $d\mathcal{P}^X(x)$, as shown in Table 4.1 [6]. To determine the unknown expansion coefficients y_k^X, we apply Galerkin weighting to (4.1) and make use of (4.2) to obtain

$$y_j^X = E[Y(x)\phi_j^X(x)] = \int_\Omega Y(x)\phi_j^X(x) d\mathcal{P}^X(x). \tag{4.3}$$

We can now conveniently approximate the integral by a suitable N-point Gauss quadrature rule, being

$$y_j^X \approx \sum_{i=1}^{N} w_i Y(x_i) \phi_j^X(x_i), \qquad j = 0, 1, \ldots, P. \tag{4.4}$$

where the quadrature points x_i are given by the N zeros of $\phi_N^X(x)$ in Ω and with w_i the corresponding weights. In order to evaluate (4.4), we must evaluate $Y = f(X)$ for N realisations of the random variable X corresponding to the quadrature points. In contrast to intrusive methods, this technique may be applied to any function or procedure taking x_i as an input and yielding $Y(x_i)$ as an output. Here, we apply the non-intrusive formalism to the cavity model of Chapter 3.

Note that, in order to evaluate the moments of the output distribution $\mathcal{P}^Y$, we do not need to revert to (4.1), as they might be directly computed based on the knowledge of the $Y(x_i)$ generated in order to calculate (4.4). Indeed, we have that

$$\begin{aligned} E[g(y)] &= \int_{\Omega_y} g(y) d\mathcal{P}^Y(y) \\ &= \int_\Omega g(Y(x)) d\mathcal{P}^X(x) \approx \sum_{i=1}^{N} w_i g\left[Y(x_i)\right], \end{aligned} \tag{4.5}$$

for an arbitrary function $g(y)$.

Table 4.1: The correspondence of the type of Wiener-Askey polynomial chaos and their underlying continuous random variables.

Random variable distribution	Wiener-Askey polynomials	Support
Gaussian	Hermite polynomials	$(-\infty, \infty)$
Gamma	Laguerre polynomials	$[0, \infty)$
Beta	Jacobi polynomials	$[a, b]$
Uniform	Legendre polynomials	$[a, b]$

4.2.2 On-the-fly construction of the orthogonal polynomials $\phi_j^X(x)$

Although the Askey scheme provides analytic expressions for sets of orthogonal polynomials corresponding to many widely-used distributions, many practical cases exist where the required set is not readily available for the distribution at hand. Assume, for example, that the radius of curvature is distributed following a normal distribution. The infinite support of the Gauss distribution is not compatible with the practical fact that textile antennas deployed on the human body only have a positive radius of curvature. This means that, in practice, we must truncate the normal distribution to a finite support. In this case, we do not have a set of orthogonal polynomials readily available. Therefore, we on-the-fly construct the set of polynomials that are orthogonal to the truncated Gaussian distribution as a weighting function. Although many techniques exist to orthogonalise monic polynomials, the problem is known to be notoriously ill-conditioned. We start from the set of Hermite polynomials corresponding to the Gauss distribution with infinite support and use the Modified Chebychev algorithm [16] to transform the recurrence relation for Hermite polynomials to a recurrence relationship for polynomials orthogonal to the truncated normal distribution. Next, we apply the Golub-Welsch algorithm [17] to derive the quadrature points x_i and weights w_i required to evaluate (4.4). This procedure can be used to construct a set of orthogonal polynomials for any arbitrary distribution of the input random variables.

The modified Chebychev algorithm

The modified Chebychev algorithm is a moment-based method that allows to transform a set of orthogonal polynomials to a new set of polynomials, orthogonal over a new domain. It can be applied with any system of monic polynomials satisfying a three-term recurrence relation.

Define the original set of monic orthogonal polynomials with respect to measure $\mathrm{d}l$ as

$$p_{k+1}(t) = (t - a_k)p_k(t) - b_k p_{k-1}(t), \qquad k = 0, 1, 2, \ldots \tag{4.6}$$

with $p_{-1}(t) = 0$, $p_0(t) = 1$, $a_k \in \mathbb{R}$ and $b_k \geq 0$. The three-term recurrence relation of the new set, with respect to measure $\mathrm{d}\lambda$, is defined as

$$\pi_{k+1}(t) = (t - \alpha_k)\pi_k(t) - \beta_k \pi_{k-1}(t), \qquad k = 0, 1, 2, \ldots \tag{4.7}$$

with $\pi_{-1}(t) = 0$ and $\pi_0(t) = 1$. This new set can also be written as

$$\begin{aligned} \pi_k &= p_k + \mathcal{O}(k-1), \\ &= (t - a_{k-1})p_{k-1}(t) - b_{k-1}p_{k-2}(t) + \mathcal{O}(k-1), \\ &= t p_{k-1}(t) + \mathcal{O}(k-1), \end{aligned} \tag{4.8}$$

where $\mathcal{O}(k-1)$ stands for a polynomial of order $k-1$.

Now the *mixed moments* can be introduced:

$$\sigma_{kl} = \int \pi_k(t) p_l(t)\, \mathrm{d}\lambda(t), \qquad k, l \geq -1. \tag{4.9}$$

Note that by orthogonality $\sigma_{kl} = 0$ for $k > l$ and from (4.8), we obtain

$$\int \pi_k^2(t)\, \mathrm{d}\lambda(t) = \int \pi_k(t) t p_{k-1}(t)\, \mathrm{d}\lambda(t) = \sigma_{kk}, \qquad k \geq 1. \tag{4.10}$$

The coefficients α_k and β_k in (4.7) are found from $\sigma_{k+1,k-1} = 0$ and $\sigma_{k+1,k} = 0$. Indeed, $\sigma_{k+1,k-1} = 0$ yields

$$\begin{aligned} 0 &= \int \big((t - \alpha_k)\pi_k(t) - \beta_k \pi_{k-1}(t)\big)\, p_{k-1}(t)\, \mathrm{d}\lambda(t), \\ &= \sigma_{kk} - \beta_k \sigma_{k-1,k-1}, \end{aligned} \tag{4.11}$$

whereas $\sigma_{k+1,k} = 0$ leads to

$$\begin{aligned} 0 &= \int \big((t - \alpha_k)\pi_k(t) - \beta_k \pi_{k-1}(t)\big)\, p_k(t)\, \mathrm{d}\lambda(t), \\ &= \int \pi_k(t) t p_k(t)\, \mathrm{d}\lambda(t) - \alpha_k \sigma_{kk} - \beta_k \sigma_{k-1,k}, \\ &= \sigma_{k,k+1} + (a_k - \alpha_k)\sigma_{kk} - \beta_k \sigma_{k-1,k}. \end{aligned} \tag{4.12}$$

Hence, from (4.11) and (4.12), we find that

$$\beta_k = \frac{\sigma_{kk}}{\sigma_{k-1,k-1}}, \tag{4.13a}$$

$$\alpha_k = a_k + \frac{\sigma_{k,k+1}}{\sigma_{kk}} - \frac{\sigma_{k-1,k}}{\sigma_{k-1,k-1}}, \tag{4.13b}$$

$$\sigma_{kl} = \sigma_{k-1,l+1} - (\alpha_{k-1} - a_l)\sigma_{k-1,l} - \beta_{k-1}\sigma_{k-2,l} + b_l \sigma_{k-1,l-1}, \tag{4.13c}$$

which allows us to recursively determine α_k and β_k.

The Golub-Welsch algorithm

Once the three-term recurrence relation for the new monic polynomials is known, the Golub-Welsch algorithm can be applied to calculate the Gauss quadrature rules. Therefore, start by identifying the recurrence relation (4.7) with the following matrix equation

$$t\begin{pmatrix}\pi_0(t)\\ \pi_1(t)\\ \pi_2(t)\\ \vdots\\ \pi_{N-1}(t)\end{pmatrix}=\begin{pmatrix}\alpha_0 & 1 & & & \\ \beta_1 & \alpha_1 & 1 & & \\ & \beta_2 & \alpha_2 & 1 & \\ & & \ddots & \ddots & \ddots\\ & & & \beta_{N-1} & \alpha_{N-1}\end{pmatrix}\begin{pmatrix}\pi_0(t)\\ \pi_1(t)\\ \pi_2(t)\\ \vdots\\ \pi_{N-1}(t)\end{pmatrix}+\begin{pmatrix}0\\ 0\\ 0\\ \vdots\\ \pi_N(t)\end{pmatrix}, \tag{4.14}$$

or equivalently

$$t\mathbf{p}(t)=T\mathbf{p}(t)+\pi_N(t)\mathbf{e}_n, \tag{4.15}$$

with $\mathbf{e}_n=(0,0,\ldots,1)^T$. It is shown in [18] that if the polynomials are orthonormal, T becomes a symmetric matrix. In the case where T is not symmetric, a diagonal similarity transformation can be performed

$$DTD^{-1}=J=\begin{pmatrix}\alpha_0 & \sqrt{\beta_1} & & & \\ \sqrt{\beta_1} & \alpha_1 & \sqrt{\beta_2} & & \\ & \sqrt{\beta_2} & \alpha_2 & \sqrt{\beta_3} & \\ & & \ddots & \ddots & \ddots\\ & & & \sqrt{\beta_{N-1}} & \alpha_{N-1}\end{pmatrix}. \tag{4.16}$$

As already mentioned in Section 4.2.1, the quadrature points are the zeros of $\pi_N(t)$ and from (4.15) it is clear that $\pi_N(t_j)=0$ only if $t_j\mathbf{p}(t_j)=T\mathbf{p}(t_j)$, where t_j is an eigenvalue of the tridiagonal matrix T. Remark that the eigenvalues of T and J are identical because of the similarity transformation. The quadrature weights w_j are found via the following property [18]:

$$w_j[\mathbf{p}(t_j)]^T[\mathbf{p}(t_j)]=1,\qquad j=1,2,\ldots,N. \tag{4.17}$$

Now, since the eigenvectors $\mathbf{q}(t_j)=(q_0(t_j),q_1(t_j),\ldots,q_{N-1}(t_j))^T$ of J correspond to orthonormal polynomials, we get

$$[\mathbf{q}(t_j)]^T[\mathbf{q}(t_j)]=1. \tag{4.18}$$

The orthogonal eigenvectors $\mathbf{p}(t_j)$ and $\mathbf{q}(t_j)$ only scale by a constant ω, since their corresponding matrices are similar. This means that (4.17) can be written as

$$w_j\omega^2[\mathbf{q}(t_j)]^T[\mathbf{q}(t_j)]=w_j\omega^2=1. \tag{4.19}$$

The weights w_j are thus easily derived from the eigenvectors of J. It suffices to consider 1 component of each eigenvector in order to determine these weights

$$w_j = \frac{q_0^2(t_j)}{\pi_0^2(t_j)} = q_0^2(t_j). \tag{4.20}$$

4.3 Results

We now illustrate our approach for different textile patch antenna prototypes subjected to cylindrical bending when deployed on an arm or a leg. The ability to isolate variations in the antenna's figures of merit due to bending only is an important asset of the non-intrusive polynomial chaos approach. Indeed, conventional techniques that merely rely on measurements of textile antenna prototypes can only characterise the overall variations due to the aggregate effect of many different adverse factors. To keep this chapter concise, we concentrate on bending in the direction of the patch width W_p only, solving the transcendental equation (3.14), since bending in this direction gives rise to the largest variation in the resonance frequency of the antenna. However, if one is also interested in studying or adding effects originating from fabrication tolerances, humidity, temperature, etc., it is sufficient to replace the dispersion relation by a different relation that takes these effects into account and apply the same technique on it. In a similar fashion, variations in the figures of merit of other antenna types, such as dipole antennas, may be studied.

In a first part, our technique based on generalised polynomial chaos is numerically validated in terms of speed and accuracy by comparison to a Monte Carlo approach for different distributions for the radius of curvature. Experimental validation is performed in a second part by means of a real-life example. It will also be shown that the distributions and their parameters used in the first part indeed correspond to real-life applications.

4.3.1 Numerical validation

For the numerical validation, let us use the five prototypes of Chapter 3, constructed on different flexible materials and exhibiting different specifications. The dimensions of each prototype are repeated in Table 4.2.

We consider two nominal application scenarios where the prototype 2 textile antenna is bent in the direction of the patch width W_p: a textile antenna deployed on the human leg, with an average radius of curvature $\overline{R} = 10$ cm and a flexible antenna deployed on the human arm, corresponding to a mean radius of curvature $\overline{R} = 5$ cm. We now assume that, due to variations in body morphologies of multiple persons, the radius of curvature behaves as a random variable following a Gaussian distribution. Due to the infinite support of the normal distribution, we

Table 4.2: Parameters of the prototypes.

Prototype	L_p [mm]	W_p [mm]	h [mm]	y_f [mm]	ϵ_r	d
1	81.2	69.25	2	16	1.75	0.5
2	81.2	69.25	2	16	1.75	1
3	78.5	69.3	2.7	17	1.715	1
4	52.5	43.7	2.7	11	1.715	1
5	78.5	68.3	4.04	16.8	1.715	1

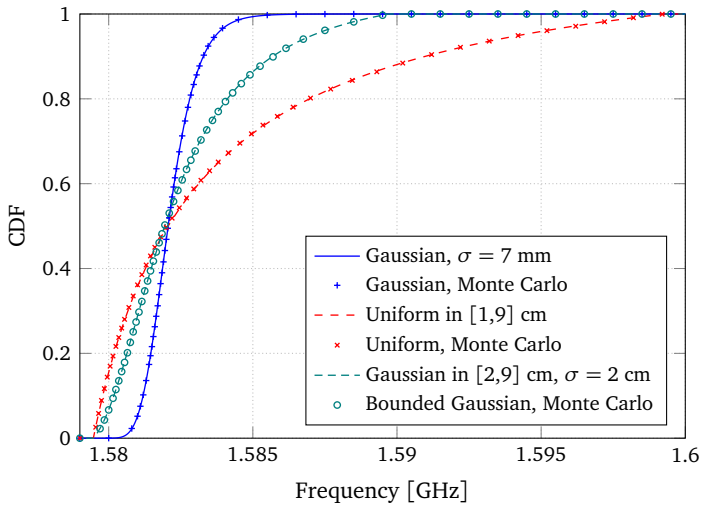

Figure 4.1: CDFs of the resonance frequency for the prototype 2 textile antenna deployed on the arm with a mean radius of curvature $\overline{R} = 5$ cm, assuming a Gaussian distribution with standard deviation $\sigma = 7$ mm, a uniform distribution over the interval [1 cm, 9 cm], and a Gaussian distribution truncated to the interval [2 cm, 9 cm] with standard deviation $\sigma = 2$cm.

need to restrict the range of acceptable values for the standard deviation in order to avoid unrealistic (negative) values for the radius of curvature. Assuming a uniform distribution, by relying on a set of Legendre polynomials, and a truncated Gaussian distribution, using a set of on-the-fly constructed orthogonal polynomials following Section 4.2.2, allows us to consider larger variations for the radius of curvature.

Let us first compare the distributions obtained for prototype 2 based on non-intrusive generalised polynomial chaos and Monte Carlo simulations. Fig. 4.1 presents the cumulative distribution functions (CDFs) obtained for the textile antenna deployed on a human arm with a mean radius of curvature $\overline{R} = 5$ cm,

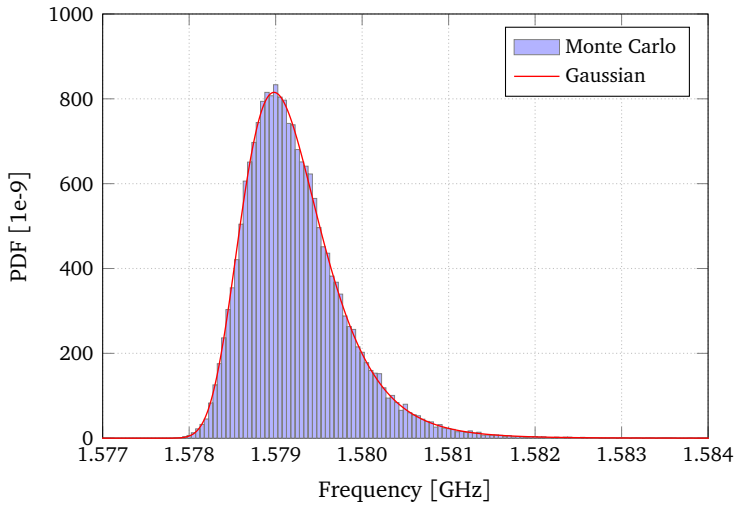

Figure 4.2: PDF of the resonance frequency for the prototype 2 textile antenna deployed on the leg assuming a Gaussian distributed radius of curvature with mean $\overline{R} = 10$ cm and standard deviation $\sigma = 17$ mm.

considering a Gaussian distribution with standard deviation $\sigma = 7$ mm, a uniform distribution over the interval [1 cm, 9 cm], and a Gaussian distribution truncated to the interval [2 cm, 9 cm] with standard deviation $\sigma = 2$ cm. An excellent agreement is found between our non-intrusive generalised polynomial chaos method and the Monte Carlo approach. Yet, on the one hand, to apply the Monte Carlo technique, the dispersion relation (3.14) is evaluated for 50 000 realisations on an Intel® Core™ i7-2760QM CPU operating at 2.40 GHz with 8 GB RAM using Mathematica 8.0, taking 4 min 51 s, 5 min 21 s, and 5 min 10 s of CPU-time for the Gaussian, uniform and truncated Gaussian distributions, respectively. In order to apply the non-intrusive polynomial chaos, on the other hand, adopting a conservative strategy for all distributions considered, we evaluated (4.4) at 33 quadrature points, requiring 1.4 s to compute the dispersion relation (3.14) at these points.

Fig. 4.2 presents the probability density function (PDF) when the prototype 2 textile antenna is deployed on a human leg and subjected to bending following a Gaussian distributed radius of curvature along the patch width W_p with mean $\overline{R} = 10$ cm and standard deviation $\sigma = 17$ mm. For this small σ, the distribution of the resonance frequency does not differ that much from a Gaussian distribution. Due to the non-linear dependence of the resonance frequency on the bending radius, we see that the output PDF exhibits a slight positive skew of 1.319 (1.325 based on the Monte Carlo simulation). Yet, we notice a good agreement with the Monte Carlo simulation when using Hermite polynomials up to order $P = 3$ in the

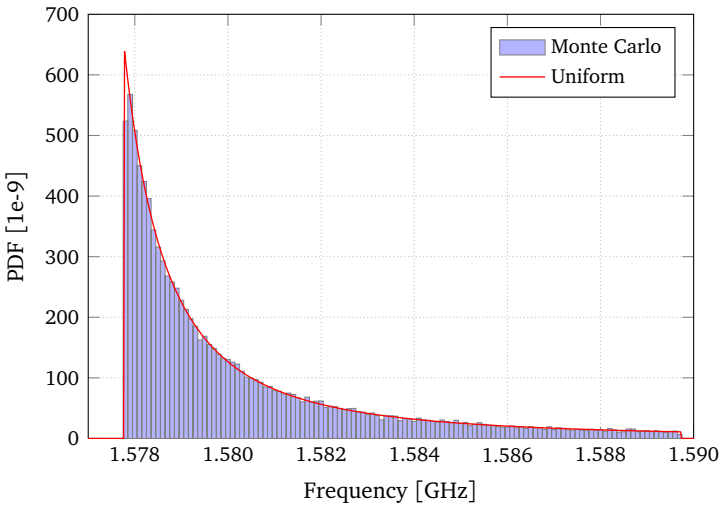

Figure 4.3: PDF of the resonance frequency for the prototype 2 textile antenna deployed on the leg considering a uniformly distributed radius of curvature in the interval [2 cm, 18 cm].

Wiener-Askey expansion (4.1).

When the radius of curvature is uniformly distributed over an interval of width 16 cm centred around $\overline{R} = 10$ cm, in Fig. 4.3 we observe that the output PDF for the resonance frequency differs a lot from the uniform input distribution. The skewness of the output distribution has now increased to 1.579 (an identical value is found using Monte Carlo simulation). We obtain a good agreement between the Monte-Carlo simulation and the generalised polynomial chaos based on Legendre polynomials of orders up to $P = 21$.

Next, we consider a Gaussian distribution around the mean bending radius $\overline{R} = 10$ cm that is truncated to the interval [2 cm, 30 cm]. As the distribution's support is now finite, compared to the complete Gaussian distribution, we may increase the standard deviation now to $\sigma = 5$ cm. For illustrative purposes, we deliberately chose to make the input distribution asymmetrical, exhibiting a positive skew of 0.35. The modified Chebychev algorithm is then applied to generate the appropriate basis of orthogonal polynomials after which the $N = 33$ quadrature points follow from the Golub-Welsch algorithm. The output PDF for the resonance frequency shown in Fig. 4.4, generated using the basis of on-the-fly constructed polynomials to construct the generalised polynomial expansion (4.1) of order up to $P = 16$, is in excellent agreement with the histogram generated using the Monte Carlo data. The PDF now exhibits a skewness of 2.004 (2.026 based on the Monte Carlo simulation).

To investigate the convergence of the generalised polynomial chaos expansion

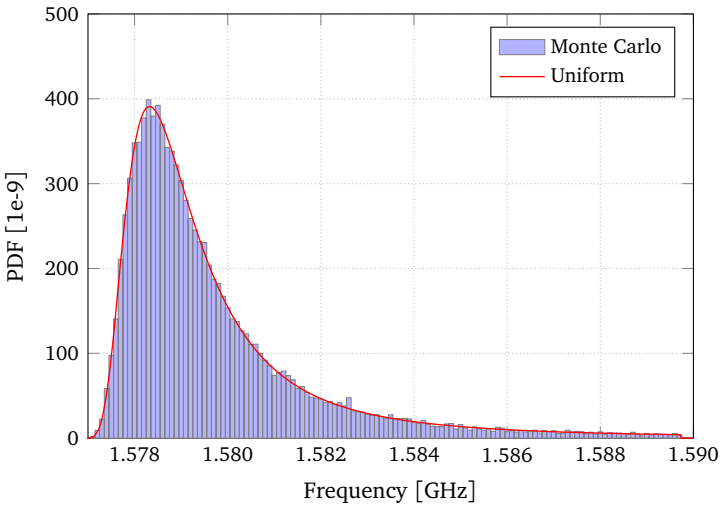

Figure 4.4: PDF of the resonance frequency for the prototype 2 textile antenna deployed on the leg considering a Gaussian distributed radius of curvature truncated to the interval [2 cm, 30 cm] with mean $\overline{R} = 10$ cm and standard deviation $\sigma = 5$cm.

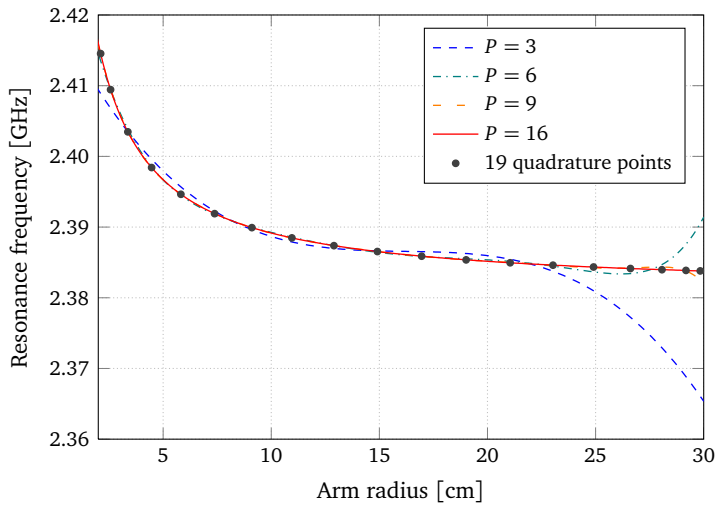

Figure 4.5: Prototype 4 bent around a human leg with a radius of curvature following a Gaussian distribution truncated to the interval [2 cm, 30 cm] with mean $\overline{R} = 10$ cm and standard deviation $\sigma = 5$ cm. Polynomial chaos expansion $f^P(X)$ for different maximum polynomial orders P.

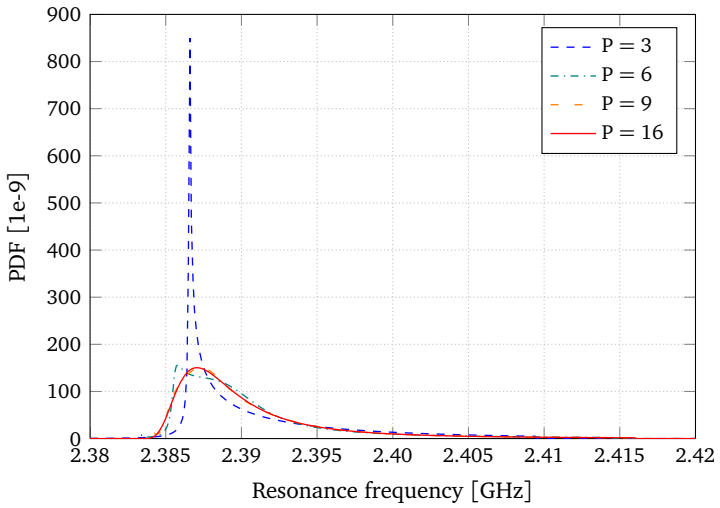

Figure 4.6: Prototype 4 bent around a human leg with a radius of curvature following a Gaussian distribution truncated to the interval [2 cm, 30 cm] with mean $\overline{R} = 10$ cm and standard deviation $\sigma = 5$ cm. PDF of the output random variable for different maximum polynomial orders *P*.

(4.1) as a function of the maximum polynomial order P, we consider prototype 4, which is a textile patch antenna resonating close to the 2.45 GHz ISM band. We assume that the antenna is bent along the W_p direction around a human leg, and that the radius of curvature follows a truncated Gaussian in the interval [2 cm, 30 cm] with mean $\overline{R} = 10$ cm and standard deviation $\sigma = 5$ cm. In Fig. 4.5 we plot the function $f^P(X)$, transforming the input random variable, being the bending radius R, to the output random variable, being the resonance frequency f_r, for different polynomial orders P. In the process, we reduced the number of quadrature points from 33 to 19, as it was found that this does not significantly reduce the accuracy of the expansion coefficients. These 19 quadrature points used in (4.4) are also plotted in Fig 4.5. Fig. 4.6 shows the corresponding effect of the expansion order P on the probability density function. One notices that the expansion up to order $P = 3$ only provides a poor fit to the output distribution, whereas for $P = 6$ and $P = 9$, the approximation starts to converge to the actual PDF, exhibiting Gibbs-like oscillations that decrease with higher values of P. For $P = 16$, the PDF has fully converged to the correct function $Y = f(X)$.

Table 4.3 provides the median resonance frequency and the 90% confidence interval, bounded by the 5^{th} and 95^{th} percentiles when bending the different textile antenna prototypes along the W_p direction around a human arm with a radius of curvature following a Gaussian distribution truncated to the interval [2 cm, 9 cm] with mean $\overline{R} = 5$ cm and standard deviation $\sigma = 2$ cm. The resonance frequency of prototype 1 at 1.57 GHz in planar state exhibits a negligible shift to a median

Table 4.3: Statistical properties of the resonance frequencies when positioning different prototypes on a human arm with a radius of curvature following a Gaussian distribution truncated to the interval [2 cm, 9 cm] with mean $\overline{R} = 5$ cm and standard deviation $\sigma = 2$ cm. (numbers between parentheses: results obtained by means of Monte Carlo simulations)

Prototype	median [GHz]	5^{th} percentile [GHz]	95^{th} percentile [GHz]
1	1.5701	1.57004	1.57037
	(1.5701)	(1.57004)	(1.57036)
2	1.58194	1.57989	1.58707
	(1.58194)	(1.57989)	(1.58703)
3	1.55299	1.54975	1.56098
	(1.55297)	(1.54975)	(1.56092)
4	2.3964	2.39113	2.40942
	(2.39637)	(2.39114)	(2.40948)
5	1.53585	1.53124	1.54661
	(1.53584)	(1.53123)	(1.54673)

frequency of 1.5701 GHz with a very narrow 90% confidence interval spanning 320 kHz. The fact that the resonance frequency remains very stable when bending the antenna results from the use of the stretchable electro-textile Flectron as conductive material for antenna patch and ground plane. When applying copper foil for the antenna patch and the ground plane, as for antenna prototype 2, we notice a significant shift in resonance frequency from 1.576 GHz in planar state to a median resonance frequency of 1.58194 GHz in bent state, with a 90% confidence interval spanning 7.2 MHz. Similar behaviour is observed for the cotton-based prototype 3 where the resonance frequency of 1.5435 GHz in planar state shifts to a median resonance frequency of 1.55299 GHz in bent state, with a 90% confidence interval spanning 11.2 MHz. Prototype 5, for which a thicker antenna substrate was used, exhibits a larger resonance frequency shift from 1.522 GHz in planar state to a median resonance frequency of 1.53585 GHz in bent state, with a broader 90% confidence interval spanning 15.4 MHz. Prototype 4, operating close to the 2.45 GHz ISM band with a resonance frequency of 2.381 GHz, has its resonance frequency shifted to a median resonance frequency of 2.3964 GHz in bent state, with a 90% confidence interval spanning 18.3 MHz.

Table 4.4 provides the median resonance frequency and the 90% confidence interval, when bending the different textile antenna prototypes along the W_p direction around a human leg with a radius of curvature following a Gaussian distribution truncated to the interval [2 cm, 30 cm] with mean $\overline{R} = 10$ cm and standard deviation $\sigma = 5$ cm. Similar conclusions can be drawn as for the antennas deployed on the arm.

Table 4.4: Statistical properties of the resonance frequencies when positioning different prototypes on a human leg with a radius of curvature following a Gaussian distribution truncated to the interval [2 cm, 30 cm] with mean $\overline{R} = 10$ cm and standard deviation $\sigma = 5$ cm. (numbers between parentheses: results obtained by means of Monte Carlo simulations)

Prototype	median [GHz]	5^{th} percentile [GHz]	95^{th} percentile [GHz]
1	1.57002	1.57001	1.57019
	(1.57002)	(1.57001)	(1.57019)
2	1.57903	1.57773	1.5841
	(1.57903)	(1.57773)	(1.5841)
3	1.54838	1.54629	1.55638
	(1.54839)	(1.5463)	(1.55645)
4	2.3889	2.38553	2.40192
	(2.38889)	(2.38554)	(2.40192)
5	1.52925	1.52619	1.54052
	(1.52927)	(1.52617)	(1.5405)

4.3.2 Experimental validation

In the previous part, the proposed technique was validated for different probability distribution functions for the curvature radius of textile antennas. However, in real-life applications, this distribution is mostly not readily available and must be fitted on measured sample data. We now demonstrate how this fitted analytical PDF then forms the starting point for our technique.

Consider the design of a textile antenna, similar to prototype 2, that has to be worn on a human arm. Since we focus on the fluctuations in arm radius for persons with different morphology wearing the antenna, the PDF of the arm radius for a representative population needs to be known. This distribution can be derived from measurement campaigns, such as NHANES [19], that provide databases of sample data. Fig. 4.7 shows the histogram of the arm radius after measuring the arm circumference of 7,056 persons. It is compiled using freely available NHANES examination data of 2009-2010, selecting persons larger than 1.40 m and heavier than 40 kg. The histogram of the sampled measurement data is now approximated by an analytical PDF, where a truncated normal distribution in the interval [3 cm, 8 cm], with mean $\overline{R} = 5.14$ cm and $\sigma = 0.85$ cm provides a good fit. Remark that these parameters are in good agreement with the parameters used for numerical validation in Section 4.3.1. The fitted truncated Gaussian distribution is also displayed in Fig. 4.7.

Next, a measurement campaign was performed to construct the dispersion relation (3.14) that relates the arm radius to the measured antenna resonance frequency.

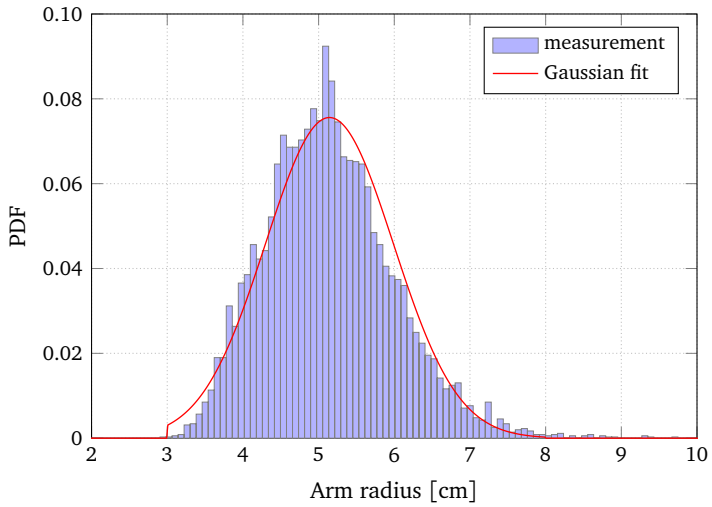

Figure 4.7: PDF of the arm radius of different people. NHANES data and truncated Gaussian in [3 cm, 8 cm] with mean $\overline{R} = 5.14$ cm and $\sigma = 0.85$ cm.

Therefore, a new textile antenna prototype was built and the resonance frequencies of the antenna in bent state were measured for different curvature radii, as displayed in Fig. 4.8. In order to find a good fit, the relative permittivity after compression, $\epsilon_{r,\text{comp}} = \epsilon_{r,\text{flat}} \left(1 + \eta \frac{h(d-0.5)}{R}\right)$, was optimised for both $\epsilon_{r,\text{flat}}$ and η by applying the least-squares method. The fitted dispersion curve is shown in Fig. 4.8 by the full line. For the error analysis, we also plotted the dispersion relation for $\epsilon_{r,\text{comp}} \pm 0.003$.

The resulting PDF of the resonance frequency is displayed in Fig. 4.9. The measured data is obtained by solving the fitted dispersion relation (3.14) with the optimised $\epsilon_{r,\text{comp}}$ for all 7,056 arm radii of the NHANES data set, requiring 59 s of CPU-time, whereas only 19 evaluations were needed to construct the modelled PDF, taking 0.5 s of CPU-time (with expansion order $P = 9$). A good agreement is found between the modelled and the measured data. The modelled PDFs are also shown for $\epsilon_{r,\text{comp}} \pm 0.003$ and one observes a shift of approximately 1 MHz due to the tolerance on the permittivity. Remark that the terms 'lower bound' and 'higher bound' correspond to the bounds defined in Fig. 4.8.

4.4 Conclusion

A new efficient stochastic design tool was introduced based on a non-intrusive generalised polynomial chaos expansion combined with a cavity model for textile antennas subject to cylindrical bending. The method predicts the cumulative dis-

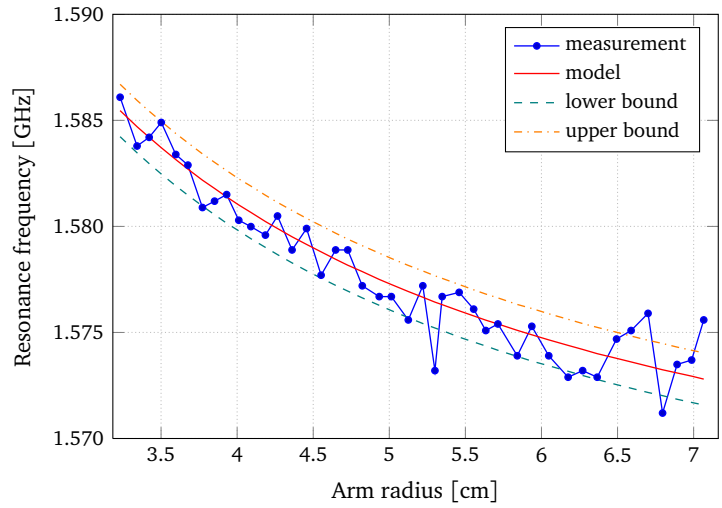

Figure 4.8: Resonance frequency as a function of the arm radius. Measurement data and fit.

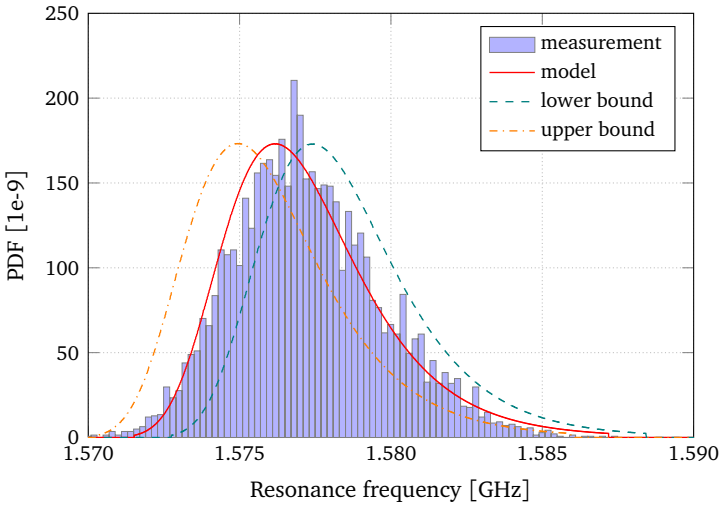

Figure 4.9: PDF of the resonance frequency. Measurement and fit.

tribution function, the probability density function, the confidence intervals and the moments of the statistical distribution of the resonance frequency when the radius of curvature of the textile patch is a random variable. The method can be applied for input distributions of the Askey family as well as to any arbitrary distribution. For the latter, the Modified Chebychev algorithm is applied to con-

struct the relevant set of orthogonal polynomials, followed by the Golub-Welsch algorithm to determine the quadrature points, for which the dispersion relation of the cavity model is solved. Comparison to Monte Carlo simulations and to experimental data demonstrates the accuracy and the large speed-up obtained by the new procedure.

References

[1] A. Tronquo, H. Rogier, C. Hertleer, and L. Van Langenhove, "Robust planar textile antenna for wireless body LANs operating in 2.45 GHz ISM band", *Electronics Letters*, vol. 42, no. 3, pp. 142–143, Feb. 2006.

[2] I. Locher, M. Klemm, T. Kirstein, and G. Troster, "Design and characterization of purely textile patch antennas", *IEEE Trans. Adv. Packag.*, vol. 29, no. 4, pp. 777–788, Nov. 2006.

[3] P. Salonen, L. Sydanheimo, M. Keskilammi, and M. Kivikoski, "A small planar inverted-F antenna for wearable applications", in *Wearable Computers, 1999. Digest of Papers. The Third International Symposium on*, 1999, pp. 95–100.

[4] C. Hertleer, H. Rogier, L. Vallozzi, and L. Van Langenhove, "A textile antenna for off-body communication integrated into protective clothing for firefighters", *IEEE Trans. Antennas Propag.*, vol. 57, no. 4, pp. 919–925, Apr. 2009.

[5] Q. Bai and R. Langley, "Crumpling of PIFA textile antenna", *IEEE Trans. Antennas Propag.*, vol. 60, no. 1, pp. 63–70, Jan. 2012.

[6] D. Xiu and G. E. Karniadakis, "The Wiener-Askey polynomial chaos for stochastic differential equations", *SIAM J. Sci. Comput.*, vol. 24, no. 2, pp. 649–644, Feb. 2002.

[7] O. Sy, M. van Beurden, B. Michielsen, J. Vaessen, and A. Tijhuis, "Second-order statistics of complex observables in fully stochastic electromagnetic interactions: applications to emc", *Radio Science*, vol. 45, no. 4, pp. 1–16, Aug. 2010.

[8] D. Xiu, "Fast numerical methods for stochastic computations: a review", *Commun. Comput. Phys.*, vol. 5, no. 2-4, pp. 242–272, Feb. 2009.

[9] D. Vande Ginste, D. De Zutter, D. Deschrijver, T. Dhaene, P. Manfredi, and F. Canavero, "Stochastic modeling-based variability analysis of on-chip interconnects", *IEEE Trans. Compon., Packag., Manuf. Technol. A*, vol. 2, no. 7, pp. 1182–1192, Jul. 2012.

[10] P. Manfredi and F. Canavero, "Polynomial chaos for random field coupling to transmission lines", *IEEE Trans. Electromagn. Compat.*, vol. 54, no. 3, pp. 677–680, Jun. 2012.

[11] H. Bagci, A. Yucel, J. Hesthaven, and E. Michielssen, "A fast Stroud-based collocation method for statistically characterizing EMI/EMC phenomena on complex platforms", *IEEE Trans. Electromagn. Compat.*, vol. 51, no. 2, pp. 301–311, May 2009.

[12] D. Spina, F. Ferranti, T. Dhaene, L. Knockaert, G. Antonini, and D. Vande Ginste, "Variability analysis of multiport systems via polynomial-chaos expansion", *IEEE Trans. Microw. Theory Tech.*, vol. 60, no. 8, pp. 2329–2338, Aug. 2012.

[13] F. Boeykens, L. Vallozzi, and H. Rogier, "Cylindrical bending of deformable textile rectangular patch antennas", *International Journal of Antennas and Propagation*, vol. 2012, 1–11, Article ID 170420, 2012.

[14] G. Poëtte and D. Lucor, "Non intrusive iterative stochastic spectral representation with application to compressible gas dynamics", *Journal of Computational Physics*, vol. 231, no. 9, pp. 3587–3609, May 2012.

[15] X. Wan and G. E. Karniadakis, "Beyond Wiener-Askey expansions: handling arbitrary PDFs", *Journal of Scientific Computing*, vol. 27, no. 1-3, pp. 455–464, Jun. 2006.

[16] W. Gautschi, *Orthogonal Polynomials: Computation and Approximation*. Oxford, 2004, p. 76.

[17] G. Golub and J. Welsch, "Calculation of Gauss quadrature rules", *Mathematics of Computation*, vol. 23, no. 106, pp. 221–230, Apr. 1969.

[18] H. S. Wilf, *Mathematics for the Physical Sciences*. Wiley, 1962.

[19] Centers for Disease Control and Prevention. (Sep. 2011). National Health and Nutrition Examination Survey, [Online]. Available: `http://www.cdc.gov/nchs/nhanes.htm`.

Part II

Hybrid Electromagnetic Modelling

5

Numerical Techniques for solving the Maxwell Equations

★ ★ ★

In the frequency domain, two major numerical techniques exist for simulating electromagnetic problems: the Finite Element (FE) method, which is powerful for modelling complex inhomogeneous problems, and the boundary integral equation (BIE) method, whose strength is to model homogeneous and unbounded domains. Both methods solve the Maxwell equations, albeit from a different viewpoint. In this chapter, the theory behind these two methods is presented in order to understand the construction of the hybrid FE-BIE system in Chapter 6.

5.1 A note on curl-conforming and div-conforming basis functions

When solving the Maxwell equations by means of numerical techniques, it is necessary to discretise certain quantities such as fields and currents, which are then represented by a linear combination of basis functions. In the process, it is important that some properties of the fields and currents are maintained. For the fields, this means that the basis functions have to maintain sufficient continuity to be differentiable via the curl operator, yielding a bounded, well-defined result without introducing Dirac delta distributions. Such basis functions are called curl-conforming basis functions and maintain first-order tangential vector continuity across cell edges. For the currents, the basis functions have to conserve enough continuity to be differentiable via the divergence operator. These basis functions

are called div-conforming basis functions and maintain first-order normal vector continuity across cell edges [1].

The function space in which the curl-conforming basis functions of a domain Ω exist, is denoted as $\mathsf{H}(\text{curl};\Omega)$. For the div-conforming basis functions, this becomes $\mathsf{H}(\text{div};\Omega)$. The traces of the basis functions on the boundary $\partial\Omega$ are defined in the spaces $\mathsf{H}^{-\frac{1}{2}}(\text{curl},\partial\Omega)$ and $\mathsf{H}^{-\frac{1}{2}}(\text{div},\partial\Omega)$, respectively. For more information over these function spaces, we refer the reader to [2], [3].

5.2 The finite element method

The FE method, as first described by Courant in 1942, is one of the most successful numerical techniques for solving different engineering problems. For a good overview of this method applied to electromagnetic problems, we refer the reader to [4]–[7].

In this thesis, the FE implementation by Agilent Technologies®, *EMPro* is used. This formulation solves the non-symmetric Maxwell equations (1.6) for the electric field $\mathbf{E}$ due to implied electric currents $\mathbf{J}^{\text{imp}}$. It is constructed by weighting the differential equations that describe the problem with the same basis functions that are used to discretise the electric field. Such a method, where the test and basis functions are equal, is called a Galerkin FE method and leads to a symmetric system matrix.

An important characteristic of the FE method is that it discretises the full 3D simulation domain. The basis functions in this domain only interact locally, leading to a sparse system matrix. A drawback, however, is that the domain has to be truncated, meaning that not the full 3D space is modelled. To compensate for the truncation error, different techniques can be applied, such as, e.g. imposing Absorbing Boundary Conditions [8].

5.2.1 Formulation

The FE formulation starts from the curl equations (1.6a) and (1.6b) and eliminates the magnetic field $\mathbf{H}$ in order to construct the wave equation for the electric field in a domain Ω

$$\frac{1}{\mu_r}\nabla\times(\nabla\times\mathbf{E}) - k_0^2\epsilon_r\cdot\mathbf{E} = -j\omega\mu_0\cdot\mathbf{J}^{\text{imp}}, \tag{5.1}$$

with $k_0 = \omega\sqrt{\epsilon_0\mu_0}$. The variational formulation is found after testing (5.1) with weighting functions $\mathbf{W}\in\mathsf{H}(\text{curl};\Omega)$:

$$\frac{1}{\mu_r}\int_\Omega \mathbf{W}\cdot\nabla\times(\nabla\times\mathbf{E})\ \mathrm{d}V - k_0^2\epsilon_r\int_\Omega \mathbf{W}\cdot\mathbf{E}\,\mathrm{d}V = -j\omega\mu_0\int_\Omega \mathbf{W}\cdot\mathbf{J}^{\text{imp}}\,\mathrm{d}V. \tag{5.2}$$

Applying the identity $\mathbf{A}\cdot(\nabla\times\mathbf{B}) = (\nabla\times\mathbf{A})\cdot\mathbf{B} - \nabla\cdot(\mathbf{A}\times\mathbf{B})$ on (5.2) and using the divergence theorem yields

$$\frac{1}{\mu_r}\int_\Omega (\nabla\times\mathbf{W})\cdot(\nabla\times\mathbf{E})\,\mathrm{d}V - k_0^2\epsilon_r\int_\Omega \mathbf{W}\cdot\mathbf{E}\,\mathrm{d}V \\ = j\omega\mu_0\int_{\partial\Omega}\mathbf{w}\cdot(\mathbf{n}\times\mathbf{H})\,\mathrm{d}S - j\omega\mu_0\int_\Omega \mathbf{w}\cdot\mathbf{J}^{\mathrm{imp}}\,\mathrm{d}V, \quad (5.3)$$

where $\mathbf{w}\in\mathsf{H}^{-\frac{1}{2}}(\mathrm{curl},\partial\Omega)$ is the trace of $\mathbf{W}$ on $\partial\Omega$. Here we have explicitly introduced the trace of the magnetic field $(\mathbf{n}\times\mathbf{H})$, since this term will later be used to couple the formulation with a BIE method.

5.2.2 Schur complement

Since a hybrid FE-BIE formulation only couples the boundary FE unknowns with the BIE unknowns, we can eliminate all internal FE unknowns by computing the Schur complement of the FE system matrix.

Consider the following FE system

$$\begin{pmatrix} A_{\Omega,\Omega} & A_{\Omega,\partial\Omega} \\ A_{\partial\Omega,\Omega} & A_{\partial\Omega,\partial\Omega}\end{pmatrix}\begin{pmatrix}\mathbf{X}_\Omega \\ \mathbf{X}_{\partial\Omega}\end{pmatrix} = \begin{pmatrix}\mathbf{B}_\Omega \\ 0\end{pmatrix}. \quad (5.4)$$

The submatrix $A_{\Omega,\Omega}$ represents the interactions from all internal unknowns, $A_{\partial\Omega,\partial\Omega}$ stands for the boundary unknown interactions, and $A_{\Omega,\partial\Omega}$ and $A_{\partial\Omega,\Omega}$ correspond to the interactions between the internal and boundary unknowns. After LU decomposition, this becomes

$$A = \begin{pmatrix} L_{\Omega,\Omega} & 0 \\ L_{\partial\Omega,\Omega} & I\end{pmatrix}\begin{pmatrix} U_{\Omega,\Omega} & U_{\Omega,\partial\Omega} \\ 0 & S\end{pmatrix}. \quad (5.5)$$

The Schur complement $\mathcal{S}$ is then defined as

$$\mathcal{S} = A_{\partial\Omega,\partial\Omega} - A_{\partial\Omega,\Omega}(A_{\Omega,\Omega})^{-1}A_{\Omega,\partial\Omega}. \quad (5.6)$$

In the FE method, the internal basis functions only interact locally. Therefore, given the sparseness of the system matrix, the Schur complement is calculated in order to obtain a smaller dense matrix. The calculation is performed using the efficient MUMPS[1] library. The FE unknowns then follow from

$$\begin{pmatrix} U_{\Omega,\Omega} & U_{\Omega,\partial\Omega} \\ 0 & S\end{pmatrix}\begin{pmatrix}\mathbf{X}_\Omega \\ \mathbf{X}_{\partial\Omega}\end{pmatrix} = \begin{pmatrix}\mathbf{B}'_\Omega \\ \mathbf{B}'_{\partial\Omega}\end{pmatrix} \quad (5.7)$$

[1] `http://graal.ens-lyon.fr/MUMPS/`

with

$$\begin{pmatrix} L_{\Omega,\Omega} & 0 \\ L_{\partial\Omega,\Omega} & I \end{pmatrix} \begin{pmatrix} \mathbf{B}'_{\Omega} \\ \mathbf{B}'_{\partial\Omega} \end{pmatrix} = \begin{pmatrix} \mathbf{B}_{\Omega} \\ 0 \end{pmatrix}. \tag{5.8}$$

By calculating the Schur complement, a relationship between the tangential trace of the electric field on the boundary $\mathbf{E}^t = \mathbf{n} \times (\mathbf{E} \times \mathbf{n})$ and the electric surface current $\mathbf{J} = \mathbf{n} \times \mathbf{H}$ is obtained. We get

$$\mathcal{S}\mathbf{E}^t = jk_0\eta_0 \left(\mathbf{J} - \mathbf{J}^{\text{imp}}\right), \tag{5.9}$$

with $\eta_0 = \sqrt{\mu_0/\epsilon_0}$. A scaled version of the Schur complement is the Poincaré-Steklov or Dirichlet-to-Neumann operator $\mathcal{Y}$, which relates the tangential electric field directly to the electric surface current

$$\mathcal{Y}\mathbf{E}^t = \mathbf{J} - \mathbf{J}^{\text{imp}}. \tag{5.10}$$

It is this representation that will be used to couple the FE method with the BIE method in Chapter 6.

5.2.3 Discretisation

EMPro applies up to second order curl-conforming basis functions to discretise the electric field. The first order basis functions are the standard edge elements [9], and the second order are the quadratic edge and quadratic face basis functions. In Fig. 5.1, a typical element for discretising the simulation domain is shown. Each tetrahedron is associated with 20 basis functions: one standard edge element for each edge, one quadratic edge basis function for each edge and two quadratic face basis functions for each face.

In order to define the basis functions, we first introduce the barycentric coordinates ξ_i as the normalised distances of a given point to the opposite face, such that ξ_i equals 1 at point $\mathbf{p}_i$ and zero at the opposing face. Following Fig. 5.1, this means that each point in the tetrahedron can be represented by its barycentric coordinates $(\xi_0, \xi_1, \xi_2, \xi_3)$. We can then define a standard edge element associated with edge $\mathbf{p}_0\mathbf{p}_1$ as

$$\xi_0 \nabla\xi_1 - \xi_1 \nabla\xi_0, \tag{5.11}$$

and the quadratic edge basis function as

$$\xi_0 \nabla\xi_1 + \xi_1 \nabla\xi_0. \tag{5.12}$$

The two quadratic face basis functions associated with face $\mathbf{p}_0\mathbf{p}_1\mathbf{p}_2$ are given by

$$4\xi_0 \left(\xi_1 \nabla\xi_2 - \xi_2 \nabla\xi_1\right), \tag{5.13a}$$

$$4\xi_1 \left(\xi_2 \nabla\xi_0 - \xi_0 \nabla\xi_2\right). \tag{5.13b}$$

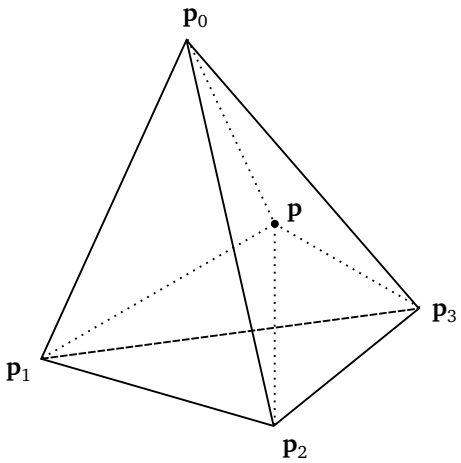

Figure 5.1: A typical element for discretising a 3D FE simulation domain. Any point $\mathbf{p}$ in this tetrahedron is represented by its barycentric coordinates $(\xi_0, \xi_1, \xi_2, \xi_3)$, where ξ_i represents the normalised distance of $\mathbf{p}$ to the plane opposing $\mathbf{p}_i$.

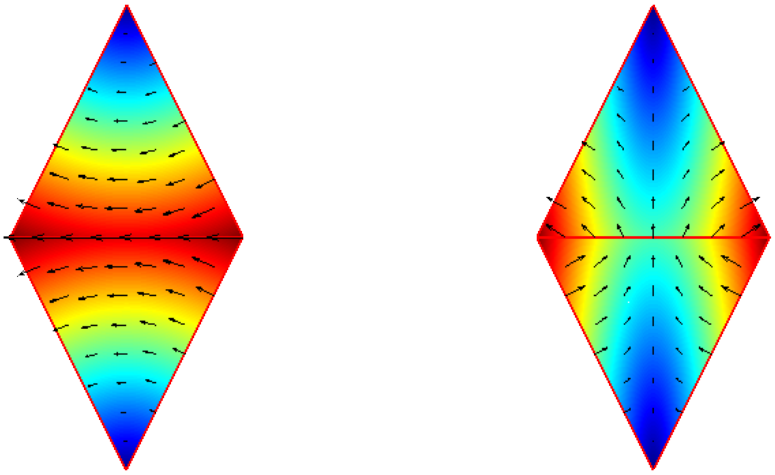

(a) (b)

Figure 5.2: Traces of FE edge basis functions: a standard first order edge element (a) and a quadratic edge basis (b).

Note that a third related face basis function can be constructed by a further cyclical rotation of the indices, but this does not expand the space spanned by taking the

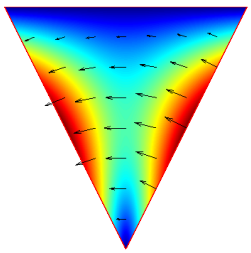

Figure 5.3: The trace of a second order FE face basis function.

curl of the full set of basis functions and is omitted.

The traces of these basis functions are important for the hybrid FE-BIE formulation, since they discretise $\mathbf{E}^t$ on the boundary of the FE domain. These traces are the 2D edge and face basis functions of which examples are displayed in Fig. 5.2 and Fig. 5.3.

5.3 Boundary integral equations

In contrast to the FE method, the BIE method does not immediately discretise the differential form of the Maxwell equations in three dimensions. It first solves them partially analytically in order to decrease the dimensions of the problem with one. As a result, only the boundaries of materials need to be discretised, what leads to a system with substantially less unknowns as compared to the FE method. Also, the simulation domain can be extended to the full open 3D space. Drawbacks are that this is only possible for configurations for which a Green's function is analytically available, such as homogeneous media and that the system matrix is now a dense matrix. For more information about this technique, see [10]–[12].

The derivation of the BIE formulation starts from the vector and scalar potentials, derived in Section 1.2.

5.3.1 Green's function

The Helmholtz equations (1.13) and (1.21) are solved by means of the Green's function. This function is a solution of

$$\nabla^2 G(\mathbf{r}) + k^2 G(\mathbf{r}) = -\delta(\mathbf{r}). \tag{5.14}$$

Given the symmetry of the problem, the solution $G(\mathbf{r})$ only depends on the radial coordinate r of the spherical coordinate system, thus $G(r)$. We then obtain

$$\frac{1}{r^2}\frac{d}{dr}r^2\frac{d}{dr}G(r) + k^2 G(r) = 0, \qquad r > 0. \tag{5.15}$$

The general solution of this equation is

$$G(r) = A\frac{e^{-jkr}}{r} + B\frac{e^{jkr}}{r}. \tag{5.16}$$

Since the wave cannot propagate from infinity (it must satisfy the radiation condition), $B = 0$ must hold. After integration of equation (5.14) over a sphere, we find

$$G(r) = \frac{e^{-jkr}}{4\pi r}. \tag{5.17}$$

Note that this Green's function is only valid for an open homogeneous region of infinite extent.

5.3.2 Integral representations

The solutions of (1.13) and (1.21) are found using the Green's function, with their source terms in the Maxwell equations (here represented as $s(\mathbf{r})$) written as

$$s(\mathbf{r}) = \int_V \delta(\mathbf{r}-\mathbf{r}')s(\mathbf{r}')\,\mathrm{d}V'. \tag{5.18}$$

The vector and scalar potentials are then related to the sources by

$$\mathbf{A}(\mathbf{r}) = \int_V G(|\mathbf{r}-\mathbf{r}'|)\mathbf{J}(\mathbf{r}')\,\mathrm{d}V', \tag{5.19a}$$

$$\mathbf{F}(\mathbf{r}) = \int_V G(|\mathbf{r}-\mathbf{r}'|)\mathbf{K}(\mathbf{r}')\,\mathrm{d}V', \tag{5.19b}$$

$$\phi(\mathbf{r}) = \frac{1}{\epsilon}\int_V G(|\mathbf{r}-\mathbf{r}'|)\rho(\mathbf{r}')\,\mathrm{d}V', \tag{5.19c}$$

$$\psi(\mathbf{r}) = \frac{1}{\mu}\int_V G(|\mathbf{r}-\mathbf{r}'|)\kappa(\mathbf{r}')\,\mathrm{d}V'. \tag{5.19d}$$

The electric and magnetic field in a certain point are given by (1.22) and become

$$\begin{aligned}\mathbf{E}(\mathbf{r}) = &-\nabla\times\int_V G(|\mathbf{r}-\mathbf{r}'|)\mathbf{K}(\mathbf{r}')\,\mathrm{d}V' - j\omega\mu\int_V G(|\mathbf{r}-\mathbf{r}'|)\mathbf{J}(\mathbf{r}')\,\mathrm{d}V' \\ &-\frac{1}{\epsilon}\nabla\int_V G(|\mathbf{r}-\mathbf{r}'|)\rho(\mathbf{r}')\,\mathrm{d}V',\end{aligned} \tag{5.20a}$$

$$\begin{aligned}\mathbf{H}(\mathbf{r}) = &\nabla\times\int_V G(|\mathbf{r}-\mathbf{r}'|)\mathbf{J}(\mathbf{r}')\,\mathrm{d}V' - j\omega\epsilon\int_V G(|\mathbf{r}-\mathbf{r}'|)\mathbf{K}(\mathbf{r}')\,\mathrm{d}V' \\ &-\frac{1}{\mu}\nabla\int_V G(|\mathbf{r}-\mathbf{r}'|)\kappa(\mathbf{r}')\,\mathrm{d}V'.\end{aligned} \tag{5.20b}$$

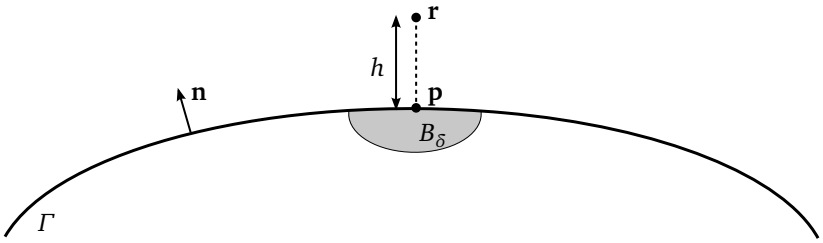

Figure 5.4: The fields in an observation point $\mathbf{r}$ near the surface Γ are calculated in two parts: a contribution from the small circle B_δ around $\mathbf{p}$, the projection of the observation point, and a contribution from the remaining part of the surface $\Gamma \backslash B_\delta$.

By applying the laws of charge conservation (1.3), electric and magnetic charges are eliminated and we get

$$\begin{aligned}\mathbf{E}(\mathbf{r}) = &-\nabla \times \int_V G(|\mathbf{r}-\mathbf{r}'|)\mathbf{K}(\mathbf{r}')\,\mathrm{d}V' - j\omega\mu \int_V G(|\mathbf{r}-\mathbf{r}'|)\mathbf{J}(\mathbf{r}')\,\mathrm{d}V' \\ &+ \frac{1}{j\omega\epsilon}\nabla \int_V G(|\mathbf{r}-\mathbf{r}'|)\nabla' \cdot \mathbf{J}(\mathbf{r}')\,\mathrm{d}V', \qquad (5.21a)\\ \mathbf{H}(\mathbf{r}) = &\nabla \times \int_V G(|\mathbf{r}-\mathbf{r}'|)\mathbf{J}(\mathbf{r}')\,\mathrm{d}V' - j\omega\epsilon \int_V G(|\mathbf{r}-\mathbf{r}'|)\mathbf{K}(\mathbf{r}')\,\mathrm{d}V' \\ &+ \frac{1}{j\omega\mu}\nabla \int_V G(|\mathbf{r}-\mathbf{r}'|)\nabla' \cdot \mathbf{K}(\mathbf{r}')\,\mathrm{d}V'. \qquad (5.21b)\end{aligned}$$

5.3.3 Traces of integral representations

To construct the BIE formulation, we need to consider the special case of a current distribution $\mathbf{X}(\mathbf{r}')$ located on a surface Γ, with outward normal $\mathbf{n}$. In order to calculate $\mathbf{E}(\mathbf{r})$ and $\mathbf{H}(\mathbf{r})$ for $\mathbf{r} \to \Gamma$, it is clear from (5.21) that the following limits then have to be computed:

$$\lim_{\mathbf{r}\to\Gamma} \int_\Gamma G(|\mathbf{r}-\mathbf{r}'|)\mathbf{X}(\mathbf{r}')\,\mathrm{d}S', \qquad (5.22a)$$

$$\lim_{\mathbf{r}\to\Gamma} \int_\Gamma \nabla G(|\mathbf{r}-\mathbf{r}'|)\nabla' \cdot \mathbf{X}(\mathbf{r}')\,\mathrm{d}S', \qquad (5.22b)$$

$$\lim_{\mathbf{r}\to\Gamma} \int_\Gamma \nabla \times G(|\mathbf{r}-\mathbf{r}'|)\mathbf{X}(\mathbf{r}')\,\mathrm{d}S'. \qquad (5.22c)$$

The first term contains a weakly singular integrand $\frac{1}{|\mathbf{r}-\mathbf{r}'|}$. Its limit value can be calculated by placing $\mathbf{r}$ on Γ and evaluating the integral as an improper integral.

The other terms contain the integrand $\nabla\frac{1}{|\mathbf{r}-\mathbf{r}'|}$, which has to be handled more carefully. Therefore, consider $\mathbf{r}$ to be very close to Γ, with projection $\mathbf{p}$ onto Γ, as demonstrated in Fig. 5.4. The signed distance of $\mathbf{r}$ to Γ is then

$$h = (\mathbf{r}-\mathbf{p})\cdot\mathbf{n}. \tag{5.23}$$

The integral is then calculated in two parts. First, integrate over a small circle with centre $\mathbf{p}$ and radius δ, denoted as B_δ, and then integrate over the remaining part $\Gamma\backslash B_\delta$. This is allowed as long as δ is chosen to be small enough and provided that the surface is sufficiently smooth. The integral over B_δ is then

$$\int_{B_\delta} \nabla\frac{1}{|\mathbf{r}-\mathbf{r}'|}\,\mathrm{d}S' = \begin{cases} -2\pi\mathbf{n}, & h\to 0+ \\ +2\pi\mathbf{n}, & h\to 0- \end{cases}. \tag{5.24}$$

It can be proven that the integral of $\nabla\frac{1}{|\mathbf{r}-\mathbf{r}'|}$ over the remaining part of the surface converges as a Cauchy principal value when $\mathbf{r}\in\Gamma$.

The result of (5.24) can now be used to compute the limiting values of (5.22b) and (5.22c). The current densities can be assumed constant throughout the small circle B_δ:

$$G(|\mathbf{r}-\mathbf{r}'|)\mathbf{X}(\mathbf{r}') \approx \frac{1}{4\pi\,|\mathbf{r}-\mathbf{r}'|}\mathbf{X}(\mathbf{r}), \tag{5.25a}$$

$$G(|\mathbf{r}-\mathbf{r}'|)\nabla'\cdot\mathbf{X}(\mathbf{r}') \approx \frac{1}{4\pi\,|\mathbf{r}-\mathbf{r}'|}\nabla\cdot\mathbf{X}(\mathbf{r}). \tag{5.25b}$$

We then obtain for (5.22b):

$$\begin{aligned}
&\lim_{h\to 0\pm}\int_\Gamma \nabla G(|\mathbf{r}-\mathbf{r}'|)\nabla'\cdot\mathbf{X}(\mathbf{r}')\,\mathrm{d}S' \\
&\quad= \left[\fint_\Gamma \nabla G(|\mathbf{r}-\mathbf{r}'|)\nabla'\cdot\mathbf{X}(\mathbf{r}')\,\mathrm{d}S'\right]_{h=0} + \lim_{h\to 0\pm}\frac{1}{4\pi}\int_{B_\delta}\nabla\frac{1}{|\mathbf{r}-\mathbf{r}'|}\nabla\cdot\mathbf{X}(\mathbf{r})\,\mathrm{d}S', \\
&\quad= \left[\fint_\Gamma \nabla G(|\mathbf{r}-\mathbf{r}'|)x(\mathbf{r}')\,\mathrm{d}S'\right]_{h=0} \mp\frac{1}{2}\nabla\cdot\mathbf{X}(\mathbf{r})\mathbf{n}.
\end{aligned} \tag{5.26a}$$

The line through the integration symbol means that the integral has to be calculated in the Cauchy principal value sense. The limit value of (5.22c) is:

$$\begin{aligned}
&\lim_{h\to 0\pm}\int_\Gamma \nabla\times G(|\mathbf{r}-\mathbf{r}'|)\mathbf{X}(\mathbf{r}')\,\mathrm{d}S' \\
&\quad= \left[\fint_\Gamma \nabla\times G(|\mathbf{r}-\mathbf{r}'|)\mathbf{X}(\mathbf{r}')\,\mathrm{d}S'\right]_{h=0} + \lim_{h\to 0\pm}\frac{1}{4\pi}\int_{B_\delta}\nabla\times\frac{1}{|\mathbf{r}-\mathbf{r}'|}\mathbf{X}(\mathbf{r})\,\mathrm{d}S', \\
&\quad= \left[\fint_\Gamma \nabla\times G(|\mathbf{r}-\mathbf{r}'|)\mathbf{X}(\mathbf{r}')\,\mathrm{d}S'\right]_{h=0} \mp\frac{1}{2}\mathbf{n}\times\mathbf{X}(\mathbf{r}).
\end{aligned} \tag{5.27}$$

The identity $\nabla \times (\varphi \mathbf{F}) = \nabla\varphi \times \mathbf{F} + \varphi \nabla \times \mathbf{F}$ was applied in the last line.

In the following, the notation

$$\mathbf{Y}^{\pm}(\mathbf{r}) = \lim_{h \to 0\pm} \mathbf{Y}(\mathbf{r}) \tag{5.28}$$

will be used.

The traces of the tangential parts of the integral representations are the most interesting for constructing boundary integral equations. Therefore, two integral operators $\mathcal{T}$ and $\mathcal{K}$ are introduced. The operator $\mathcal{T}$ is defined as

$$\begin{aligned}\mathcal{T}[\mathbf{X}](\mathbf{r}) &= \mathcal{T}_s[\mathbf{X}](\mathbf{r}) + \mathcal{T}_h[\mathbf{X}](\mathbf{r}) \\ &= -\frac{j\omega}{4\pi c}\mathbf{n} \times \int_\Gamma G(|\mathbf{r}-\mathbf{r}'|)\mathbf{X}(\mathbf{r}')\,\mathrm{d}S' \\ &\qquad + \frac{c}{4\pi j\omega}\mathbf{n} \times \int_\Gamma \nabla G(|\mathbf{r}-\mathbf{r}'|)\nabla' \cdot \mathbf{X}(\mathbf{r}')\,\mathrm{d}S',\end{aligned} \tag{5.29}$$

$\forall \mathbf{r} \in \Gamma$, and the definition of the operator $\mathcal{K}$ is

$$\mathcal{K}[\mathbf{X}](\mathbf{r}) = -\frac{1}{4\pi}\mathbf{n} \times \int_\Gamma \nabla G(|\mathbf{r}-\mathbf{r}'|) \times \mathbf{X}(\mathbf{r}')\,\mathrm{d}S', \tag{5.30}$$

$\forall \mathbf{r} \in \Gamma$. The traces of the tangential parts of the integral representations are then written as

$$\mathbf{E}^{\pm}(\mathbf{r}) \times \mathbf{n} = -\eta\mathcal{T}[\mathbf{J}](\mathbf{r}) + \left\{-\mathcal{K} \pm \frac{1}{2}\right\}[\mathbf{K}](\mathbf{r}), \tag{5.31a}$$

$$\mathbf{n} \times \mathbf{H}^{\pm}(\mathbf{r}) = \left\{-\mathcal{K} \pm \frac{1}{2}\right\}[\mathbf{J}](\mathbf{r}) + \frac{1}{\eta}\mathcal{T}[\mathbf{K}](\mathbf{r}), \tag{5.31b}$$

with $\eta = \sqrt{\mu/\epsilon}$ the wave impedance. In the special case where the currents are the equivalent currents $\mathbf{J}_{\text{eq}} = \mathbf{n} \times \mathbf{H}$ and $\mathbf{K}_{\text{eq}} = \mathbf{E} \times \mathbf{n}$ (see Section 1.3), this becomes

$$\begin{pmatrix} \mathbf{E}^{\pm}(\mathbf{r}) \times \mathbf{n} \\ \mathbf{n} \times \mathbf{H}^{\pm}(\mathbf{r}) \end{pmatrix} = \begin{pmatrix} -\mathcal{K} \pm \frac{1}{2}\mathcal{I} & -\eta\mathcal{T} \\ \frac{1}{\eta}\mathcal{T} & -\mathcal{K} \pm \frac{1}{2}\mathcal{I} \end{pmatrix} \cdot \begin{pmatrix} \mathbf{E}(\mathbf{r}) \times \mathbf{n} \\ \mathbf{n} \times \mathbf{H}(\mathbf{r}) \end{pmatrix} + \begin{pmatrix} \mathbf{E}^i(\mathbf{r}) \times \mathbf{n} \\ \mathbf{n} \times \mathbf{H}^i(\mathbf{r}) \end{pmatrix}, \tag{5.32}$$

with $\mathcal{I}$ the identity operator and where $\mathbf{E}^i$ and $\mathbf{H}^i$ are the fields radiated by other sources. This is the Stratton-Chu representation theorem, describing a relationship between the traces of the fields.

The representation of (5.32) can, in analogy to the FE formulation, also be written as a function of the tangential trace of the electric field on Γ, $\mathbf{E}^t = \mathbf{n} \times (\mathbf{E} \times \mathbf{n})$, and the equivalent electric current $\mathbf{J} = \mathbf{J}_{\text{eq}}$ (the $\mathbf{r}$ dependency will be omitted for the

ease of reading). For the sourceless system in a domain where a normal $\mathbf{n}$ points into, we then obtain

$$\begin{pmatrix} -\mathbf{n}\times\mathbf{E}^t \\ \mathbf{J} \end{pmatrix} = \mathcal{P}\begin{pmatrix} -\mathbf{n}\times\mathbf{E}^t \\ \mathbf{J} \end{pmatrix}, \tag{5.33}$$

where the block-Calderón operator $\mathcal{P}$ is defined as

$$\mathcal{P} \equiv \begin{pmatrix} -\mathcal{K}+\frac{1}{2}\mathcal{I} & -\eta\mathcal{T} \\ \frac{1}{\eta}\mathcal{T} & -\mathcal{K}+\frac{1}{2}\mathcal{I} \end{pmatrix}. \tag{5.34}$$

If the normal $\mathbf{n}$ points outside the domain, it follows from (5.32) that the complementary Calderón operator $\tilde{\mathcal{P}} = \mathcal{I} - \mathcal{P}$ needs to be used. In a system with sources, this becomes

$$\left(\mathcal{I}-\tilde{\mathcal{P}}\right)\begin{pmatrix} -\mathbf{n}\times\mathbf{E} \\ \mathbf{J} \end{pmatrix} = \begin{pmatrix} -\mathbf{n}\times\mathbf{E}^i \\ \mathbf{J}^i \end{pmatrix}, \tag{5.35a}$$

$$\begin{pmatrix} \mathcal{K}'+\frac{1}{2}\mathcal{I} & \eta\mathcal{U} \\ -\frac{1}{\eta}\mathcal{N}\mathcal{U}\mathcal{N} & -\mathcal{K}+\frac{1}{2}\mathcal{I} \end{pmatrix}\begin{pmatrix} \mathbf{E}^t \\ \mathbf{J} \end{pmatrix} = \begin{pmatrix} \mathbf{E}^{t,i} \\ \mathbf{J}^i \end{pmatrix}. \tag{5.35b}$$

We have that $\mathcal{N} = \mathbf{n}\times$, with $\mathcal{N}' = -\mathcal{N}$ and $\mathcal{N}^2 = -\mathcal{I}$. The complex symmetric operator $\mathcal{U} = \mathcal{U}'$ is related to (5.29) and (5.34) by $\mathcal{T} = \mathcal{N}\mathcal{U}$ and $\mathcal{N}\mathcal{K}\mathcal{N} = \mathcal{K}'$ [13]. The equations of (5.35b) are the well-known electric field integral equation (EFIE) and magnetic field integral equation (MFIE) and will be used in Chapter 6 to couple the BIE method with the FE method.

5.3.4 The Calderón identities

The Calderón identities are obtained from the Calderón operator $\mathcal{P}$ and play an important role in determining the stability of hybrid FE-BIE formulations in Chapter 7. Therefore, they are given here.

The sourceless Calderón operator (5.33) is written as

$$\frac{1}{2}\begin{pmatrix} \mathbf{E}^t \\ \eta\mathbf{J} \end{pmatrix} = \mathcal{H}\begin{pmatrix} \mathbf{E}^t \\ \eta\mathbf{J} \end{pmatrix}. \tag{5.36}$$

Applying the Hamiltonian operator $\mathcal{H}$ [13] again on (5.36) leads to

$$\frac{1}{2}\mathcal{H}\begin{pmatrix}\mathbf{E}\\ \eta\mathbf{J}\end{pmatrix} = \mathcal{H}^2\begin{pmatrix}\mathbf{E}\\ \eta\mathbf{J}\end{pmatrix}, \tag{5.37}$$

$$\frac{1}{4}\begin{pmatrix}\mathbf{E}\\ \eta\mathbf{J}\end{pmatrix} = \mathcal{C}\begin{pmatrix}\mathbf{E}\\ \eta\mathbf{J}\end{pmatrix}, \tag{5.38}$$

with

$$\mathcal{C} = \begin{pmatrix} \mathcal{K}'^2 - \mathcal{U}\mathcal{N}\mathcal{U}\mathcal{N} & \mathcal{K}'\mathcal{U} - \mathcal{U}\mathcal{K} \\ -\mathcal{N}\mathcal{U}\mathcal{N}\mathcal{K}' + \mathcal{K}\mathcal{N}\mathcal{U}\mathcal{N} & -\mathcal{N}\mathcal{U}\mathcal{N}\mathcal{U} + \mathcal{K}^2 \end{pmatrix}. \tag{5.39}$$

Since (5.38) has to be valid for all frequencies, four equations are found, the so-called Calderón identities.

5.3.5 The method of moments

The method of moments is a numerical technique that can be applied to solve the EFIE and the MFIE (5.35b). The foundation of the method, as we know it, was laid by Harrington [14]. The principle is as follows: consider a linear operator $\mathcal{L}$ connecting a field $\mathbf{f}(\mathbf{r})$ with a source $\mathbf{g}(\mathbf{r})$

$$\mathcal{L}(\mathbf{f}(\mathbf{r})) = \mathbf{g}(\mathbf{r}). \tag{5.40}$$

The field is then projected onto a finite n-dimensional subspace with basis functions $\mathbf{b}_i(\mathbf{r})$

$$\mathbf{f}(\mathbf{r}) \approx \sum_{i=1}^{n} a_i \mathbf{b}_i(\mathbf{r}), \tag{5.41}$$

where a_i is a set of unknown scalar coefficients. In order to determine the n unknowns, equation (5.40) is projected onto an m-dimensional basis, spanned by the weighting functions $\mathbf{v}_j$

$$\langle \mathbf{v}_j, \mathcal{L}(\mathbf{f}(\mathbf{r})) \rangle = \langle \mathbf{v}_j, \mathbf{g}(\mathbf{r}) \rangle. \tag{5.42}$$

In this thesis, the Galerkin method is applied, meaning that the weighting functions and basis functions are equal. This leads to a dense system of n equations for solving n unknowns.

5.3.6 Discretisation

The basis functions that are used to discretise the equivalent currents on the material boundaries are the div-conforming Rao-Wilton-Glisson (RWG) basis functions [15]. Remark that in contrast to the FE method, the BIE basis functions only need

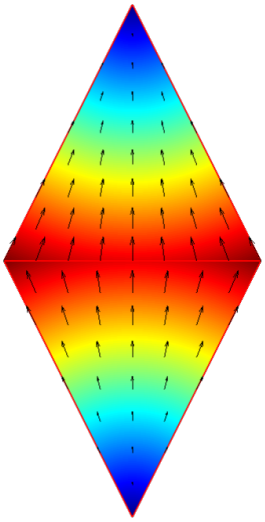

Figure 5.5: An RWG basis function.

to span a 2D space. For a point in a triangular cell, an RWG is evaluated by means of

$$\mathbf{f}(\mathbf{r}) = \pm\frac{l}{2A}(\mathbf{r}-\mathbf{p}), \tag{5.43}$$

with l the length of an edge, A the area of the triangle and $\mathbf{p}$ the vertex opposite to the edge.

A second type of div-conforming basis functions are the Buffa-Christiansen (BC) basis functions [16]. These basis functions are constructed on the barycentric mesh (also named as the refined mesh) and each RWG on the original mesh corresponds to one BC basis function, as demonstrated in Fig. 5.6. The BC basis function is a linear combination of RWG basis functions, associated with the refined mesh that have a vertex in common with the RWG on the original mesh.

An important property is that the curl-conforming $\mathbf{n}\times$ BC basis functions are not perpendicular to the div-conforming RWG basis functions. This means that the Gramian matrix $\langle \mathbf{n}\times \text{BC}, \text{RWG}\rangle$ is well-conditioned, whereas $\langle \mathbf{n}\times \text{RWG}, \text{RWG}\rangle$ is a singular matrix.

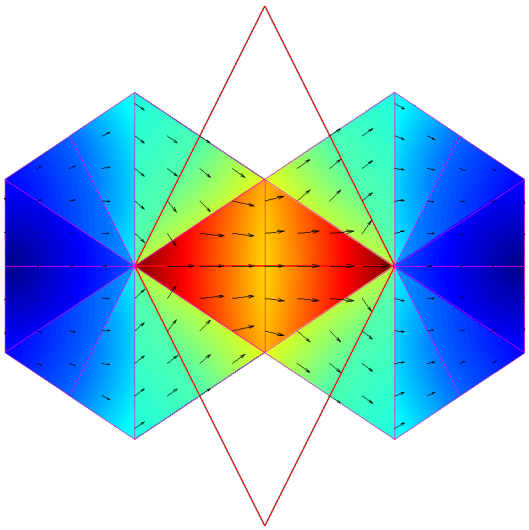

Figure 5.6: A BC basis function.

References

[1] A. Peterson, *Mapped Vector Basis Functions for Electromagnetic Integral Equations*. Morgan & Claypool, 2005.

[2] V. Girault and R. Pierre-Arnaud, *Finite Element Methods for Navier-Stokes Equations*. New York: Springer, 1986.

[3] J. L. Volakis, K. Sertel, and B. C. Usner, *Frequency Domain Hybrid Finite Element Methods for Electromagnetics*, C. A. Balanis, Ed. Morgan & Claypool, 2006.

[4] P. Silvester and R. Ferrari, *Finite Elements for Electrical Engineers*. Cambridge, UK: Cambridge University Press, 1990.

[5] J. Jin, *The Finite Element Method in Electromagnetics*. New York: John Wiley & Sons, 1993.

[6] P. Monk, *Finite Element Methods for Maxwell's Equations*, ser. Numerical Mathematics and Scientific Computing. Oxford University Press Inc., 2003.

[7] Y. Zhu and A. C. Cangellaris, *Multigrid Finite Element Methods for Electromagnetic Field Modeling*, ser. IEEE Press Series on Electromagnetic Wave Theory. Hoboken, New Jersey: John Wiley and Sons, Inc., 2006.

[8] B. Engquist and A. Majda, "Absorbing boundary conditions for the numerical simulations of waves", *Mathematics of Computation*, vol. 31, no. 139, pp. 629–651, Jul. 1977.

[9] J.-C. Nédélec, "Mixed finite elements in R3", *Numerische Mathematik*, vol. 35, pp. 315–341, 1980.

[10] R. Harrington, *Time-Harmonic Electromagnetic Fields*. New York, US: McGraw-Hill, 1961.

[11] J. G. Van Bladel, *Electromagnetic Fields*, 2nd, D. G. Dudley, Ed. John Wiley and Sons, Inc., 2007.

[12] W. C. Chew, M. S. Tong, and B. Hu, *Integral Equation Methods for Electromagnetic and Elastic Waves*, C. A. Balanis, Ed. Morgan & Claypool, 2008.

[13] L. Knockaert and D. De Zutter, "On the complex symmetry of the Poincaré-Steklov operator", *Progress In Electromagnetics Research B*, vol. 7, pp. 145–157, 2008.

[14] R. Harrington, *Field Computation by Moment Methods*, D. G. Dudley, Ed. Oxford: Oxford University Press, 1968.

[15] S. M. Rao, D. R. Wilton, and A. W. Glisson, "Electromagnetic scattering by surfaces of arbitrary shapes", *IEEE Trans. Antennas Propag.*, vol. 30, no. 3, pp. 409–418, May 1982.

[16] A. Buffa and S. H. Christiansen, “A dual finite element complex on the barycentric refinement”, *Mathematics of Computation*, vol. 76, no. 260, pp. 1743–1769, May 2007.

6

A Non-Conformal 3D Hybrid Finite Element - Boundary Integral Equation Method

★ ★ ★

A symmetric hybrid FE-BIE system is formulated with two types of boundary conditions. The first type imposes weak tangential continuity of the field components, whereas the second type applies Robin transmission conditions. In this formulation, the FE and BIE simulation domains are fully decoupled, meaning that their solutions are discretised on different meshes and/or with a different type/order of basis functions. The goal of this coupling is, as for all kinds of hybrid methods, to minimise the computational requirements by employing each method where it is most efficient.

6.1 Introduction

The FE method offers the ability to model complex inhomogeneous materials and anisotropic structures, but suffers from domain truncation and approximate absorbing boundary conditions. Its effectiveness can be improved by combining the technique with the BIE method. This approach allows to extend the simulation domain to the full open space by enforcing the Silver-Müller radiation conditions in the kernel functions of the integral equations. Also multiple distant subdomains can be coupled in this way.

For this coupling, the following additional criteria are also proposed:

- The coupling between neighbouring domains must be enforced in the weak sense, resulting in decoupled discretisations. This means that the FE and BIE solutions are discretised on different meshes. This can also mean that the FE and BIE may use the same mesh, but different type/order basis functions.

- The reciprocity theorem and energy conservation must be respected at the FE-BIE interface.

A 2D decoupled formulation has previously been proposed in [1], but this approach suffers from some drawbacks. First, reciprocity is not respected in the non-symmetric system, and second, a zero lies on the diagonal of the system matrix, leading to an inherently less stable system. An improvement for bodies of revolution is found in [2], where both the EFIE and MFIE equations are used in order to form a symmetric system matrix.

In 3D, it is worth mentioning the work described in [3], where the CFIE is used to avoid interior resonances, but this leads to an non-symmetric system matrix. Hence, it becomes more difficult and computationally expensive to solve with iterative solvers. The approach described in this chapter is based on [4], where the FE and BIE domains are fully decoupled and the formulation leads to a symmetric system matrix. This enhances the modularity of the formulation and faster convergence is achieved when solving the system with iterative solvers. Two types of boundary conditions are used: the first type imposes weak tangential continuity of the field components, whereas the second type applies Robin transmission conditions.

6.2 Matrix representations

Fig. 6.1 depicts the configuration of the hybrid system. The bounded FE domain is Ω with boundary $\partial\Omega$ and outward normal $\mathbf{n}_1$. The outward normal of the unbounded BIE domain is given by $\mathbf{n}_0 = -\mathbf{n}_1$. In the FE domain, we have the electric field $\mathbf{E}_1$, with tangential trace $\mathbf{E}_1^t$ on $\partial\Omega$ and the equivalent electric current $\mathbf{J}_1$ (this last set of unknowns is introduced because of the decoupling of the FE and BIE meshes). On the BIE side, the electric field in the BIE domain is $\mathbf{E}_0^t$ and the equivalent electric current is $\mathbf{J}_0$. The relation between the tangential electric current and the equivalent magnetic current in the BIE domain is: $\mathbf{E}_0^t = \mathbf{n}_0 \times \mathbf{M}_0$.

The following equations are combined in the hybrid formulation:

1. The wave equation for the electric field, after construction of the Dirichlet-to-Neumann operator $\mathcal{Y}_1$, as calculated in (5.10)

$$\mathcal{Y}_1 \mathbf{E}_1^t - \mathbf{J}_1 = -\mathbf{J}^{\text{imp}}. \tag{6.1}$$

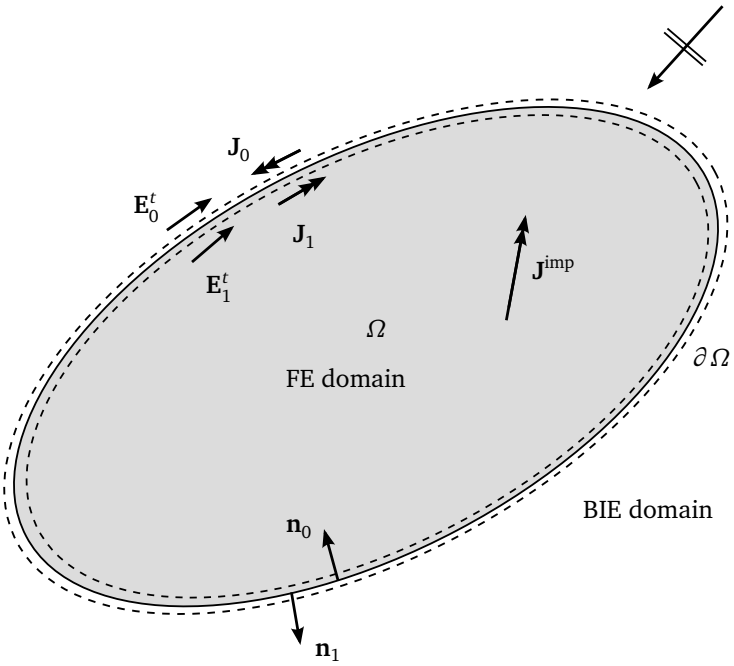

Figure 6.1: Hybrid configuration.

2. The EFIE, as obtained in (5.35b) for a domain with an outward normal

$$\left(\mathcal{K}' + \frac{1}{2}\mathcal{I}\right)\mathbf{E}_0^t + \eta_0 \mathcal{U}\mathbf{J}_0 = \mathbf{E}^{t,i}. \tag{6.2}$$

3. The MFIE, also from (5.35b), for a domain with an outward normal

$$-\frac{1}{\eta_0}\mathcal{N}\mathcal{U}\mathcal{N}\mathbf{E}_0^t + \left(-\mathcal{K} + \frac{1}{2}\mathcal{I}\right)\mathbf{J}_0 = \mathbf{J}^i. \tag{6.3}$$

6.2.1 Tangential continuity

On $\partial\Omega$, the continuity of the tangential electric field and the equivalent electric current is imposed:

$$\mathbf{E}_0^t = \mathbf{E}_1^t, \tag{6.4a}$$
$$\mathbf{J}_0 = -\mathbf{J}_1. \tag{6.4b}$$

It is clear that these boundary conditions satisfy the reciprocity theorem and the law of energy conservation, defined in Section 1.4 and Section 1.5.

The first equation combines (6.1) with (6.4b). By splitting the electric current $\mathbf{J}_1$ into two and substituting the electric current $\mathbf{J}_0$ from the BIE domain, we get:

$$\mathcal{Y}_1\mathbf{E}_1^t - \frac{1}{2}\mathbf{J}_1 + \frac{1}{2}\mathbf{J}_0 = -\mathbf{J}^{\text{imp}}. \tag{6.5}$$

The second equation is constructed from (6.2) and (6.4a). Here, the FE electric field is substituted via the singular part of the EFIE.

$$\mathcal{K}'\mathbf{E}_0^t + \eta_0\mathcal{U}\mathbf{J}_0 + \frac{1}{2}\mathbf{E}_1^t = \mathbf{E}^{t,i}. \tag{6.6}$$

The third equation combines (6.3) and (6.4b). The FE electric current is substituted via the singular part of the MFIE.

$$-\frac{1}{\eta_0}\mathcal{N}\mathcal{U}\mathcal{N}\mathbf{E}_0^t - \mathcal{K}\mathbf{J}_0 - \frac{1}{2}\mathbf{J}_1 = \mathbf{J}^i. \tag{6.7}$$

The last equation explicitly enforces (6.4a):

$$\frac{1}{2}\mathbf{E}_0^t - \frac{1}{2}\mathbf{E}_1^t = 0. \tag{6.8}$$

The symmetric matrix representation is then:

$$\begin{pmatrix} \mathcal{Y}_1 & -\frac{1}{2}\mathcal{I} & 0 & \frac{1}{2}\mathcal{I} \\ -\frac{1}{2}\mathcal{I} & 0 & \frac{1}{2}\mathcal{I} & 0 \\ 0 & \frac{1}{2}\mathcal{I} & \frac{1}{\eta_0}\mathcal{N}\mathcal{U}\mathcal{N} & \mathcal{K} \\ \frac{1}{2}\mathcal{I} & 0 & \mathcal{K}' & \eta_0\mathcal{U} \end{pmatrix} \begin{pmatrix} \mathbf{E}_1^t \\ \mathbf{J}_1 \\ \mathbf{E}_0^t \\ \mathbf{J}_0 \end{pmatrix} = \begin{pmatrix} -\mathbf{J}^{\text{imp}} \\ 0 \\ -\mathbf{J}^i \\ \mathbf{E}^{t,i} \end{pmatrix}. \tag{6.9}$$

6.2.2 Robin transmission conditions

The Robin transmission conditions find their origin in the Sommerfeld radiation condition, which states that the energy radiated from sources cannot scatter back from infinity.

$$\lim_{r\to\infty} r\big(\mathbf{u}_r \times (\nabla \times \mathbf{E}) - jk\mathbf{E}\big) = \mathbf{0}. \tag{6.10}$$

At the boundary $\partial\Omega$, a similar residue can be calculated.

$$\psi = -\big(\mathbf{n} \times (\nabla \times \mathbf{E}) - jk\mathbf{E}\big) = \mathbf{E}^t + \eta_0\mathbf{J}. \tag{6.11}$$

This residue is transferred to the other domain.

$$\mathbf{E}_0^t + \eta_0\mathbf{J}_0 = \mathbf{E}_1^t - \eta_0\mathbf{J}_1, \tag{6.12a}$$

$$\mathbf{E}_1^t + \eta_0\mathbf{J}_1 = \mathbf{E}_0^t - \eta_0\mathbf{J}_0. \tag{6.12b}$$

In order to make it more general, a constant factor α can be used.

$$\mathbf{E}_0^t + \alpha\mathbf{J}_0 = \mathbf{E}_1^t - \alpha\mathbf{J}_1, \tag{6.13a}$$
$$\mathbf{E}_1^t + \alpha\mathbf{J}_1 = \mathbf{E}_0^t - \alpha\mathbf{J}_0. \tag{6.13b}$$

These boundary conditions also satisfy reciprocity and energy conservation, since by subtracting and adding the equations (6.13a) and (6.13b), we obtain the tangential continuity boundary conditions.

The first equation combines (6.1) with (6.13b):

$$\left(\mathcal{Y}_1 + \frac{1}{2\alpha}\right)\mathbf{E}_1^t - \frac{1}{2}\mathbf{J}_1 - \frac{1}{2\alpha}\mathbf{E}_0^t + \frac{1}{2}\mathbf{J}_0 = -\mathbf{J}^{\text{imp}}. \tag{6.14}$$

The second equation is constructed from (6.2) and (6.13a):

$$\mathcal{K}'\mathbf{E}_0^t + \left(\eta_0\mathcal{U} - \frac{1}{2}\alpha\right)\mathbf{J}_0 + \frac{1}{2}\mathbf{E}_1^t - \frac{1}{2}\alpha\mathbf{J}_1 = \mathbf{E}^{t,i}. \tag{6.15}$$

The third equation combines (6.3) and (6.13a):

$$-\left(\frac{1}{\eta_0}\mathcal{N}\mathcal{U}\mathcal{N} + \frac{1}{2\alpha}\right)\mathbf{E}_0^t - \mathcal{K}\mathbf{J}_0 + \frac{1}{2\alpha}\mathbf{E}_1^t - \frac{1}{2}\mathbf{J}_1 = \mathbf{J}^i. \tag{6.16}$$

The last equation explicitly enforces (6.13b):

$$\frac{1}{2}\mathbf{E}_0^t - \frac{1}{2}\alpha\mathbf{J}_0 - \frac{1}{2}\mathbf{E}_1^t - \frac{1}{2}\alpha\mathbf{J}_1 = 0. \tag{6.17}$$

The symmetric matrix representation is then:

$$\begin{pmatrix} \mathcal{Y}_1 + \frac{1}{2\alpha}\mathcal{I} & -\frac{1}{2}\mathcal{I} & -\frac{1}{2\alpha}\mathcal{I} & \frac{1}{2}\mathcal{I} \\ -\frac{1}{2}\mathcal{I} & -\frac{1}{2}\alpha\mathcal{I} & \frac{1}{2}\mathcal{I} & -\frac{1}{2}\alpha\mathcal{I} \\ -\frac{1}{2\alpha}\mathcal{I} & \frac{1}{2}\mathcal{I} & \frac{1}{\eta_0}\mathcal{N}\mathcal{U}\mathcal{N} + \frac{1}{2\alpha}\mathcal{I} & \mathcal{K} \\ \frac{1}{2}\mathcal{I} & -\frac{1}{2}\alpha\mathcal{I} & \mathcal{K}' & \eta_0\mathcal{U} - \frac{1}{2}\alpha\mathcal{I} \end{pmatrix} \begin{pmatrix} \mathbf{E}_1^t \\ \mathbf{J}_1 \\ \mathbf{E}_0^t \\ \mathbf{J}_0 \end{pmatrix} = \begin{pmatrix} -\mathbf{J}^{\text{imp}} \\ 0 \\ -\mathbf{J}^i \\ \mathbf{E}^{t,i} \end{pmatrix}. \tag{6.18}$$

6.2.3 Multiple domains

Multiple FE domains

The matrix representation for multiple FE domains is a simple extension of the representation for one FE domain, since we do not allow the FE domains to couple with each other. Consider the following simple form of the system matrix for one FE and one BIE domain:

$$A = \begin{pmatrix} A_{\text{FE}} & C \\ C^T & A_{\text{BIE}} \end{pmatrix}. \tag{6.19}$$

The extension to multiple FE domains then becomes:

$$A = \begin{pmatrix} A_{\text{FE},1} & 0 & 0 & 0 & C_1 \\ 0 & A_{\text{FE},2} & 0 & 0 & C_2 \\ 0 & 0 & \ddots & 0 & \vdots \\ 0 & 0 & 0 & A_{\text{FE},n} & C_n \\ C_1^T & C_2^T & \cdots & C_n^T & A_{\text{BIE}} \end{pmatrix}. \tag{6.20}$$

Multiple BIE domains

If a system contains multiple BIE domains, it is possible to couple these also in a non-conformal formulation. The EFIE and MFIE are then calculated in each domain and are coupled using the weak tangential continuity (6.4) or the Robin (6.13) boundary conditions. We will provide the symmetric system matrix for two BIE domains with Robin transmission conditions here:

$$\begin{pmatrix} \frac{1}{\eta_1}\mathcal{N}_1\mathcal{U}_1\mathcal{N}_1 + \frac{1}{2\alpha}\mathcal{I} & \mathcal{K}_1 & -\frac{1}{2\alpha}\mathcal{I} & \frac{1}{2}\mathcal{I} \\ \mathcal{K}_1' & \eta_1\mathcal{U}_1 - \frac{1}{2}\alpha\mathcal{I} & \frac{1}{2}\mathcal{I} & -\frac{1}{2}\alpha\mathcal{I} \\ -\frac{1}{2\alpha}\mathcal{I} & \frac{1}{2}\mathcal{I} & \frac{1}{\eta_0}\mathcal{N}_0\mathcal{U}_0\mathcal{N}_0 + \frac{1}{2\alpha}\mathcal{I} & \mathcal{K}_0 \\ \frac{1}{2}\mathcal{I} & -\frac{1}{2}\alpha\mathcal{I} & \mathcal{K}_0' & \eta_0\mathcal{U}_0 - \frac{1}{2}\alpha\mathcal{I} \end{pmatrix} \begin{pmatrix} \mathbf{E}_1^t \\ \mathbf{J}_1 \\ \mathbf{E}_0^t \\ \mathbf{J}_0 \end{pmatrix} = \begin{pmatrix} -\mathbf{J}^i \\ \mathbf{E}^{t,i} \\ -\mathbf{J}^i \\ \mathbf{E}^{t,i} \end{pmatrix}. \tag{6.21}$$

The indices in the operators denote the domain in which they are calculated. Remark that the same coupling matrices are obtained as for a hybrid FE-BIE formulation.

6.3 Projections

Typical for this hybrid formulation is the occurrence of coupling matrices, which represent projections of certain basis functions onto other basis functions in order to couple the different simulation domains. These projections have to be calculated as efficiently as possible and therefore they are computed analytically

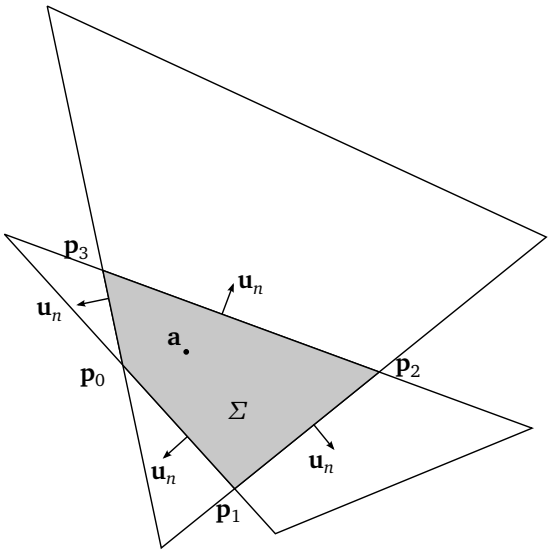

Figure 6.2: Triangle intersection.

instead of using traditional Gauss quadrature rules. In this way, no trade-off between speed and accuracy needs to be made. The calculation of these projections is explained in this section.

6.3.1 Theory

The projection of two 2D vector basis functions $\mathbf{A}(\mathbf{r})$ and $\mathbf{B}(\mathbf{r})$ is defined as the surface integral of the scalar product of the basis functions.

$$P = \int_{\Sigma} \mathbf{A}(\mathbf{r}) \cdot \mathbf{B}(\mathbf{r}) \, \mathrm{d}S = \int_{\Sigma} \Phi(\mathbf{r}) \, \mathrm{d}S. \tag{6.22}$$

The integration domain Σ is the overlap area of the support of the two basis functions and, since a triangular mesh is used, can be seen as the overlap area of two triangles. This makes Σ a polygon spanned by maximum 6 vertices. The use of traditional Gauss quadrature rules for calculating these integrals then becomes more complicated since different polygons require different Gauss rules. Alternatively, one can also subdivide the polygon into triangles, but this slows down the calculation.

It is however possible to calculate these integrals analytically, based on a technique for evaluating singular integrals over polyhedral domains. This technique, as described in [5], allows to reduce the integral of $\Phi(\mathbf{r})$ over Σ to an integral over the boundary $\partial\Sigma$, allowing the kernel of $\Phi(\mathbf{r})$ to become singular in a point $\mathbf{a} \in \Sigma$. This is demonstrated in Fig. 6.2. The overlap area of the two triangles is

Σ and a potentially singular point is $\mathbf{a}$. From [5] it follows then that, if $\Phi(\mathbf{r})$ is continuously differentiable over an open domain containing the conical domain

$$\Sigma(\mathbf{a}) = \{t\mathbf{r} + (1-t)\mathbf{a} : \ 0 < t \leq 1, \ \mathbf{r} \in \Sigma\}, \tag{6.23}$$

and provided that

$$\lim_{t \to 0} \ t^2 \Phi(t\mathbf{r} + (1-t)\mathbf{a}) = 0, \tag{6.24}$$

the following result is valid:

$$P = \int_{\partial \Sigma} (\mathbf{r} - \mathbf{a}) \cdot \mathbf{u}_n \, \mathrm{d}l \int_0^1 t \Phi(t\mathbf{r} + (1-t)\mathbf{a}) \, \mathrm{d}t. \tag{6.25}$$

With this generalised Gauss theorem, the surface integral (6.22) is transformed into a line integral along the edges of the overlap area. Moreover, since the scalar product of two basis functions exhibits no singularities, conditions (6.23) and (6.24) are always satisfied. In the example of Fig. 6.2, this means that the projection is calculated along the lines $\mathbf{p}_i\mathbf{p}_{(i+1)\%4}$ with outward normal $\mathbf{u}_n$ using (6.25). The point $\mathbf{a}$ can be chosen arbitrarily in Σ.

6.3.2 Practical implementation

First, the inner integral of (6.25) is calculated. The point $\mathbf{a}$ can be an arbitrary point in the plane, since $\Phi(\mathbf{r})$ has no singularities.

$$f(\mathbf{r}, \mathbf{a}) = \int_0^1 t\Phi\left(t\mathbf{r} + (1-t)\mathbf{a}\right) \, \mathrm{d}t. \tag{6.26}$$

The projection integral then becomes

$$P = \int_{\partial \Sigma} (\mathbf{r} - \mathbf{a}) \cdot \mathbf{u}_n \, f(\mathbf{r}, \mathbf{a}) \, \mathrm{d}l, \tag{6.27}$$

$$= \sum_i ||\mathbf{p}_{i+1} - \mathbf{p}_i|| \, (\mathbf{p}_i - \mathbf{a}) \cdot \mathbf{u}_n \, I(\mathbf{p}_i, \mathbf{p}_{i+1}, \mathbf{a}). \tag{6.28}$$

with

$$I(\mathbf{p}, \mathbf{q}, \mathbf{a}) = \int_0^1 f\left((1-t)\mathbf{p} + t\mathbf{q}, \mathbf{a}\right) \, \mathrm{d}t. \tag{6.29}$$

This last integral $I(\mathbf{p}, \mathbf{q}, \mathbf{a})$ has to be calculated over each line $\mathbf{pq}$ with outward normal $\mathbf{u}_n$. Remark that by choosing $\mathbf{a}$ equal to a vertex of Σ, two line integrals become 0. In Appendix A, the analytical expressions of $I(\mathbf{p}, \mathbf{q}, \mathbf{a})$ for all combinations of FE and BIE basis functions can be found.

6.3.3 Improving the condition number

The electric fields components $\mathbf{E}_i^t$ are discretised using curl-conforming basis functions (denoted as $\mathbf{w}_i$) and the electric currents $\mathbf{J}_i$ by div-conforming basis functions (denoted as $\mathbf{v}_i$). The projections used in the hybrid formulation can then be subdivided into 3 categories.

Dual space testing The first category consists of projections where the test functions are in the dual space of the basis functions.

$$\int_{\partial\Omega} \mathbf{w}_i(\mathbf{r}) \cdot \mathbf{v}_j(\mathbf{r}) \, \mathrm{d}S. \tag{6.30}$$

Self testing In the second category, the test functions are equal to the basis functions.

$$\int_{\partial\Omega} \mathbf{w}_i(\mathbf{r}) \cdot \mathbf{w}_i(\mathbf{r}) \, \mathrm{d}S, \tag{6.31a}$$

$$\int_{\partial\Omega} \mathbf{v}_i(\mathbf{r}) \cdot \mathbf{v}_i(\mathbf{r}) \, \mathrm{d}S. \tag{6.31b}$$

Equal space testing In the last category, the test and basis functions belong to the same space, but they are defined on the other side of the boundary Γ.

$$\int_{\partial\Omega} \mathbf{w}_i(\mathbf{r}) \cdot \mathbf{w}_j(\mathbf{r}) \, \mathrm{d}S, \tag{6.32a}$$

$$\int_{\partial\Omega} \mathbf{v}_i(\mathbf{r}) \cdot \mathbf{v}_j(\mathbf{r}) \, \mathrm{d}S, \tag{6.32b}$$

with $i \neq j$.

In the formulation with weak tangential continuity boundary conditions, only projection matrices belonging to the dual space testing exist. A problem can then arise when the FE and BIE domains are defined on the same mesh. The coupling matrices are then singular, and even worse, result in a singular FE-BIE system matrix. This problem can be tackled by using BC basis functions for the electric currents, so that the projection matrices and the system matrix become well-conditioned. However, using BC basis function to expand the electric currents in the BIE domain leads to a slow computation of the BIE interaction matrix (since it has to be computed on the refined mesh). Therefore, a trade-off is made and BCs are only used for the FE electric currents. With this approach, two of the three projection matrices become well-conditioned and the total system matrix is not singular anymore.

The expansion of the electric currents with BC basis functions is not necessary for the formulation with Robin transmission conditions, because in this formulation, we also have projection matrices belonging to the self testing category and the equal space testing category, which are well-conditioned.

6.4 Solution of the hybrid system

The solution process is discussed here for a system with one FE domain and one BIE domain, but it can easily be extended for multiple simulation domains. The symmetric system matrix is represented by the block matrix

$$A = \begin{pmatrix} A_1 & C_{12} \\ C_{21} & A_2 \end{pmatrix}, \tag{6.33}$$

where $C_{12}^T = C_{21}$.

The benefit of this hybrid FE-BIE formulation is that the FE and BIE domains are decoupled, which makes it interesting to solve the system using domain decomposition methods. These methods alternate solutions of the different domains until convergence is reached. Because only the system matrices of the local domains need to be solved, much larger problems can be tackled using this approach.

6.4.1 Stationary iterative methods

Stationary iterative methods solve a set of linear equations

$$A\mathbf{x} = \mathbf{b}, \tag{6.34}$$

in a way that the solution vector at a certain iteration can be expressed by

$$\mathbf{x}^k = B\mathbf{x}^{k-1} + \mathbf{c}, \tag{6.35}$$

where neither B or $\mathbf{c}$ depends upon the iteration count k [6].

A first method is the additive Schwarz method. Here, in every iteration step, a solution is calculated for all local domains and then the residues are updated using the coupling matrices C_{ij}. This can be schematically explained by writing the system matrix as a sum of a strictly lower triangular matrix, a diagonal matrix and a strictly upper triangular matrix:

$$A = L + D + U, \tag{6.36a}$$

$$= \begin{pmatrix} & \\ C_{21} & \end{pmatrix} + \begin{pmatrix} A_1 & \\ & A_2 \end{pmatrix} + \begin{pmatrix} & C_{12} \\ & \end{pmatrix}, \tag{6.36b}$$

One iteration is then defined by

$$\mathbf{x}^{k+1} = D^{-1}\left(\mathbf{b} - (L+U)\mathbf{x}^k\right). \tag{6.37}$$

A great advantage of this solution is that the solutions of the different domains can be calculated in parallel. This method is equivalent to a block-Jacobi method.

A second stationary method is the multiplicative Schwarz method. In contrast to the additive Schwarz method, the residue is updated after each subdomain solution. This means that in a system with n subdomains, the residue is n times updated per iteration step. Using the notation of (6.36b), one iteration is now defined by

$$\mathbf{x}^{k+1} = (L+D)^{-1}\left(\mathbf{b} - U\mathbf{x}^k\right). \tag{6.38}$$

This method is equivalent to a block Gauss-Seidel method.

6.4.2 Non-stationary iterative methods

Despite their advantage in domain decomposition methods, the stationary methods described above converge rather slowly to the correct solutions. Therefore, non-stationary methods are implemented. These methods differ from stationary methods in that the computations involve information that changes at each iteration. Typically, constants are computed by taking inner products of residuals or other vectors arising from the iterative method [6].

The non-stationary methods that were used in this formulation are the Biconjugate Gradient Stabilised (BiCGSTAB) and the Transpose Free Quasi Minimal Residual (TFQMR) algorithms with block-Jacobi preconditioners. For more information about these methods, we refer the reader to [6].

6.5 Acceleration of the program

In order to speed up the hybrid FE-BIE program, several accelerations are implemented. We make use of *Nexus*, an open source library for parallel fast multipole method (FMM) computations, designed by dr. ir. Jan Fostier [7] and further developed by dr. ir. Joris Peeters [8], together with OpenMPI[1] for parallellising the hybrid program over multiple processes. By combining this framework with a multilevel fast multipole algorithm (MLFMA) (also from [8]), the low-rank property of the BIE interaction matrix is exploited and we can further accelerate its construction. Finally, a shared-memory multiprocessing program OpenMP[2] is also employed for speeding up matrix-vector calculations and again the computation of BIE interactions.

[1] http://www.open-mpi.org/
[2] http://openmp.org/

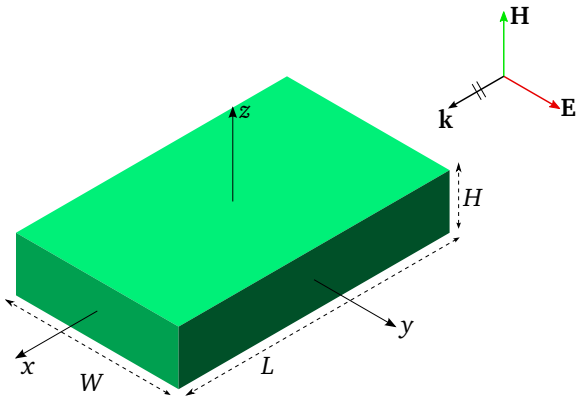

Figure 6.3: Scattering by a dielectric cuboid.

6.6 Numerical results

This section demonstrates some numerical results. Most of the examples consider plane wave scattering by a dielectric cuboid with dimensions $L \times W \times H$, as depicted in Fig. 6.3. The dimensions and the material parameters of the dielectric are mentioned in the different subsections.

6.6.1 Accuracy

The accuracy is tested by solving the scattering problem for a dielectric cube with $\{L, W, H\} = \{1, 1, 1\}$ m and $\epsilon_r = 4$. The FE calculations rely on first order basis functions. The normalised radar cross section (RCS) σ/λ^2 in the yz-plane is then calculated at 100 MHz and compared against a pure BIE reference simulation, computed by means of the Poggio-Miller-Chang-Harrington-Wu-Tsai (PMCWHT) formulation with an average edge size of 100 mm.

Influence of mesh size

First, the RCS is calculated for different mesh sizes. In this setup, the dielectric cube is treated as an FE domain and the background medium is calculated as a BIE domain. In order to obtain an accurate result, $\lambda/15$ meshing is applied. In free space, this corresponds to approximately 200 mm, whereas in the dielectric medium, this reduces to about 100 mm.

Three simulations are then performed and compared against the reference BIE simulation.

1. Identical meshes for the FE and BIE domains with an average edge size of 100 mm. This means that the FE domain has a normal mesh size of $\lambda/15$ and the BIE domain has a dense mesh size of $\lambda/30$.

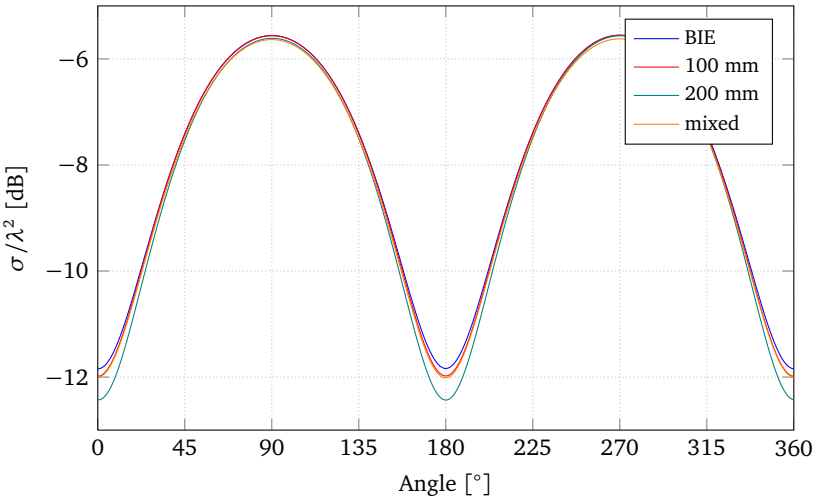

Figure 6.4: Normalised RCS of the dielectric cube in the yz-plane for different mesh sizes.

2. Again identical meshes for the FE and BIE domains, but now with an average edge size of 200 mm. This means that the FE domain has a too coarse mesh size of approximately $\lambda/7$, whereas the BIE domain has a normal mesh size of $\lambda/15$.

3. Different meshes for the FE and BIE domains. The average edge size is 100 mm for the FE domain and 200 mm for the BIE domain. Now both domains have discretisations of size $\lambda/15$.

Fig. 6.4 shows the RCS for the different simulations. It is clear that the performance of the 100 mm mesh is better than the performance of the 200 mm mesh. But more importantly, there is almost no difference in accuracy between the 100 mm mesh and the mixed mesh simulation. This means that, thanks to the non-conformal meshes, similar results can be achieved with less unknowns. The same conclusion can also be drawn when relying on second order FE basis functions.

Influence of FE bounding box size

Next, the RCS is calculated for different FE bounding box sizes. In the previous section, the FE-BIE boundary was the interface between the dielectric and the background medium. Here, we will increase the FE bounding box size, what means that now also a part of the background medium is calculated by means of the FE method.

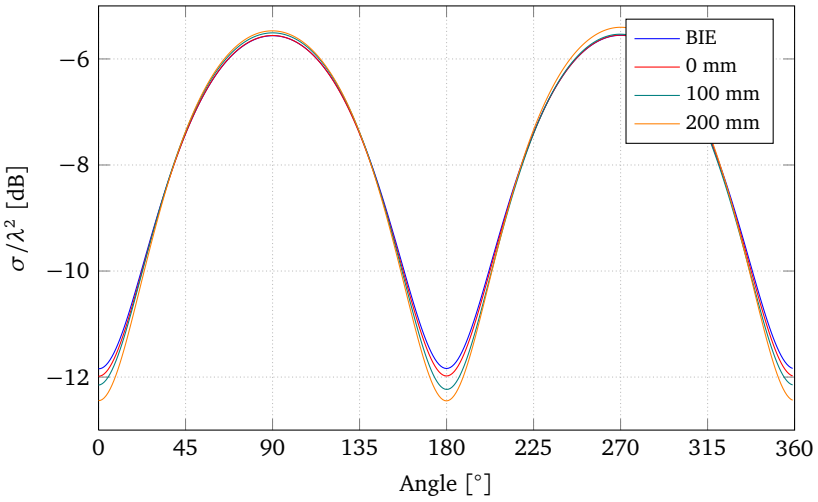

Figure 6.5: Normalised RCS of the dielectric cube in the yz-plane for different FE bounding box sizes.

The radar cross sections for the different FE bounding box sizes are shown in Fig. 6.5. All calculations are performed with a 100 mm mesh size. It is clear that the larger the FE bounding box becomes, the worse the accuracy gets. This has a double advantage for the hybrid method. It is necessary to keep the bounding box as small as possible in order to achieve better results and this leads to less unknowns in the hybrid system. When relying on second order FE basis functions, similar conclusions can be drawn, but in this case it is more important to reduce the number of unknowns.

6.6.2 Reciprocity and energy conservation

The reciprocity theorem (see Section 1.4) and the law of energy conservation (see Section 1.5) are verified by solving the scattering problem for a dielectric cuboid with $\{L,W,H\} = \{1, 0.6, 0.2\}$ m and a relative permittivity of 2. Some losses are also introduced by setting the $\tan\delta = 0.1$.

The reciprocity error is calculated by

$$\text{error} = \frac{\left|\left|\mathbf{E}_1^t \left\langle \mathbf{w}_1, \mathbf{v}_2 \right\rangle_\Gamma \mathbf{J}_2 - \mathbf{E}_2^t \left\langle \mathbf{w}_2, \mathbf{v}_1 \right\rangle_\Gamma \mathbf{J}_1\right|\right|}{\left|\left|\mathbf{E}_1^t \left\langle \mathbf{w}_1, \mathbf{v}_2 \right\rangle_\Gamma \mathbf{J}_2\right|\right|} \tag{6.39}$$

and is shown for both the formulation with tangential continuity and Robin transmission conditions in Fig. 6.6 for an increasing number of unknowns. When relying on first order FE basis functions, the reciprocity theorem is better respected by the Robin transmission conditions. However, if second order FE basis functions

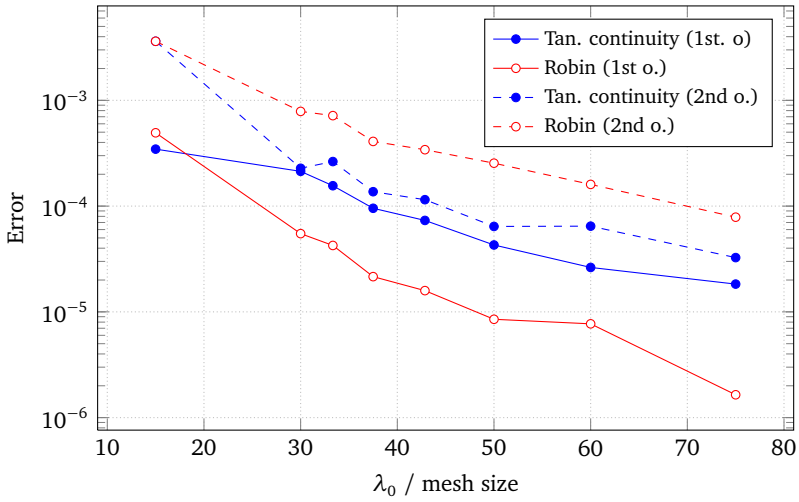

Figure 6.6: Reciprocity errors for the hybrid formulation with weak tangential continuity and the formulation imposing Robin transmission conditions. Both were simulated using first order FE basis functions (solid line) and second order FE basis functions (dashed line).

are used, the formulation imposing weak tangential continuity leads to the smallest error. Also notice that, in both formulations, the reciprocity theorem is better respected when relying on first order FE basis functions.

The energy error is computed as

$$\text{error} = \frac{\left|\left|\mathbf{E}_1^t \left\langle \mathbf{w}_1, \mathbf{v}_1 \right\rangle_\Gamma \mathbf{J}_1^* - \mathbf{E}_2^t \left\langle \mathbf{w}_2, \mathbf{v}_2 \right\rangle_\Gamma \mathbf{J}_2^*\right|\right|}{\left|\left|\mathbf{E}_1^t \left\langle \mathbf{w}_1, \mathbf{v}_1 \right\rangle_\Gamma \mathbf{J}_1^*\right|\right|}. \tag{6.40}$$

and is displayed in Fig. 6.7 for both formulations for an increasing number of unknowns. It is clear that the same conclusions can be drawn as for the reciprocity theorem. Remark that the difference between the reciprocity errors and the energy errors is approximately one order of magnitude.

6.6.3 Multiple domains

As a problem with multiple FE domains, we consider scattering of a plane wave by 9 dielectric cuboids, as demonstrated in Fig. 6.8. The cuboids have dimensions $\{L, W, H\} = \{1, 0.6, 0.2\}$ m and a relative permittivity of 4. The normalised RCS in the xy-plane is shown in Fig. 6.9 and an excellent agreement can be found when comparing the solution with a reference BIE solution applying the PMCHWT formulation.

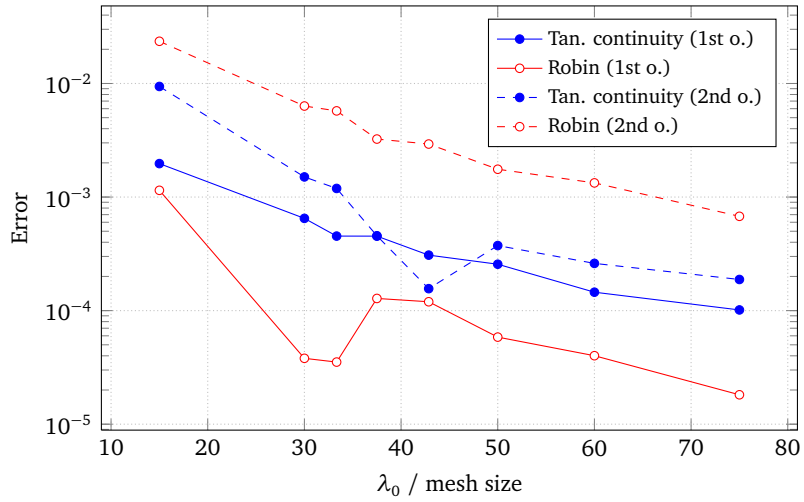

Figure 6.7: Reciprocity errors for the hybrid formulation with weak tangential continuity and the formulation imposing Robin transmission conditions. Both were simulated using first order FE basis functions (solid line) and second order FE basis functions (dashed line).

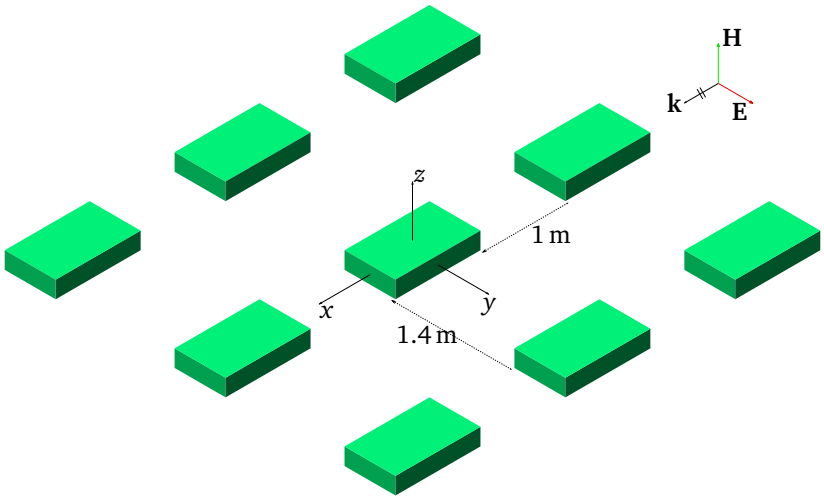

Figure 6.8: Scattering problem with multiple dielectric cuboids.

6.6.4 Patch antenna

As a real-life example, the reflection coefficient of a planar inset microstrip patch antenna is calculated. The configuration is shown in Fig. 6.10 and the substrates have a length of 6 cm and a width of 5 cm. The antenna is designed with the 2.5D

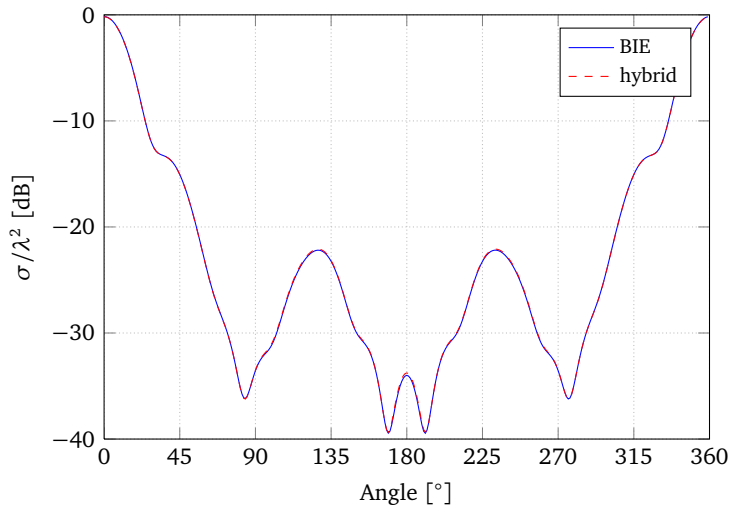

Figure 6.9: RCS of multiple dielectric cuboids in the xy-plane.

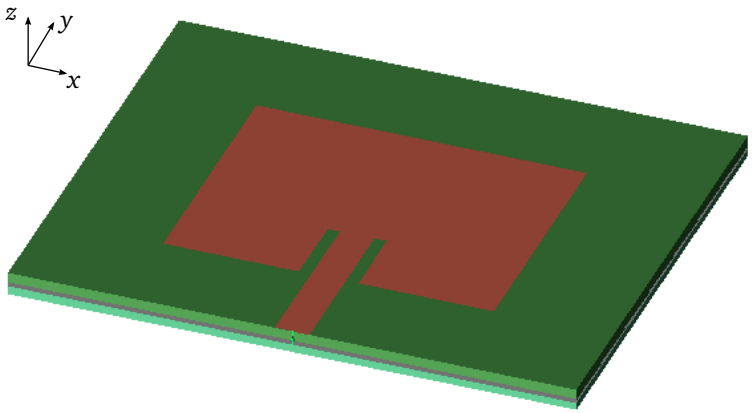

Figure 6.10: Configuration of the planar inset microstrip patch antenna.

simulation tool ADS Momentum® for operation at 3 GHz with an input impedance of 50 Ω. It is constructed on rigid substrates with relative permittivities of 3.38 (bottom substrate) and 3.66 (top substrate, Rogers® RO4350B).

Three simulation setups are now compared in terms of CPU-time, memory usage and accuracy:

Table 6.1: Data of the different patch antenna simulations setups.

Setup	FE padding	# FE unknowns	# FE boundary unknowns	# BIE unknowns
1	20 mm	370 613	7 720	-
2	20 mm	370 613	7 720	2 220
3	10 mm	336 341	1 157	534

1. A pure FE simulation with absorbing boundary conditions. In EMPro, the surface mesh size of the substrates is set to 3 mm and that of the conductors to 2 mm. The target mesh size is set to 7 mm.

2. A hybrid FE-BIE simulation with the same FE bounding box and discretisation as setup 1 and a coarse BIE mesh with an average edge size of 10 mm.

3. A hybrid FE-BIE simulation with a smaller FE bounding box as setup 1 and where the BIE mesh is identical to the boundary FE mesh. The surface mesh sizes of the substrates and conductors are equal to that of setup 1, however, no target mesh size is specified in this setup.

Their data are shown in Table 6.1. The FE padding (a term used in EMPro to set the boundary of the simulation domain) is 20 mm in each direction for setups 1 and 2, since the radiating boundaries of setup 1 should be applied approximately one quarter of a wavelength away from the source of the signal. This is, however, not necessary for a hybrid FE-BIE simulation, hence the padding is reduced to 10 mm in setup 3. All simulations are performed with second order FE basis functions and the hybrid simulations impose Robin transmission conditions, as this leads to a faster convergence in the solution phase. The solutions are calculated with an error of 1×10^{-5} by applying the TFQMR algorithm.

The CPU-time of the most time-consuming parts of the simulations are compared in Table 6.2. During the FE meshing, the FE mesh is created and the local FE interactions are calculated. It is clear that this requires less time in setup 3, since the bounding box is closer to the antenna and less FE unknowns are created. One also notices that the computation of the Schur complement, which reduces the FE unknowns to only the boundary FE unknowns, forms the bottleneck of the hybrid simulations. It even leads to a total simulation time of setup 3 that is still larger than that of setup 1.

In Table 6.3 the memory requirements of the different simulation parts are given. Again, the Schur complement computations form the bottleneck of the hybrid simulations. Remark that the peak memory usage is given by the maximum memory usage of a part, instead of the sum of the usages of all parts.

Table 6.2: CPU time of different simulation parts at 2.5 GHz.

Setup	FE meshing	Schur complement	BIE interactions	Solution
1	1 m 30 s	-	-	35 s
2	1 m 30 s	5 m 24 s	10 s	1 m 18 s
3	1 m 12 s	2 m 8 s	2 s	1 s

Table 6.3: Memory requirements of different simulation parts at 2.5 GHz.

Setup	Schur complement	BIE interactions	Solution
1	-	-	872 MB
2	5.8 GB	75 MB	1.6 GB
3	2.3 GB	4.4 MB	33 MB

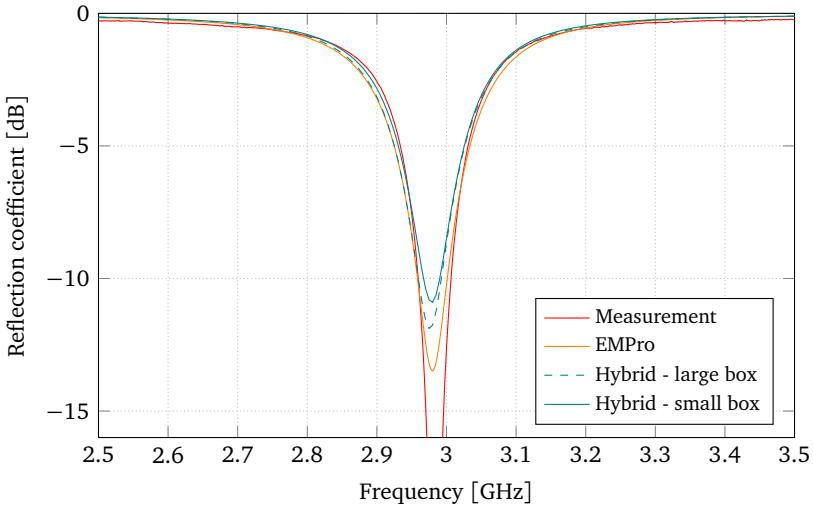

Figure 6.11: Simulated and measured reflection coefficient of the patch antenna.

The reflection coefficient is displayed in Fig. 6.11 for all simulations and for a measurement performed on an antenna prototype. It is clear that the resonance frequency is reasonably accurate for all simulations, compared to the measured resonance frequency. The only difference between the simulations is the depth of the resonance peak.

6.6.5 Patch antenna on a human body

As a final example, we demonstrate how the hybrid FE-BIE method can be employed for the simulation of a planar patch antenna on a human body. Instead of relying on a detailed body model, the simulation time is decreased by simply adding a small homogeneous block behind the antenna (with length and width 8 cm, height 2 cm and positioned 2 cm from the back of the antenna), since the size and shape of the human tissue were found to have small influence on the antenna resonance [9]. This approach was already applied in [10]. The parameters of the block are chosen to be $\epsilon_r = 50.8$ and $\sigma = 2.01\,\mathrm{S/m}$ and correspond to the human tissue mimicking fluid MSL2450, recommended by CENELEC standard EN50383 [11].

The simulation of the homogeneous block is performed by means of the BIE method and different discretisations are used for the interior and exterior surfaces. The average edge size of the exterior surface is set to 1 cm (corresponding to $\lambda/10$ at 3 GHz in free space) and the average edge size of the interior surface is chosen to be 2 mm (corresponding to $\lambda/7$ at 3 GHz in the human tissue). This leads to a total of 30 496 BIE unknowns and 1 157 FE unknowns (after calculation of the Schur complement). At 2.5 GHz, the calculation of the BIE interaction required only 3 m 17 s of CPU time and 861 MB memory, thanks to the acceleration by the MLFMA. The solution of the hybrid system was then computed after 1 m 51 s of CPU time and used 932 MB memory.

A pure FE simulation is also performed with a target mesh size of 1 cm. A system with 845 049 unknowns is then constructed in 2 m 27 s and solved in 3 m 6 s of CPU time. This required 1.8 GB memory. The reflection coefficient of both simulations is shown in Fig. 6.12. A slight difference between the resonance peaks is noticed.

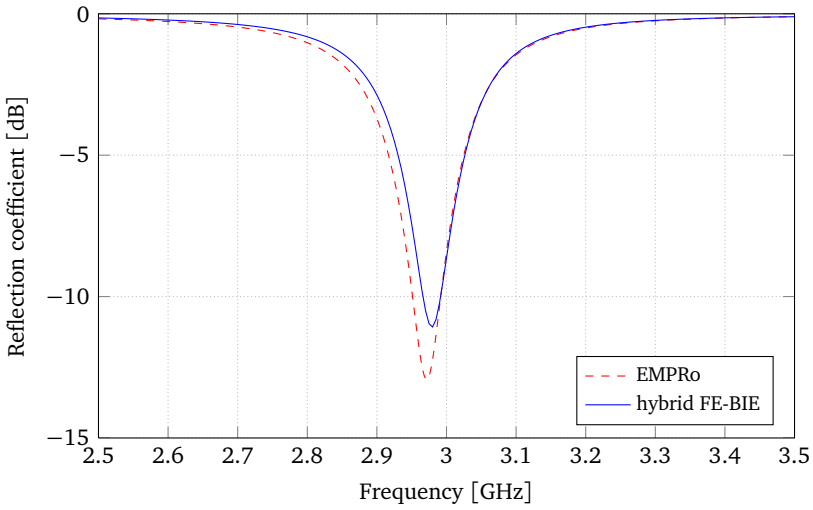

Figure 6.12: Simulated reflection coefficient of the patch antenna on a human body.

References

[1] T. Cwik, "Coupling finite element and integral equation solutions using decoupled boundary meshes", *IEEE Trans. Antennas Propag.*, vol. 40, no. 12, pp. 1496–1504, Dec. 1992.

[2] D. J. Hoppe, L. W. Epp, and J.-F. Lee, "A hybrid symmetric FEM/MOM formulation applied to scattering by inhomogeneous bodies of revolution", *IEEE Trans. Antennas Propag.*, vol. 42, no. 6, pp. 798–805, Apr. 1994.

[3] J. L. Volakis, K. Sertel, and B. C. Usner, *Frequency Domain Hybrid Finite Element Methods for Electromagnetics*, C. A. Balanis, Ed. Morgan & Claypool, 2006.

[4] K. Zhao, M. N. Vouvakis, and J.-F. Lee, "Solving electromagnetic problems using a novel symmetric FEM-BEM approach", *IEEE Trans. Magn.*, vol. 42, no. 4, pp. 583–586, Apr. 2006.

[5] L. Knockaert, "A general Gauss theorem for evaluating singular integrals over polyhedral domains", *Electromagnetics*, vol. 11, pp. 269–280, 1991.

[6] R. Barret, M. Berry, T. Chan, J. Demmel, J. Donato, J. Dongarra, V. Eijkhout, R. Pozo, C. Romine, and H. van der Vorst, *Templates for the solution of linear systems: building blocks for the iterative methods, 2nd edition*. Philadelphia, PA: SIAM, 1994.

[7] J. Fostier, "Parallel techniques for fast multipole algorithms", PhD thesis, Ghent University, 2009.

[8] J. Peeters, "Efficient simulation of 3d electromagnetic scattering problems using boundary integral equations", PhD thesis, Ghent University, 2010.

[9] A. Kiourti and K. S. Nikita, "Miniature scalp-implantable antennas for telemetry in the MICS and ISM bands: design, safety considerations and link budget analysis", *IEEE Trans. Antennas Propag.*, vol. 60, no. 8, pp. 3568–3575, Aug. 2012.

[10] S. Agneessens, P. Van Torre, E. Tanghe, G. Vermeeren, W. Joseph, and H. Rogier, "On-body wearable repeater as a data link relay for in-body wireless implants", *IEEE Antennas Wireless Propag. Lett.*, vol. 11, pp. 1714–1717, Jan. 2012.

[11] *EN50383: basic standard for the calculation and measurement of electromagnetic field strength and SAR related to human exposure from radio base stations and fixed terminal stations for wireless telecommunication systems*, CENELEC, Sep. 2012.

7

Rigorous Analysis of Internal Resonances in 3D Hybrid FE-BIE Formulations by means of the Poincaré-Steklov Operator

Freek Boeykens, Hendrik Rogier, Jan Van Hese, Jeannick Sercu and Tim Boonen

Published in IEEE Transactions on Microwave Theory and Techniques

★ ★ ★

The interest in combining the FE method with the BIE method has led to various 3D hybrid FE-BIE formulations in literature. However, some formulations suffer from breakdown frequencies at which the solution is not uniquely defined and errors are introduced due to internal resonances. In this chapter, we investigate the occurrence of spurious solutions resulting from these resonances by using the concept of the Poincaré-Steklov or Dirichlet-to-Neumann operator, which provides a relation between the tangential electric field and the electric current on the boundary of a domain. By identifying this operator in both the FE and the BIE method, several new properties of internal resonances in 3D hybrid FE-BIE formulations are easily derived. Several conformal and non-conformal formulations are studied and the theory is then applied to a scattering problem.

7.1 Introduction

We already know from Chapter 6 that the effectiveness of the FE method can be improved by combining the technique with the BIE method, which allows extending the simulation domain to the full open space by enforcing the Silver-Müller radiation conditions in the kernel functions of the integral equations. Such methods were already successfully implemented in the past in 2D (e.g. [1], [2]) and in 3D (e.g. [3], [4]).

The exact hybrid formulation appears to be very important in order to avoid so-called spurious solutions. Previous contributions demonstrated that formulations applying the EFIE or the MFIE as BIE method in combination with an FE method contain certain 'forbidden frequencies' if the background medium is lossless [3], [5]–[12]. At these frequencies, the EFIE and MFIE are not uniquely defined and the sourceless hybrid system contains non-trivial solutions that introduce errors on the result. Adding some losses to the background medium alleviates this problem, but doesn't provide much theoretical insight [13].

Some knowledge about spurious solutions is rendered by Chew in [14], [15], where he discusses internal resonances in integral equations by means of Gedanken experiments. He also relates the combined field integral equation (CFIE) to the cavity resonance problem with impedance boundary conditions to conclude that uniqueness is provided. The CFIE is also applied in time-domain FE-BIE methods, such as in [16], and in FDTD transparent boundary conditions, see [17], in order to overcome the problem of internal resonances. However, the stability of hybrid formulations such as in [4], [18], [19] was until now only investigated by means of numerical simulations, which is actually a trial-and-error method. Hence, another approach is still required.

In this chapter, we build further on the approach applied in [20], where the concept of a Poincaré-Steklov (PS) or Dirichlet-to-Neumann (DtN) operator is used to describe the relationship between the tangential electric field and the electric current on the boundary of a domain. By identifying this operator in the FE and BIE methods, different properties regarding internal resonances in hybrid formulations are easily derived. This also gives us the opportunity to investigate hybrid formulations on an operator level. Furthermore, we will not only investigate conformal formulations, where the FE and BIE share the same mesh, but also non-conformal formulations, where the FE and BIE solutions exist on different meshes and the continuity of the tangential electric fields and the electric currents is imposed in a weak sense.

The organisation of this chapter is as follows. Section 7.2 presents the theoretical background for both the FE and BIE formulations. In Section 7.3, some conformal hybrid formulations are studied and Section 7.4 discusses non-conformal formulations. The results are shown in Section 7.5 and the conclusions are drawn in Section 7.6.

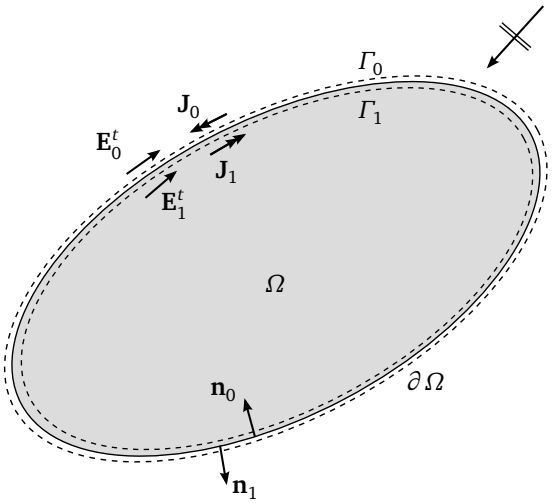

Figure 7.1: Configuration of the scattering problem.

7.2 General formulations

Consider the configuration of Fig. 7.1. A plane wave is scattered by an inhomogeneous domain Ω, bounded by $\partial\Omega$, and with relative permittivity and permeability tensors $\overline{\overline{\epsilon}}_r(\mathbf{r})$ and $\overline{\overline{\mu}}_r(\mathbf{r})$, respectively. The domain is considered to consist of reciprocal material, hence the permittivity and permeability tensors are complex symmetrical, i.e. $\overline{\overline{\epsilon}}_r(\mathbf{r}) = \overline{\overline{\epsilon}}_r^T(\mathbf{r})$ and $\overline{\overline{\mu}}_r(\mathbf{r}) = \overline{\overline{\mu}}_r^T(\mathbf{r})$. The background medium is homogeneous and isotropic, characterised by ϵ_0 and μ_0. At the boundary $\partial\Omega$, we define the surface Γ_0 as the smallest surface that encloses $\partial\Omega$ and Γ_1 as the largest surface that can be enclosed by $\partial\Omega$. Their outward normals are $\mathbf{n}_0$ and $\mathbf{n}_1$, respectively.

The tangential electric field on Γ_0 is $\mathbf{E}_0^t$ and the equivalent electric current on Γ_0 is $\mathbf{J}_0$. Accordingly, the tangential electric field on Γ_1 is $\mathbf{E}_1^t$ and the equivalent electric current on Γ_1 is $\mathbf{J}_1$. The relation between $\mathbf{E}_0^t$ and $\mathbf{J}_0$ is found using the BIE method and the connection between $\mathbf{E}_1^t$ and $\mathbf{J}_1$ is obtained by the FE method. This section describes these two formulations more in detail and identifies the complex symmetric PS operator $\mathcal{Y} = \mathcal{Y}'$ that maps the tangential electric field on the equivalent electric current: $\mathcal{Y}\mathbf{E}^t = \mathbf{J}$ [21]. It is important to note that the transpose operator $\mathcal{Y}'$ is defined with respect to the bilinear inner product $\langle \mathbf{X}|\mathbf{Y}\rangle = \int_{\partial\Omega} \mathbf{X}\cdot\mathbf{Y}\,\mathrm{d}S$ [22]. The frequencies for which $\mathcal{Y}\mathbf{E}^t = 0$ are known as the Neumann eigenfrequencies and the frequencies for which $\mathcal{Y}^{-1}\mathbf{J} = 0$ are the Dirichlet eigenfrequencies of the domain Ω.

7.2.1 The finite element method

In the inhomogeneous domain Ω, we apply the FE method as described in Section 5.2. After calculation of the Schur complement, we obtain

$$\mathcal{S}\mathbf{E}_1^t = jk_0\eta_0\mathbf{J}_1, \tag{7.1}$$

with $\eta_0 = \sqrt{\mu_0/\epsilon_0}$. Note that at some frequencies the Schur complement $\mathcal{S}$ can become singular, meaning that its inverse $\mathcal{S}^{-1}$ is undefined. Therefore, at these frequencies, we implicitly extend Γ_1 with some interior edges, such that $\mathcal{S}^{-1}$ always exists. This is the equivalent of leaving some unknowns uneliminated while forming the Schur complement.

It is easily observed that $\mathcal{S}$ is a scaled version of the complex symmetric PS operator $\mathcal{Y}_1$, since it already provides a direct relationship between $\mathbf{E}_1^t$ and $\mathbf{J}_1$. The reduced FE system can thus be written as

$$\mathcal{Y}_1\mathbf{E}_1^t = \mathbf{J}_1. \tag{7.2}$$

In the rest of this chapter, we will refer to (7.2) as the Electric Field Formulation (EFF), as in [20].

Remark that, in the case of *lossless* reciprocal media, $\overline{\overline{\epsilon}}_r$ and $\overline{\overline{\mu}}_r$ are *real* symmetric tensors. For these materials, the left hand side of (5.3) becomes a real symmetric matrix in a Galerkin weighting scheme (assuming the basis functions are real-valued). $\mathcal{S}$ is then a real symmetric matrix and $\mathcal{Y}_1$ becomes a purely imaginary operator that can be written as $\mathcal{Y}_1 = j\mathcal{X}_1$, with $\mathcal{X}_1$ a real symmetric operator: $\mathcal{X}_1 = \mathcal{X}_1'$.

7.2.2 Boundary integral equations

The fields in the homogeneous background medium are related to $\mathbf{E}_0^t$ and $\mathbf{J}_0$ by integral equations with the Green's function $G(|\mathbf{r}-\mathbf{r}'|) = e^{-jk_0|\mathbf{r}-\mathbf{r}'|}/\left(4\pi\,|\mathbf{r}-\mathbf{r}'|\right)$ as integral kernel. As can be seen from the configuration of Fig. 7.1, we solve for the tangential electric field $\mathbf{E}_0^t$ and the equivalent electric current $\mathbf{J}_0$ in the exterior domain. Hence, we can employ the EFIE and the MFIE from (5.35b), which are repeated here for the ease of reading

$$\begin{pmatrix} \mathcal{K}' + \frac{1}{2}\mathcal{I} & \eta\mathcal{U} \\ -\frac{1}{\eta}\mathcal{N}\mathcal{U}\mathcal{N} & -\mathcal{K} + \frac{1}{2}\mathcal{I} \end{pmatrix} \begin{pmatrix} \mathbf{E}^t \\ \mathbf{J} \end{pmatrix} = \begin{pmatrix} \mathbf{E}^{t,i} \\ \mathbf{J}^i \end{pmatrix}. \tag{7.3}$$

The PS operator $\mathcal{Y}_0$, which relates $\mathbf{E}_0^t$ and $\mathbf{J}_0$ in the *interior* domain, can now be identified in the sourceless Stratton-Chu representation (5.33). Remark that the domain is supposed to be filled with background material (ϵ_0, μ_0), since $G_0(\mathbf{r}, \mathbf{r}')$

is used as kernel in the integral equations. We obtain

$$\frac{1}{2}\begin{pmatrix}\mathbf{E}_0^t\\ \eta_0\mathbf{J}_0\end{pmatrix}=\begin{pmatrix}\mathcal{K}' & \mathcal{U}\\ -\mathcal{N}\mathcal{U}\mathcal{N} & -\mathcal{K}\end{pmatrix}\begin{pmatrix}\mathbf{E}_0^t\\ \eta_0\mathbf{J}_0\end{pmatrix}, \tag{7.4}$$

and with $\mathcal{Y}_0\mathbf{E}_0^t=\mathbf{J}_0$, the following properties are found:

$$\left(-\mathcal{K}'+\frac{1}{2}\mathcal{I}\right)\mathcal{Y}_0^{-1}=\eta_0\mathcal{U}, \tag{7.5a}$$

$$\left(\mathcal{K}+\frac{1}{2}\mathcal{I}\right)\mathcal{Y}_0=-\frac{1}{\eta_0}\mathcal{N}\mathcal{U}\mathcal{N}. \tag{7.5b}$$

Similarly, the complementary PS operator $\tilde{\mathcal{Y}}_0$, which relates $\mathbf{E}_0^t$ and $\mathbf{J}_0$ in the *exterior* domain, can be identified in the sourceless EFIE and MFIE (7.3):

$$\frac{1}{2}\begin{pmatrix}\mathbf{E}_0^t\\ \eta_0\mathbf{J}_0\end{pmatrix}=\begin{pmatrix}-\mathcal{K}' & -\mathcal{U}\\ \mathcal{N}\mathcal{U}\mathcal{N} & \mathcal{K}\end{pmatrix}\begin{pmatrix}\mathbf{E}_0^t\\ \eta_0\mathbf{J}_0\end{pmatrix}, \tag{7.6}$$

and with $\tilde{\mathcal{Y}}_0\mathbf{E}_0^t=\mathbf{J}_0$, we obtain

$$\mathcal{K}'+\frac{1}{2}\mathcal{I}=-\eta_0\mathcal{U}\tilde{\mathcal{Y}}_0, \tag{7.7a}$$

$$-\mathcal{K}+\frac{1}{2}\mathcal{I}=\frac{1}{\eta_0}\mathcal{N}\mathcal{U}\mathcal{N}\tilde{\mathcal{Y}}_0^{-1}. \tag{7.7b}$$

More details about $\mathcal{Y}_0$ and $\tilde{\mathcal{Y}}_0$ can be found in [21].

The uniqueness of the EFIE and the MFIE solutions is easily established after identification of the PS operator $\tilde{\mathcal{Y}}_0$ in (7.3). For the sourceless EFIE we find with (7.7a):

$$\eta_0\mathcal{U}\left(\tilde{\mathcal{Y}}_0\mathbf{E}_0^t-\mathbf{J}_0\right)=0, \tag{7.8}$$

which indicates that spurious solutions can exist when $\mathcal{U}$ becomes singular. From (7.5a), it is clear that this occurs at the Dirichlet eigenfrequencies of the interior structure filled with background material. Hence, at these frequencies, a non-zero spurious electric current $\mathbf{J}_{\text{sp}}$ can be found. Remark that $\mathbf{J}_{\text{sp}}$ does not radiate, since it is a resonant current on the PEC cavity formed by Ω. It will only generate a non-zero field *inside* the cavity. However, it will induce a radiating spurious tangential electric field $\mathbf{E}_{\text{sp}}^t=\tilde{\mathcal{Y}}_0^{-1}\mathbf{J}_{\text{sp}}$.

For the sourceless MFIE, we obtain using (7.7b):

$$\frac{1}{\eta_0}\mathcal{N}\mathcal{U}\mathcal{N}\left(\mathbf{E}_0^t-\tilde{\mathcal{Y}}_0^{-1}\mathbf{J}_0\right)=0, \tag{7.9}$$

which shows that now spurious solutions can exist when $\mathcal{NUN}$ becomes singular. From (7.5b), we find that this occurs at the Neumann eigenfrequencies of the interior structure filled with background material. Hence, at these frequencies, a non-zero spurious tangential electric field $\mathbf{E}^t_{\text{sp}}$ can be found. This is a resonant tangential electric field on the PMC cavity formed by Ω, which will only generate a non-zero field *inside* the cavity. However, it will induce a radiating spurious electric current $\mathbf{J}_{\text{sp}} = \tilde{\mathcal{Y}}_0 \mathbf{E}^t_{\text{sp}}$.

It is important to note that the spurious solutions of (7.8) and (7.9) do *not* coincide [23]. Therefore, no spurious solutions can exist if both equations are satisfied.

7.2.3 Physical resonances

When solving the sourceless problem of Fig. 7.1, the Maxwell equations lead to the following expressions in the exterior and interior domain:

$$\begin{cases} \tilde{\mathcal{Y}}_0 \mathbf{E}^t_0 - \mathbf{J}_0 = 0, \\ \mathcal{Y}_1 \mathbf{E}^t_1 - \mathbf{J}_1 = 0. \end{cases} \tag{7.10}$$

In the case of conformal meshes, we have that $\mathbf{E}^t_0 = \mathbf{E}^t_1$ and $\mathbf{J}_0 = -\mathbf{J}_1$. After substituting this in (7.10) and pre-multiplying both equations with $\tilde{\mathcal{Y}}_0^{-1}$, we find

$$\left(\mathcal{I} + \tilde{\mathcal{Y}}_0^{-1} \mathcal{Y}_1\right) \mathbf{E}^t_0 = 0. \tag{7.11}$$

This leads to $\mathbf{E}^t_0 = 0$, unless $\left(\mathcal{I} + \tilde{\mathcal{Y}}_0^{-1} \mathcal{Y}_1\right)$ becomes singular. In this case, we find a physical resonance tangential electric field for the configuration.

A similar expression for the electric current can be found, starting from

$$\begin{cases} \mathbf{E}^t_0 - \tilde{\mathcal{Y}}_0^{-1} \mathbf{J}_0 = 0, \\ \mathbf{E}^t_1 - \mathcal{Y}_1^{-1} \mathbf{J}_1 = 0. \end{cases} \tag{7.12}$$

After substitution of $\mathbf{E}^t_1$ by $\mathbf{E}^t_0$ and $\mathbf{J}_1$ by $-\mathbf{J}_1$, and after pre-multiplication of (7.12) with $\tilde{\mathcal{Y}}_0$, we obtain

$$\left(\tilde{\mathcal{Y}}_0 \mathcal{Y}_1^{-1} + \mathcal{I}\right) \mathbf{J}_0 = 0. \tag{7.13}$$

This leads to $\mathbf{J}_0 = 0$, unless $\left(\tilde{\mathcal{Y}}_0 \mathcal{Y}_1^{-1} + \mathcal{I}\right)$ becomes singular. In this case, we find a physical resonance electric current for the configuration.

7.3 Conformal hybrid FE-BIE formulations

A first group of hybrid formulations consists of conformal formulations. In these systems, both the FE and BIE method are applied on the same mesh and the

tangential electric fields and equivalent electric currents are coupled via strong (pointwise) continuity relations

$$\mathbf{E}_0^t = \mathbf{E}_1^t, \tag{7.14a}$$
$$\mathbf{J}_0 = -\mathbf{J}_1. \tag{7.14b}$$

The solution of these systems is, however, not always uniquely defined and the frequencies for which internal resonances occur can be predicted by identifying the PS operator in the different formulations.

7.3.1 EFF and EFIE

The classic approach to construct a hybrid FE-BIE formulation is to combine the EFF and the EFIE [3], [8]. Making use of (7.2) and the first equation of (7.3), the following system is obtained:

$$\begin{pmatrix} \mathcal{Y}_1 & \mathcal{I} \\ \mathcal{K}' + \frac{1}{2}\mathcal{I} & \eta_0 \mathcal{U} \end{pmatrix} \begin{pmatrix} \mathbf{E}_0^t \\ \mathbf{J}_0 \end{pmatrix} = \begin{pmatrix} 0 \\ \mathbf{E}^{t,i} \end{pmatrix}. \tag{7.15}$$

It is well-known that this formulation suffers from internal resonances, more precisely at the Dirichlet eigenfrequencies of the interior structure filled with background medium [15]. This occurs because of the non-uniqueness of the EFIE for the background medium. In order to verify this, the PS operator $\tilde{\mathcal{Y}}_0$ is first identified in the sourceless EFIE, as in (7.8), and after substitution of the first equation into this expression, we find for the electric current:

$$\eta_0 \mathcal{U} \left(\tilde{\mathcal{Y}}_0 \mathcal{Y}_1^{-1} + \mathcal{I} \right) \mathbf{J}_0 = 0. \tag{7.16}$$

This leads to $\mathbf{J}_0 = 0$, unless $\eta_0 \mathcal{U}$ or $\left(\tilde{\mathcal{Y}}_0 \mathcal{Y}_1^{-1} + \mathcal{I} \right)$ becomes singular. In Section 7.2.3 it was already shown that the singularity of the latter leads to physical resonances, so spurious resonances are only present when $\eta_0 \mathcal{U}$ is singular. As already demonstrated in Section 7.2.2, this occurs at the Dirichlet eigenfrequencies of the interior structure filled with background material. At these frequencies we thus find a non-radiating resonant spurious electric current $\mathbf{J}_{\text{sp}}$ and a radiating induced spurious tangential electric field $\mathbf{E}_{\text{sp}}^t = -\mathcal{Y}_1^{-1} \mathbf{J}_{\text{sp}}$.

7.3.2 EFF and MFIE

Another approach is to combine the EFF and the MFIE. Now (7.2) and the second equation of (7.3) are utilised to form the following system:

$$\begin{pmatrix} \mathcal{Y}_1 & \mathcal{I} \\ -\frac{1}{\eta_0} \mathcal{N} \mathcal{U} \mathcal{N} & -\mathcal{K} + \frac{1}{2}\mathcal{I} \end{pmatrix} \begin{pmatrix} \mathbf{E}_0^t \\ \mathbf{J}_0 \end{pmatrix} = \begin{pmatrix} 0 \\ \mathbf{J}^i \end{pmatrix}. \tag{7.17}$$

This formulation also suffers from internal resonances, but now at the Neumann eigenfrequencies of the interior structure filled with background medium, due to the non-uniqueness of the MFIE. This is again verified after identification of $\tilde{\mathcal{Y}}_0$ in the homogeneous matrix system. Making use of (7.9), and after substitution of the first equation into this expression, we find:

$$\frac{1}{\eta_0}\mathcal{N}\mathcal{U}\mathcal{N}\left(\mathcal{I}+\tilde{\mathcal{Y}}_0^{-1}\mathcal{Y}_1\right)\mathbf{E}_0^t=0. \tag{7.18}$$

This leads to $\mathbf{E}_0^t=0$, unless $\frac{1}{\eta_0}\mathcal{N}\mathcal{U}\mathcal{N}$ or $\left(\mathcal{I}+\tilde{\mathcal{Y}}_0^{-1}\mathcal{Y}_1\right)$ is singular. Again, it was already shown in Section 7.2.3 that the singularity of $\left(\mathcal{I}+\tilde{\mathcal{Y}}_0^{-1}\mathcal{Y}_1\right)$ leads to physical resonances, which means that spurious solutions can only occur when $\frac{1}{\eta_0}\mathcal{N}\mathcal{U}\mathcal{N}$ is singular. It is shown in Section 7.2.2 that this occurs at the Neumann eigenfrequencies of the interior structure filled with background material. At these frequencies we thus find a non-radiating spurious tangential electric field $\mathbf{E}_{\text{sp}}$ and a radiating induced spurious electric current $\mathbf{J}_{\text{sp}}=-\mathcal{Y}_1\mathbf{E}_{\text{sp}}^t$.

Remark that these spurious solutions differ from the spurious solutions in Section 7.3.1, since in (7.18), they occur due to the non-uniqueness of the MFIE, whereas the spurious solutions in (7.16) exist because of the non-uniqueness of the EFIE.

7.3.3 EFF and CFIE

A solution to the problem in previous formulations is to employ the CFIE in the BIE domain [3]. The system matrix then becomes a linear combination of the system matrices in 7.3.1 and 7.3.2. We get

$$\begin{aligned}\{\alpha\begin{pmatrix}\mathcal{Y}_1 & \mathcal{I}\\ \mathcal{K}'+\frac{1}{2} & \eta_0\mathcal{U}\end{pmatrix}+(1-\alpha)\begin{pmatrix}\mathcal{Y}_1 & \mathcal{I}\\ -\mathcal{N}\mathcal{U}\mathcal{N} & \eta_0\left(-\mathcal{K}+\frac{1}{2}\right)\end{pmatrix}\}\begin{pmatrix}\mathbf{E}_0^t\\ \mathbf{J}_0\end{pmatrix}\\ =\begin{pmatrix}0\\ \alpha\mathbf{E}^{t,i}+(1-\alpha)\eta_0\mathbf{J}^i\end{pmatrix},\end{aligned} \tag{7.19}$$

with $0<\alpha<1$. Using (7.7), the sourceless matrix system becomes

$$\begin{aligned}\{\alpha\begin{pmatrix}\mathcal{Y}_1 & \mathcal{I}\\ -\eta_0\mathcal{U}\tilde{\mathcal{Y}}_0 & \eta_0\mathcal{U}\end{pmatrix}+(1-\alpha)\begin{pmatrix}\mathcal{Y}_1 & \mathcal{I}\\ \eta_0\left(\mathcal{K}-\frac{1}{2}\right)\tilde{\mathcal{Y}}_0 & \eta_0\left(-\mathcal{K}+\frac{1}{2}\right)\end{pmatrix}\}\begin{pmatrix}\mathbf{E}_0^t\\ \mathbf{J}_0\end{pmatrix}\\ =\begin{pmatrix}0\\ 0\end{pmatrix}.\end{aligned} \tag{7.20}$$

First of all, note that the spurious solutions of Section 7.3.1 and Section 7.3.2 can never be solutions of this system, since they are different from each other, as explained in the previous section and in [23]. Therefore, at the Dirichlet and Neumann eigenfrequencies of the interior structure filled with background medium, the solution of (7.20) will be zero. Possible spurious solutions for the electric current can be found by substituting the first equation of (7.20) into the second one. We obtain:

$$\left(\alpha\eta_0\mathcal{U} + (1-\alpha)\,\eta_0\left(-\mathcal{K} + \frac{1}{2}\right)\right)\left(\tilde{\mathcal{Y}}_0\mathcal{Y}_1^{-1} + \mathcal{I}\right)\mathbf{J}_0 = 0. \tag{7.21}$$

With the transposed equation of (7.5a), this is further simplified to

$$\left(\alpha + (1-\alpha)\,\eta_0\mathcal{Y}_0\right)\eta_0\mathcal{U}\left(\tilde{\mathcal{Y}}_0\mathcal{Y}_1^{-1} + \mathcal{I}\right)\mathbf{J}_0 = 0. \tag{7.22}$$

This leads to $\mathbf{J}_0 = 0$, unless $\left(\alpha + (1-\alpha)\,\eta_0\mathcal{Y}_0\right)$ or $\eta_0\mathcal{U}$ or $\left(\tilde{\mathcal{Y}}_0\mathcal{Y}_1^{-1} + \mathcal{I}\right)$ is singular. We already know that the singularity of the latter corresponds with physical resonances and that the singularity of $\eta_0\mathcal{U}$ cannot lead to internal resonances since it occurs at the Dirichlet eigenfrequencies of the interior structure filled with background medium. Hence, it is clear that spurious solutions can only exist when $\left(\alpha + (1-\alpha)\,\eta_0\mathcal{Y}_0\right)$ is singular. Therefore, $\frac{\alpha}{(\alpha-1)\eta_0}$ has to be an eigenvalue of $\mathcal{Y}_0$ (or $\frac{(\alpha-1)\eta_0}{\alpha}$ an eigenvalue of $\mathcal{Y}_0^{-1}$). This means that $\mathcal{Y}_0$ should have a real non-zero eigenvalue. However, for a lossless reciprocal medium, $\mathcal{Y}_0$ is a pure imaginary symmetric matrix, so it possesses only imaginary eigenvalues. Therefore, no internal resonances are present.

The proof for the tangential electric field is similar and leads to the same conclusions.

7.3.4 EFF + MFIE and EFIE

The last conformal formulation under study adds up the EFF and the MFIE in one equation and combines it with the EFIE in order to form a symmetric system. The system is then [18], [19]:

$$\begin{pmatrix} \mathcal{Y}_1 + \frac{1}{\eta_0}\mathcal{N}\mathcal{U}\mathcal{N} & \mathcal{K} + \frac{1}{2}\mathcal{I} \\ \mathcal{K}' + \frac{1}{2}\mathcal{I} & \eta_0\mathcal{U} \end{pmatrix}\begin{pmatrix} \mathbf{E}_0^t \\ \mathbf{J}_0 \end{pmatrix} = \begin{pmatrix} -\mathbf{J}^i \\ \mathbf{E}^{t,i} \end{pmatrix}. \tag{7.23}$$

Although one would expect that the solution of (7.23) is uniquely defined since both the EFIE and the MFIE are used to model the background medium, internal resonances are still present due to the construction of the hybrid system matrix. Indeed, after transposing (7.7a), we find that $\mathcal{K} + \frac{1}{2}\mathcal{I}$ and $\mathcal{U}$ have a shared nullspace:

$$\mathcal{K} + \frac{1}{2}\mathcal{I} = -\eta_0\tilde{\mathcal{Y}}_0\mathcal{U}. \tag{7.24}$$

Therefore, spurious solutions of the form $\begin{pmatrix}\mathbf{0} & \mathbf{J}_{\text{sp}}\end{pmatrix}^T$ can exist. From (7.5a), it is clear that this occurs at the Dirichlet eigenfrequencies of the interior structure filled with background material.

Remark that, in contrast to the internal resonances of Section 7.3.1 and Section 7.3.2, no tangential electric field is induced here.

7.4 Non-conformal hybrid FE-BIE formulations

A second group of hybrid formulations consists of non-conformal formulations. In these systems, the FE and BIE methods are independently discretised and the solutions are projected from one domain to the other. These projections can be calculated analytically and do not largely extend the simulation time [24]. A great advantage of these formulations is that higher order FE basis functions can be used in combination with first-order BIE basis functions. Also, domain decomposition techniques can be employed to solve the hybrid system.

Depending on the transmission conditions, different formulations exist. In this chapter, we focus on weak tangential continuity and Robin transmission conditions.

7.4.1 Tangential continuity

In this formulation, as described in Section 6.2.1, the transmission conditions are the continuity of the tangential electric and magnetic field at the boundary $\partial\Omega$:

$$\mathbf{E}_0^t = \mathbf{E}_1^t, \tag{7.25a}$$
$$\mathbf{J}_0 = -\mathbf{J}_1, \tag{7.25b}$$

which are applied in a weak sense. After combination with the EFF, EFIE and MFIE, the following symmetric system matrix is obtained:

$$\begin{pmatrix} \mathcal{Y}_1 & -\frac{1}{2}\mathcal{I} & 0 & \frac{1}{2}\mathcal{I} \\ -\frac{1}{2}\mathcal{I} & 0 & \frac{1}{2}\mathcal{I} & 0 \\ 0 & \frac{1}{2}\mathcal{I} & \frac{1}{\eta_0}\mathcal{N}\mathcal{U}\mathcal{N} & \mathcal{K} \\ \frac{1}{2}\mathcal{I} & 0 & \mathcal{K}' & \eta_0\mathcal{U} \end{pmatrix} \begin{pmatrix} \mathbf{E}_1^t \\ \mathbf{J}_1 \\ \mathbf{E}_0^t \\ \mathbf{J}_0 \end{pmatrix} = \begin{pmatrix} 0 \\ 0 \\ -\mathbf{J}^i \\ \mathbf{E}^{t,i} \end{pmatrix}. \tag{7.26}$$

It is clear that the continuity of the tangential electric field is explicitly enforced in the weak sense (in the second equation), whereas the continuity of the electric current is only implicitly defined. The investigation of internal resonances starts

from the sourceless matrix representation and after elimination of $\mathbf{E}_1^t$ we find:

$$\begin{pmatrix} -\frac{1}{2}\mathcal{I} & \mathcal{Y}_1 & \frac{1}{2}\mathcal{I} \\ \frac{1}{2}\mathcal{I} & \frac{1}{\eta_0}\mathcal{N}\mathcal{U}\mathcal{N} & \mathcal{K} \\ 0 & \mathcal{K}' + \frac{1}{2}\mathcal{I} & \eta_0\mathcal{U} \end{pmatrix} \begin{pmatrix} \mathbf{J}_1 \\ \mathbf{E}_0^t \\ \mathbf{J}_0 \end{pmatrix} = \begin{pmatrix} 0 \\ 0 \\ 0 \end{pmatrix}. \tag{7.27}$$

The electric current $\mathbf{J}_1$ can also be eliminated from the first equation and we obtain:

$$\begin{pmatrix} \mathcal{Y}_1 + \frac{1}{\eta_0}\mathcal{N}\mathcal{U}\mathcal{N} & \mathcal{K} + \frac{1}{2}\mathcal{I} \\ \mathcal{K}' + \frac{1}{2}\mathcal{I} & \eta_0\mathcal{U} \end{pmatrix} \begin{pmatrix} \mathbf{E}_0^t \\ \mathbf{J}_0 \end{pmatrix} = \begin{pmatrix} 0 \\ 0 \end{pmatrix}. \tag{7.28}$$

This is the same system matrix as (7.23), so the same spurious solutions will exist. This occurs at the Dirichlet eigenfrequencies of the interior structure filled with background medium.

7.4.2 Robin transmission conditions

This is the formulation of Section 6.2.2. For the configuration of Fig. 7.1, the Robin boundary conditions are given by

$$\mathbf{E}_0^t + \alpha\mathbf{J}_0 = \mathbf{E}_1^t - \alpha\mathbf{J}_1, \tag{7.29a}$$
$$\mathbf{E}_1^t + \alpha\mathbf{J}_1 = \mathbf{E}_0^t - \alpha\mathbf{J}_0. \tag{7.29b}$$

After combining the EFF, EFIE and MFIE, the following symmetric matrix representation is obtained [4]:

$$\begin{pmatrix} \mathcal{Y}_1 + \frac{1}{2\alpha}\mathcal{I} & -\frac{1}{2}\mathcal{I} & -\frac{1}{2\alpha}\mathcal{I} & \frac{1}{2}\mathcal{I} \\ -\frac{1}{2}\mathcal{I} & -\frac{1}{2}\alpha\mathcal{I} & \frac{1}{2}\mathcal{I} & -\frac{1}{2}\alpha\mathcal{I} \\ -\frac{1}{2\alpha}\mathcal{I} & \frac{1}{2}\mathcal{I} & \frac{1}{\eta_0}\mathcal{N}\mathcal{U}\mathcal{N} + \frac{1}{2\alpha}\mathcal{I} & \mathcal{K} \\ \frac{1}{2}\mathcal{I} & -\frac{1}{2}\alpha\mathcal{I} & \mathcal{K}' & \eta_0\mathcal{U} - \frac{1}{2}\alpha\mathcal{I} \end{pmatrix} \begin{pmatrix} \mathbf{E}_1^t \\ \mathbf{J}_1 \\ \mathbf{E}_0^t \\ \mathbf{J}_0 \end{pmatrix} = \begin{pmatrix} 0 \\ 0 \\ -\mathbf{J}^i \\ \mathbf{E}^{t,i} \end{pmatrix}. \tag{7.30}$$

Again, in order to find internal resonances, we start from the sourceless matrix representation and eliminate $\mathbf{E}_1^t$.

$$\begin{pmatrix} -\alpha\mathcal{Y}_1 - \mathcal{I} & \mathcal{Y}_1 & -\alpha\mathcal{Y}_1 \\ \mathcal{I} & \frac{1}{\eta_0}\mathcal{N}\mathcal{U}\mathcal{N} & \mathcal{K} + \frac{1}{2}\mathcal{I} \\ -\alpha\mathcal{I} & \mathcal{K}' + \frac{1}{2}\mathcal{I} & \eta_0\mathcal{U} - \alpha \end{pmatrix} \begin{pmatrix} \mathbf{J}_1 \\ \mathbf{E}_0^t \\ \mathbf{J}_0 \end{pmatrix} = \begin{pmatrix} 0 \\ 0 \\ 0 \end{pmatrix}. \tag{7.31}$$

The second and third equation can be replaced by the following linear combinations:

$$\begin{cases} -\eta_0 \left(\mathcal{K} + \frac{1}{2}\mathcal{I}\right)(\text{eq. 2}) + \mathcal{N}\mathcal{U}\mathcal{N}(\text{eq. 3}), \\ -\eta_0 \mathcal{U}(\text{eq. 2}) + \left(\mathcal{K}' - \frac{1}{2}\mathcal{I}\right)(\text{eq. 3}). \end{cases} \tag{7.32}$$

By applying the Calderón identities (see Section 5.3.4), this is simplified to

$$\begin{cases} \left(\eta_0 \left(\mathcal{K} + \frac{1}{2}\mathcal{I}\right) + \alpha \mathcal{N}\mathcal{U}\mathcal{N}\right)(\mathbf{J}_0 + \mathbf{J}_1) & = 0, \\ \left(\eta_0 \mathcal{U} + \alpha \left(\mathcal{K}' - \frac{1}{2}\mathcal{I}\right)\right)(\mathbf{J}_0 + \mathbf{J}_1) & = 0, \end{cases} \tag{7.33}$$

and after identifying the PS operator $\mathcal{Y}_0$ by means of (7.5), we find:

$$\begin{cases} \mathcal{N}\mathcal{U}\mathcal{N}\left(\mathcal{Y}_0^{-1} - \alpha\mathcal{I}\right)(\mathbf{J}_1 + \mathbf{J}_0) & = 0, \\ \left(\mathcal{K}' - \frac{1}{2}\right)\left(\mathcal{Y}_0^{-1} - \alpha\mathcal{I}\right)(\mathbf{J}_1 + \mathbf{J}_0) & = 0. \end{cases} \tag{7.34}$$

Hence, $\mathbf{J}_0 = -\mathbf{J}_1$, unless a shared nullspace is found between $\mathcal{N}\mathcal{U}\mathcal{N}\left(\mathcal{Y}_0^{-1} - \alpha\mathcal{I}\right)$ and $\left(\mathcal{K}' - \frac{1}{2}\right)\left(\mathcal{Y}_0^{-1} - \alpha\mathcal{I}\right)$. Therefore, α should be an eigenvalue of $\mathcal{Y}_0^{-1}$ (or $\frac{1}{\alpha}$ an eigenvalue of $\mathcal{Y}_0$). The same reasoning as for the CFIE can be used here to conclude that $\mathcal{Y}_0^{-1}$ only has imaginary non-zero eigenvalues if the background medium is lossless and reciprocal. So, for real $\alpha \neq \{0, \infty\}$, (7.31) becomes:

$$\begin{pmatrix} \mathcal{Y}_1 & \mathcal{I} \\ \frac{1}{\eta_0}\mathcal{N}\mathcal{U}\mathcal{N} & \mathcal{K} - \frac{1}{2}\mathcal{I} \\ \mathcal{K}' + \frac{1}{2}\mathcal{I} & \eta_0\mathcal{U} \end{pmatrix} \begin{pmatrix} \mathbf{E}_0^t \\ \\ \mathbf{J}_0 \end{pmatrix} = \begin{pmatrix} 0 \\ 0 \\ 0 \end{pmatrix}. \tag{7.35}$$

Here, both the EFIE and MFIE are solved for the background medium, so the solution will always be uniquely defined. Hence this formulation is free of internal resonances.

7.5 Numerical results

In this section, the above concepts are illustrated by means of numerical simulations. The configuration of the simulated problem is depicted in Fig. 7.2. A plane wave, travelling along the positive x-axis and with the electric field polarised along the positive y-axis, is scattered by a dielectric cuboid with dimensions $\{L, W, H\}$ and relative permittivity $\epsilon_r = 2$. As expansion functions, the curl conforming first-order edge elements $\mathbf{w}_i$ [25] are used for $\mathbf{E}_i^t$ and the divergence conforming RWGs $\mathbf{v}_i$ [26] are used for $\mathbf{J}_i$. We have that $\mathbf{w}_i = \mathbf{n}_i \times \mathbf{v}_i$. Galerkin weighting is applied in all formulations.

Remark that the Dirichlet and Neumann eigenfrequencies are equal for 3D configurations, because of the duality principle. In order to prove this, we use the example of Fig. 7.3. The eigenfrequencies of the Dirichlet problem in 7.3(a) are

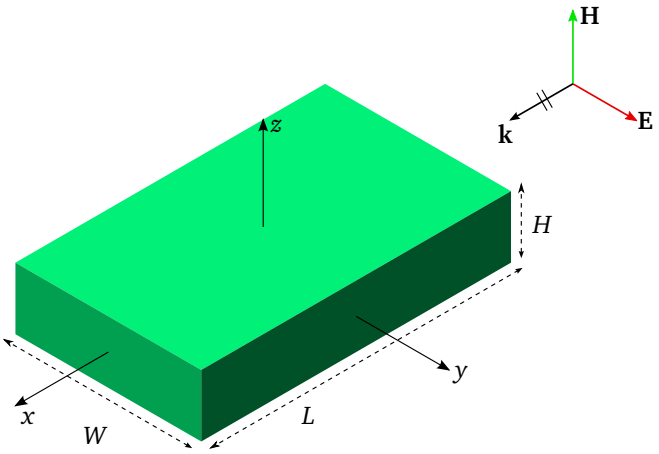

Figure 7.2: Configuration of the simulated problem. A plane wave is scattered by a dielectric cuboid with relative permittivity $\epsilon_r = 2$.

equal to the eigenfrequencies of Neumann the problem in 7.3(b) because the configurations are dual to each other. This is also true for the problems 7.3(c) and 7.3(d) (the terms Dirichlet and Neumann refer to the electric field solution). Now, since the eigenfrequencies are found from

$$\nabla \times \nabla \times \mathbf{E} - k^2 \mathbf{E} = 0, \tag{7.36}$$

it is clear that the eigensolutions are only frequency dependent through the wavenumber

$$k = \frac{2\pi f \sqrt{\epsilon_r \mu_r}}{c_0}. \tag{7.37}$$

This implies that the eigenfrequencies of Figs. 7.3(a) and 7.3(c) are also equal, because the wave number for both configurations is the same. Hence, the eigenfrequencies of 7.3(a) and 7.3(b) are equal. The latter two problems are the Dirichlet and Neumann problem of the same configuration, respectively. Hence, the Dirichlet and Neumann eigenfrequencies are equal.

7.5.1 Discretised PS operator

In (7.1), it was already shown that $\mathcal{Y}_1$ can be calculated by rescaling the Schur complement of the FE system matrix with $jk_0\eta_0$. If a Green's function kernel is available, such as for homogeneous regions Ω, the same operator can also be computed via the BIE method and the obtained matrices must be the same up to discretisation errors.

In order to obtain the BIE PS operator $\mathcal{Y}_1$, we expand the tangential electric field and the equivalent electric current in first-order edge element and RWG basis

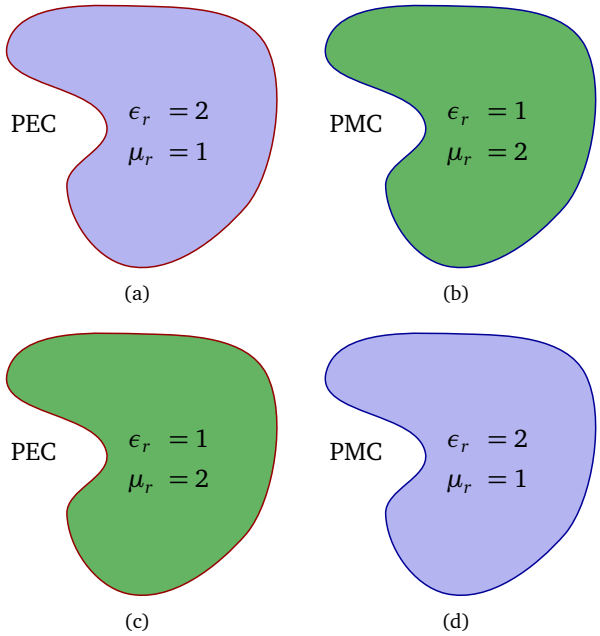

Figure 7.3: Example of the duality principle. Configuration (a) is dual to configuration (b) and configuration (c) is dual to configuration (d).

functions, respectively:

$$\mathbf{E}^t = \sum_{n=1}^{N} \chi_n \mathbf{w}_n, \tag{7.38a}$$

$$\mathbf{J} = \sum_{n=1}^{N} \xi_n \mathbf{v}_n. \tag{7.38b}$$

The discretised PS operator then becomes the complex symmetric $N \times N$ matrix Y, with

$$\mathsf{Y}_{ij} = \langle \mathbf{w}_i | \mathcal{Y} \mathbf{w}_j \rangle. \tag{7.39}$$

Here, both test and basis functions are the curl conforming first order edge elements $\mathbf{w}_i$, since $\mathcal{Y}_1$ operates on the tangential field $\mathbf{E}^t$ and results in an equivalent electric current that needs to be tested with functions from its dual space.

After inserting (7.38) into the sourceless Stratton-Chu formulation (7.4) and into

the definition of the PS operator ($\mathcal{Y}\mathbf{E}^t = \mathbf{J}$), we obtain [21]

$$\frac{1}{2}\mathsf{D}^T\chi = \mathsf{A}^T\chi + \eta_1\mathsf{B}\xi, \tag{7.40a}$$

$$\frac{1}{2}\eta_1\mathsf{D}\xi = -\mathsf{C}\chi - \eta_1\mathsf{A}\xi, \tag{7.40b}$$

$$\mathsf{Y}\chi = \mathsf{D}\xi, \tag{7.40c}$$

with χ and ξ the vectors containing the unknowns χ_n and ξ_n, and the $N \times N$ matrices $\mathsf{A}, \mathsf{B}, \mathsf{C}$ and D defined as

$$\mathsf{A}_{ij} = \langle \mathbf{w}_i | \mathcal{K}\mathbf{v}_j \rangle, \tag{7.41a}$$

$$\mathsf{B}_{ij} = \langle \mathbf{v}_i | \mathcal{U}\mathbf{v}_j \rangle, \tag{7.41b}$$

$$\mathsf{C}_{ij} = \langle \mathbf{w}_i | \mathcal{N}\mathcal{U}\mathcal{N}\mathbf{w}_j \rangle, \tag{7.41c}$$

$$\mathsf{D}_{ij} = \langle \mathbf{w}_i | \mathbf{v}_j \rangle. \tag{7.41d}$$

Note that the calculation is performed for the inner domain, so the Calderón operator $\mathcal{P}$ needs to be employed. Also, in order to obtain $\mathcal{Y}_1$, the Green's function $G_1(\mathbf{r}, \mathbf{r}')$ is used (with $\epsilon_r = 2$). Now, since the matrices B and C are complex symmetric, it is easily shown from (7.40) that the discretised PS operator can be written in an explicitly symmetric form as

$$\mathsf{Y} = \frac{1}{\eta_1}\left(-\mathsf{C} + \left(\frac{1}{2}\mathsf{D} - \mathsf{A}\right)^T \mathsf{B}^{-1}\left(\frac{1}{2}\mathsf{D} - \mathsf{A}\right)\right). \tag{7.42}$$

The matrices Y_{FE}, obtained from (7.1), and Y_{BIE}, obtained from (7.42), are now compared against each other for the problem of Fig. 7.2 with $\{L, W, H\} = \{1, 1, 1\}$ m at a frequency of 100 MHz. The matrix Y_{FE} is calculated twice, once with first-order FE basis functions and a second time with second-order FE basis functions. The mesh of the configuration is depicted in Fig. 7.4. It has an average edge length of 100 mm and leads to 2040 degrees of freedom on the boundary. Remark that, for the FE calculations, the interior mesh has the same average edge length as the boundary mesh. For the first-order FE computations, this leads to a total of 8086 unknowns and for the second-order FE computations, we have 41 815 unknowns.

The numerical equivalence of the PS operators is illustrated in Fig. 7.5, where the imaginary part of the 512th column of Y_{BIE} and Y_{FE} (obtained once via first-order and a second time via second-order FE basis functions) are compared. This column represents the interactions between the marked basis function in Fig. 7.4 and all other basis functions. In Fig. 7.5(a) the singular close interactions are shown and errors between the matrices are visible because only in the BIE method special routines were used to calculate these selfpatch integrals [27]. We also observed that this error became even worse when investigating the interactions between

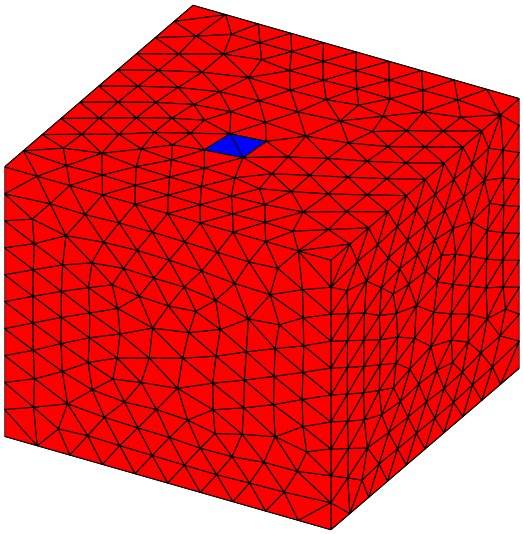

Figure 7.4: Mesh used to calculate the FE and BIE PS operator $\mathcal{Y}_1$. The interactions of the marked RWG with the other basis functions are displayed in Fig. 7.5.

basis functions on the edges or in corners. However, it is seen that the accuracy of Y_{FE} increases by using second-order FE basis functions.

Some non-singular interactions are shown in Fig. 7.5(b) and here we observe a very good match between the PS operators. The same results are obtained for the other columns.

7.5.2 Spurious solutions

In Sections 7.3 and 7.4, it was shown that internal resonances can occur at the Dirichlet and Neumann eigenfrequencies of the FE domain filled with background medium for the formulations under study. Here, we will demonstrate this for the scattering problem of Fig. 7.2 with $\{L, W, H\} = \{1.2, 0.5, 0.2\}$ m using a mesh with an average edge length of 70 mm. As mentioned before, the Dirichlet and Neumann eigenfrequencies are identical for 3D configurations and for a box, they are found from

$$f_{l,m,n} = \frac{c}{2\sqrt{\epsilon_r}} \sqrt{\frac{l^2}{1.2^2} + \frac{m^2}{0.5^2} + \frac{n^2}{0.2^2}}. \tag{7.43}$$

These frequencies are shown in Table 7.1 for both the background medium ($\epsilon_r = 1$) and the dielectric medium ($\epsilon_r = 2$). The numerical simulations are then performed as follows. A reference solution X_{PMCHWT} is first calculated by means of the pure BIE (PMCHWT) formulation and then a combined error in $\mathbf{E}_0^t$ and $\mathbf{J}_0$

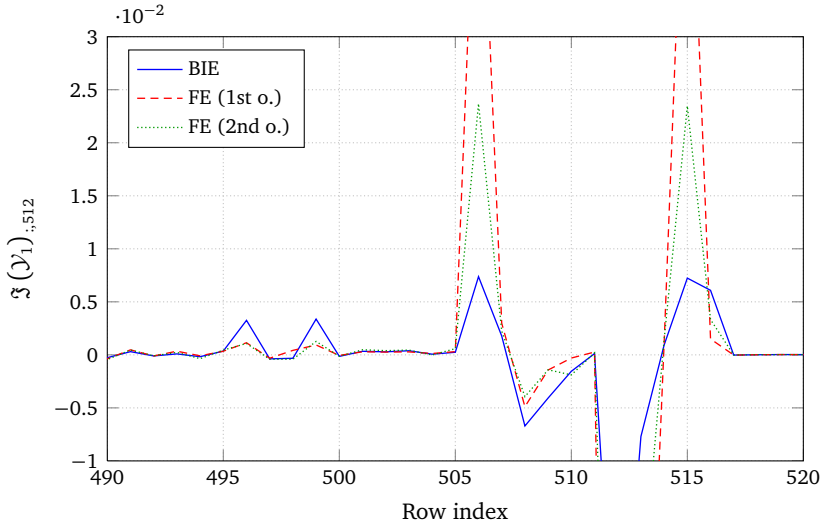

(a)

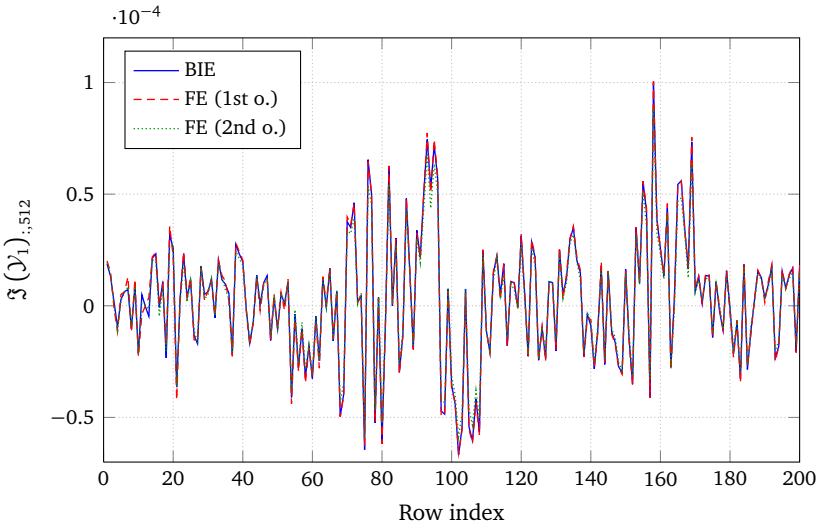

(b)

Figure 7.5: Imaginary part of the 512th column of the discretised PS operators $\mathsf{Y}_{\mathrm{BIE}}$ and Y_{FE}, where the FE PS operator is calculated once with first-order basis functions and a second time with second-order basis functions. Some singular (a) and non-singular (b) interactions are shown.

with respect to this solution is computed using the solution vectors X for each of

Table 7.1: Eigenfrequencies of the vacuum and dielectric cuboid.

mode (l,m,n)	f [MHz] for $\epsilon_r = 1$	f [MHz] for $\epsilon_r = 2$
$(1,0,0)$	124.913524	88.327200
$(2,0,0)$	249.827048	176.654400
$(0,1,0)$	299.792458	211.985280
$(1,1,0)$	324.775163	229.650720
$(3,0,0)$	374.740572	264.981600
$(2,1,0)$	390.242325	275.942994
$(3,1,0)$	479.902089	339.342021

the formulations under study:

$$\epsilon = \frac{||X - X_{\text{PMCHWT}}||}{||X_{\text{PMCHWT}}||}. \tag{7.44}$$

The error for the conformal formulations is shown in Fig. 7.6(a) for a frequency range from 300 MHz to 350 MHz and the corresponding condition numbers of the hybrid system matrices are displayed in Fig. 7.6(b). As expected, all conformal formulations exhibit spurious solutions except the formulation of 7.3.3, where the CFIE was computed with $\alpha = 0.5$. The breakdown frequency of formulations 7.3.1 and 7.3.4 occurs exactly as predicted, whereas it has shifted towards lower frequencies for formulation 7.3.2. This is because different integration routines were used to calculate the BIE interactions in formulation 7.3.2 (in a Galerkin scheme, these interactions form an $\mathbf{n}\times$MFIE formulation). Moreover, the $\mathcal{K}$ operator is not well tested in this formulation, what leads to the broader error peak. A solution would be to employ Buffa-Christiansen test functions for the second equation [28], [29], but then there is no Galerkin testing anymore. Also note that with these test functions, the formulation still suffers from internal resonances, since these occur in the continuous problem, independent from any discretisation.

Observing Fig. 7.6(b), we see that the condition number increases for all formulations that have breakdown frequencies around 325 MHz. Other increases of the condition numbers are also observed at 337 MHz and 346 MHz. These peaks are a bifurcation of the expected peak at 339 MHz, due to the singularity of $\mathcal{Y}_1$. Although, it is clear from Fig. 7.6(a) that this does not contribute to errors on the solution vector.

Fig. 7.7(a) compares the solution error defined by (7.44) for the non-conformal FE-BIE formulations discussed in Section 7.4. Since these formulations completely decouple the FE and BIE discretisations, it is also possible to compare the solutions from FE-BIE formulations with second-order FE basis functions. As explained in the previous section, the formulation imposing weak tangential continuity of

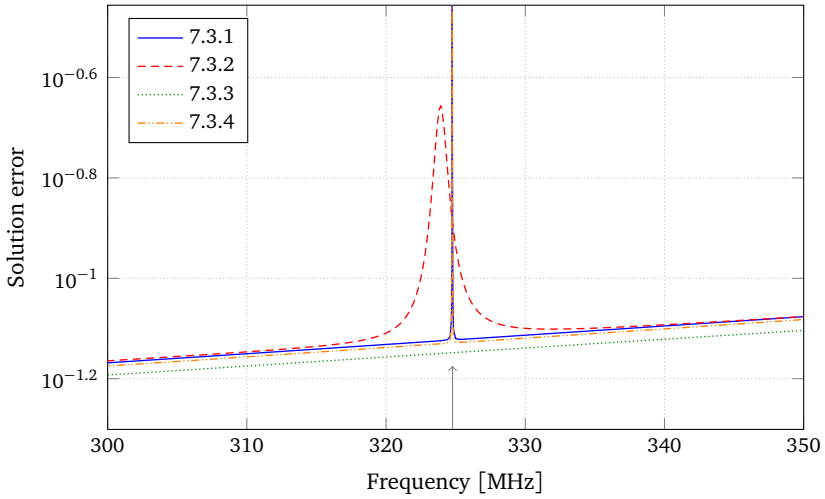

(a)

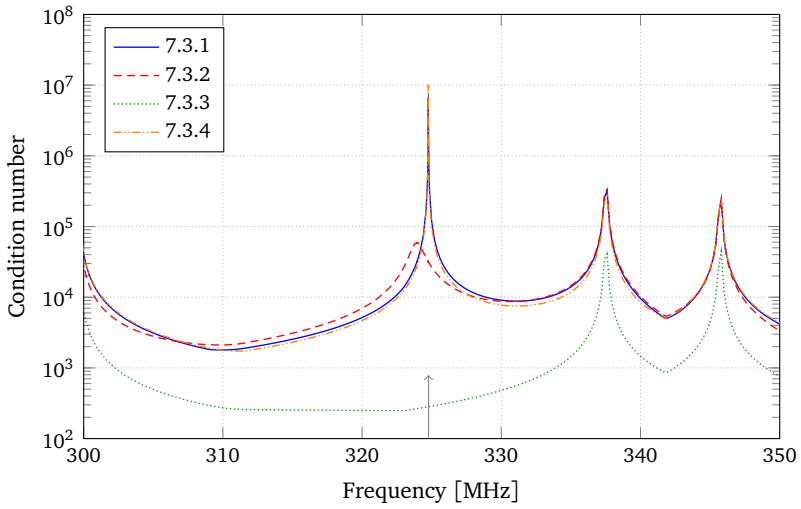

(b)

Figure 7.6: Combined error of the solutions of the conformal formulations with respect to the reference PMCHWT solution (a) and the corresponding condition numbers of the hybrid system matrices (b). The theoretical breakdown frequency is shown by the vertical arrow.

electric and magnetic fields suffers from internal resonances, whereas the Robin boundary conditions (with $\alpha = \eta_0$) lead to a resonance-free solution. A difference in accuracy between first and second-order FE basis functions is also noticeable.

The condition numbers of the system matrices of the non-conformal formulations are shown in Fig. 7.7(b). The resonance of $\mathcal{Y}_1$ can be noticed for these formulations too and the bifurcation has disappeared for the formulations with second-order FE basis functions. Again, this resonance does not contribute to errors on the solution vector, as illustrated in Fig. 7.7(a).

7.5.3 Radiating vs. non-radiating spurious solutions

In Section 7.3, it was already shown that not all spurious solutions radiate. The internal resonance solutions of the PEC or PMC cavity filled with background material produce a non-zero field in the cavity, but do not radiate outside Ω, whereas the solutions that are induced by these resonance currents or fields do radiate outside the cavity. Here, we will demonstrate this for the example of Fig. 7.2 with $\{L, W, H\} = \{1.2, 0.5, 0.2\}$ m using a mesh with an average edge length of 70 mm. The normalised radar cross section (RCS) σ/λ^2 is first calculated in the yz-plane at a frequency of 324.75 MHz by means of a reference PMCHWT formulation. This RCS is then compared with the RCS obtained from each of the spurious solutions of Section 7.3 and Section 7.4.

Fig. 7.8(a) displays the RCS in the yz-plane for the reference PMCHWT solution and for the spurious tangential electric fields $\mathbf{E}_{\text{sp}}$ of the formulations in 7.3.1 and 7.3.2. The spurious tangential electric field of formulation 7.3.1 is induced by a resonant current and one can observe that this produces a spurious RCS with the same order of magnitude as the correct reference RCS. The field radiated by the spurious tangential electric field of formulation 7.3.2 is clearly much lower in magnitude and it can be concluded that these spurious solutions do not radiate.

In Fig. 7.8(b), the RCS in the yz-plane is shown for the reference PMCHWT solution and for the spurious electric currents $\mathbf{J}_{\text{sp}}$ of the formulations in 7.3.1, 7.3.2, 7.3.4 and 7.4.1. Again, it is clear that only the currents that are induced by a resonant tangential electric field radiate, whereas the internal resonant currents do not produce a field outside Ω.

7.6 Conclusion

In this chapter the stability of several conformal and non-conformal hybrid FE-BIE formulations was analysed by identifying the Poincaré-Steklov operator in the system matrices. This method identifies and explains all internal resonances and even predicts their frequencies for simple configurations.

All conformal formulations except the EFF-CFIE formulation exhibited spurious solutions at the Dirichlet or Neumann eigenfrequencies of the FE domain filled with background medium. We also proved that the EFF-CFIE system is free of internal resonances because the PS operator $\mathcal{Y}_0$ has no real eigenvalues.

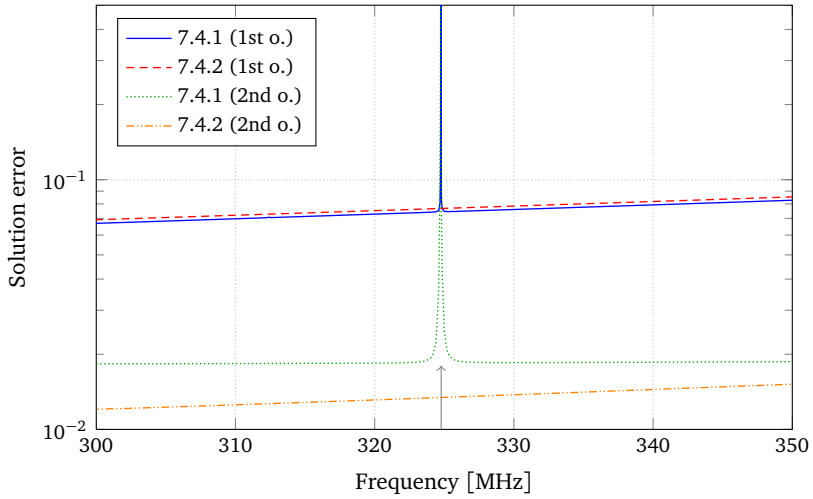

(a)

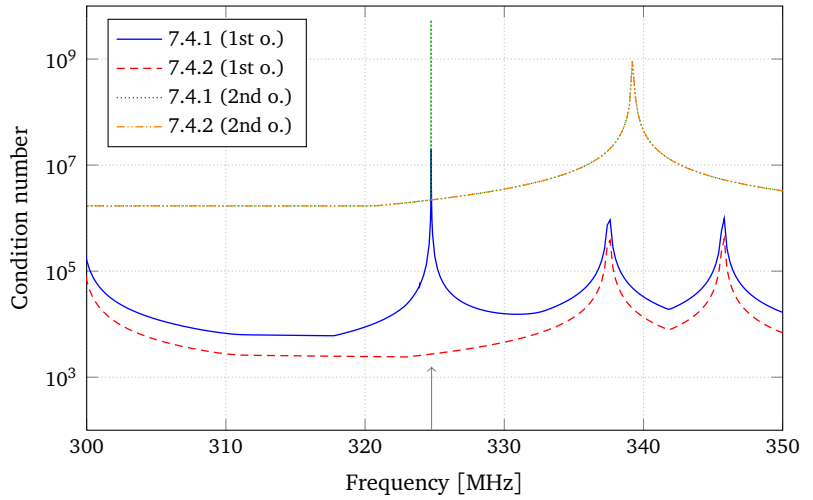

(b)

Figure 7.7: Combined error of the solutions of the non-conformal formulations with respect to the reference PMCHWT solution (a) and the corresponding condition numbers of the hybrid system matrices (b). The theoretical breakdown frequency is shown by the vertical arrow.

The non-conformal formulations under study were the formulation with weak tangential continuity of electric and magnetic fields at the interface and the formulation with Robin boundary conditions. It was shown that tangential continuity

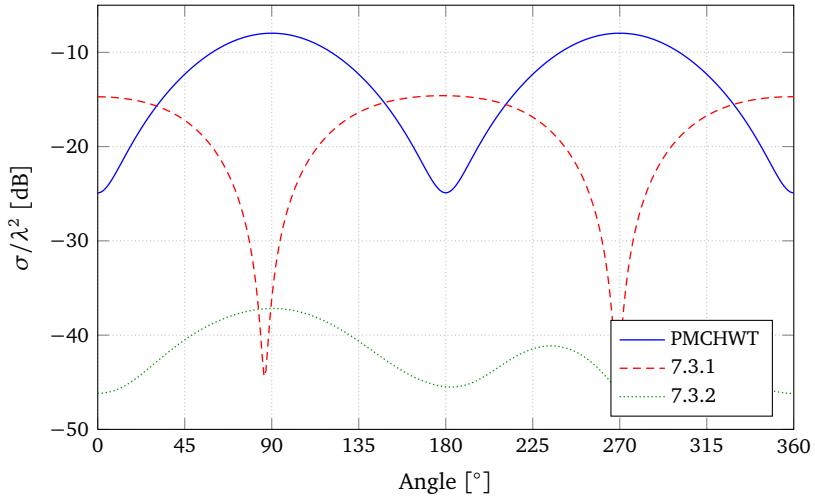

(a)

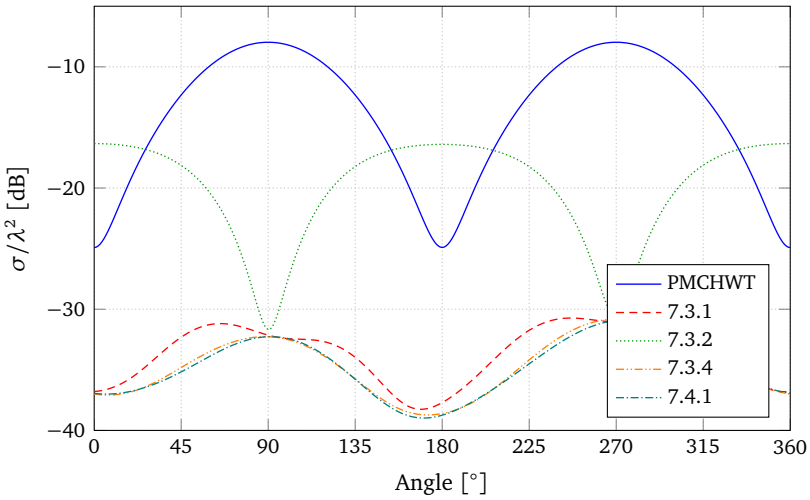

(b)

Figure 7.8: RCS in the yz-plane for the spurious tangential electric fields (a) and the spurious electric currents (b). The RCS calculated from a reference PMCHWT solution is also displayed in order to compare the order of magnitude.

leads to spurious solutions and that Robin boundary conditions are free from internal resonances as long as the parameter α is real and different from $\{0, \infty\}$.

The equivalence between the discretised FE and BIE PS operators was also demonstrated. However, a mismatch between the singular selfpatch interactions was

found due to numerical issues. Furthermore, the theory was verified for a scattering problem and it was shown that only the induced resonance currents (or fields) radiate outside the cavity.

References

[1] T. Cwik, "Coupling finite element and integral equation solutions using decoupled boundary meshes", *IEEE Trans. Antennas Propag.*, vol. 40, no. 12, pp. 1496–1504, Dec. 1992.

[2] D. J. Hoppe, L. W. Epp, and J.-F. Lee, "A hybrid symmetric FEM/MOM formulation applied to scattering by inhomogeneous bodies of revolution", *IEEE Trans. Antennas Propag.*, vol. 42, no. 6, pp. 798–805, Apr. 1994.

[3] J. L. Volakis, K. Sertel, and B. C. Usner, *Frequency Domain Hybrid Finite Element Methods for Electromagnetics*, C. A. Balanis, Ed. Morgan & Claypool, 2006.

[4] K. Zhao, M. N. Vouvakis, and J.-F. Lee, "Solving electromagnetic problems using a novel symmetric FEM-BEM approach", *IEEE Trans. Magn.*, vol. 42, no. 4, pp. 583–586, Apr. 2006.

[5] E. Arvas and J. R. Mautz, "On the non-uniqueness of the surface EFIE applied to multiple conducting and/or dielectric bodies", *Archiv für Elektronik und Übertragungstechnik (AEÜ)*, vol. 42, no. 6, pp. 364–369, 1988.

[6] B.-S. Yang, A. W. Glisson, and P. M. Goggans, "Interior resonance problems associated with hybrid integral equation/partial differential equation methods", in *Antennas and Propagation Society International Symposium, 1992. AP-S. 1992 Digest. Held in Conjuction with: URSI Radio Science Meeting and Nuclear EMP Meeting., IEEE*, vol. 2, Jul. 1992, pp. 781–784.

[7] J.-J. Angélini, C. Soize, and P. Soudais, "Hybrid numerical method for harmonic 3-D Maxwell equations: scattering by a mixed conducting and inhomogeneous anisotropic dielectric medium", *IEEE Trans. Antennas Propag.*, vol. 41, no. 1, pp. 66–76, Jan. 1993.

[8] X.-Q. Sheng, J.-M. Jin, J. Song, C.-C. Lu, and W. C. Chew, "On the formulation of hybrid finite-element and boundary-integral methods for 3-D scattering", *IEEE Trans. Antennas Propag.*, vol. 46, no. 3, pp. 303–311, Mar. 1998.

[9] Y. Ji, H. Wang, and T. H. Hubbing, "A numerical investigation of interior resonances in the hybrid FEM/MoM method", *IEEE Trans. Antennas Propag.*, vol. 51, no. 2, pp. 347–349, Feb. 2003.

[10] M. Smith and A. Peterson, "Numerical solution of the CFIE using vector bases and dual interlocking meshes", *IEEE Trans. Antennas Propag.*, vol. 53, no. 10, pp. 3334–3339, Oct. 2005.

[11] F. Andriulli and E. Michielssen, "A regularized combined field integral equation for scattering from 2-D perfect electrically conducting objects", *IEEE Trans. Antennas Propag.*, vol. 55, no. 9, pp. 2522–2529, Sep. 2007.

[12] S. Yan, J.-M. Jin, and Z. Nie, "Calderón preconditioner: from EFIE and MFIE to N-Müller equations", *IEEE Trans. Antennas Propag.*, vol. 58, no. 12, pp. 4105–4110, Dec. 2010.

[13] J. Collins, J.-M. Jin, and J. Volakis, "Eliminating interior resonances in finite element-boundary integral methods for scattering", *IEEE Trans. Antennas Propag.*, vol. 40, no. 12, pp. 1583 –1585, Dec. 1992.

[14] W. C. Chew and J. M. Song, "Gedanken experiments to understand the internal resonance problems of electromagnetic scattering", *Electromagnetics*, vol. 27, no. 8, pp. 457–471, Nov. 2007.

[15] W. C. Chew, M. S. Tong, and B. Hu, *Integral Equation Methods for Electromagnetic and Elastic Waves*, C. A. Balanis, Ed. Morgan & Claypool, 2008.

[16] D. Jiao, A. Ergin, B. Shanker, E. Michielssen, and J.-M. Jin, "A fast higher-order time-domain finite element-boundary integral method for 3-D electromagnetic scattering analysis", *IEEE Trans. Antennas Propag.*, vol. 50, no. 9, pp. 1192–1202, Sep. 2002.

[17] M. Lu, B. Shanker, and E. Michielssen, "Elimination of spurious solutions associated with exact transparent boundary conditions in FDTD solvers", *IEEE Antennas Wireless Propag. Lett.*, vol. 3, pp. 59–62, Dec. 2004.

[18] M. Vouvakis, S.-C. Lee, K. Zhao, and J.-F. Lee, "A symmetric FEM-IE formulation with a single-level IE-QR algorithm for solving electromagnetic radiation and scattering problems", *IEEE Trans. Antennas Propag.*, vol. 52, no. 11, pp. 3060 –3070, Nov. 2004.

[19] M. M. Botha and J.-M. Jin, "On the variational formulation of hybrid finite element-boundary integral techniques for electromagnetic analysis", *IEEE Trans. Antennas Propag.*, vol. 52, no. 11, pp. 3037–3047, Nov. 2004.

[20] P. Demarcke and H. Rogier, "The Poincaré-Steklov operator in hybrid Finite Element-Boundary Integral Equation formulations", *IEEE Antennas Wireless Propag. Lett.*, vol. 10, pp. 503–506, May 2011.

[21] L. Knockaert and D. De Zutter, "On the complex symmetry of the Poincaré-Steklov operator", *Progress In Electromagnetics Research B*, vol. 7, pp. 145–157, 2008.

[22] S. R. Garcia and M. Putinar, "Complex symmetric operators and applications", *Transactions of the American Mathematical Society*, vol. 358, no. 3, pp. 1285–1315, May 2005.

[23] J. G. Van Bladel, *Electromagnetic Fields*, 2nd, D. G. Dudley, Ed. John Wiley and Sons, Inc., 2007.

[24] F. Boeykens, H. Rogier, J. Van Hese, J. Sercu, and T. Boonen, "Efficient calculation of coupling matrices for a decoupled FE/BIE formulation", in *Electromagnetics in Advanced Applications (ICEAA), 2012 International Conference on*, 2012, pp. 506 –509.

[25] J.-C. Nédélec, "Mixed finite elements in R3", *Numerische Mathematik*, vol. 35, pp. 315–341, 1980.

[26] S. M. Rao, D. R. Wilton, and A. W. Glisson, "Electromagnetic scattering by surfaces of arbitrary shapes", *IEEE Trans. Antennas Propag.*, vol. 30, no. 3, pp. 409–418, May 1982.

[27] J. Peeters, I. Bogaert, and D. De Zutter, "Calculation of MoM interaction integrals in highly conductive media", *IEEE Trans. Antennas Propag.*, vol. 60, no. 2, pp. 930–940, Feb. 2012.

[28] K. Cools, F. P. Andriulli, F. Olyslager, and E. Michielssen, "Improving the MFIE's accuracy by using a mixed discretization", in *Antennas and Propagation Society International Symposium, 2009. APSURSI '09. IEEE*, Jun. 2009, pp. 1–4.

[29] S. Yan, J.-M. Jin, and Z. Nie, "Improving the accuracy of the second-kind Fredholm integral equations by using the Buffa-Christiansen functions", *IEEE Trans. Antennas Propag.*, vol. 59, no. 4, pp. 1299–1310, Apr. 2011.

Conclusions

General conclusions

The main objective of this thesis was to provide efficient and accurate solutions for the computer-aided design of flexible antennas that operate in non-ideal environments, since 2.5D simulation software is only capable of modelling the antennas in flat state and embedded in free space.

Therefore, we demonstrated in Part I how such 2.5D simulations can be validated in realistic conditions by means of a posteriori measurements. Also, an analytical model was proposed for computing the resonance frequency and the radiation patterns of flexible antennas in bent state. This model was further expanded for situations where the bending radius can fluctuate, but where a statistical distribution of the radius is known (or can be fitted).

In Part II, we developed a 3D non-conformal hybrid FE-BIE method, which takes into account the finite dimensions of the antenna substrates and is also capable of modelling objects in the near field of the antenna. The accuracy and some properties of the hybrid method were demonstrated by means of numerical examples. We also investigated the occurrence of internal resonances in different hybrid formulations based on a general rigorous operator theory. This provided insight in how to combine the FE and BIE method correctly in order to avoid spurious solutions.

Future work

The analytical cavity model for computing the resonance frequencies and radiation patterns of bent antennas is limited to rectangular patch antennas that are cylindrically bent. It can therefore be interesting to investigate the accuracy for other antenna types and to adapt the model if necessary. Also, when considering the deployment of flexible antennas on a human torso, it is possible that antennas are bent in two directions. In that case, the cylindrical model has to be extended to ellipsoidal surfaces.

Concerning the hybrid FE-BIE formulation, we demonstrated by means of the design of a planar patch antenna that the construction of the Schur complement of the FE system matrix forms the bottleneck of the program. However, in [1], it was proven that this Schur complement is of low-rank and that is has similar rank-structured properties as the BIE matrices. Therefore, it might be possible to accelerate the calculation of the Schur complement by means of hierarchical

matrix techniques, which forms a counterpart for the MLFMA applied in the BIE domains.

Another challenge for the hybrid FE-BIE formulation is to allow conductors or dielectric media to cross the FE-BIE boundary. This means that the FE bounding box is no longer a closed surface, resulting in junctions at the FE-BIE boundary, which have to be taken into account in a similar manner as in [2]. Moreover, it is highly likely that the FE and BIE discretisations will have to be conformal at these junctions in order to maintain sufficient accuracy.

References

[1] P. Demarcke, “Hybrid modeling and optimization techniques for antenna systems”, PhD thesis, Ghent University, 2011.

[2] P. Ylä-Oijala, M. Taskinen, and J. Sarvas, “Surface integral equation method for general composite metallic and dielectric structures with junctions”, *Progress In Electromagnetics Research*, vol. 52, pp. 81–108, 2005.

Appendices

A

Projection Integrands

A.1 Theory

Consider a closed and bounded domain Σ in n-dimensional Euclidean space $\mathbb{R}^n$ and let $\mathbf{a}$ be a point in $\mathbb{R}^n$. Next, consider a function $\Phi(\mathbf{r})$ which is defined and continuously differentiable over an open domain containing the conical domain

$$\Sigma(\mathbf{a}) = \{t\mathbf{r} + (1-t)\mathbf{a} : 0 < t \leq 1,\ \mathbf{r} \in \Sigma\}.$$

Then if

$$\lim_{t\to 0}\ t^n \Phi(t\mathbf{r} + (1-t)\mathbf{a}) = 0,$$

the following result is valid:

$$\int_{\Sigma} \Phi(\mathbf{r})\ \mathrm{d}V_n = \int_{\partial\Sigma} (\mathbf{r}-\mathbf{a})\cdot\mathbf{u}_n\ \mathrm{d}S_n \int_0^1 t^{n-1}\Phi(t\mathbf{r} + (1-t)\mathbf{a})\ \mathrm{d}t. \tag{A.1}$$

The scalar products of the different FE and BIE basis functions form the integrands for the projections, necessary to couple the FE and BIE systems. Using (A.1), the surface integral is transformed into a line integral and can be calculated analytically. Remark that the projections are 2D, since they are calculated per triangle-triangle overlap. Now, define

$$f(\mathbf{r},\mathbf{a}) = \int_0^1 t\Phi\left(t\mathbf{r} + (1-t)\mathbf{a}\right)\ \mathrm{d}t, \tag{A.2}$$

then the projection integral becomes

$$P = \int_{\partial\Sigma} (\mathbf{r}-\mathbf{a})\cdot\mathbf{u}_n\, f(\mathbf{r},\mathbf{a})\,\mathrm{d}S_n, \tag{A.3}$$

$$= \sum_i ||\mathbf{p}_{i+1}-\mathbf{p}_i||\,(\mathbf{p}_i-\mathbf{a})\cdot\mathbf{u}_n\, I(\mathbf{p}_i,\mathbf{p}_{i+1},\mathbf{a}), \tag{A.4}$$

with

$$I(\mathbf{p},\mathbf{q},\mathbf{a}) = \int_0^1 f\left((1-t)\mathbf{p}+t\mathbf{q},\mathbf{a}\right)\,\mathrm{d}t. \tag{A.5}$$

This last integral $I(\mathbf{p},\mathbf{q},\mathbf{a})$ is calculated here for the different scalar products of basis functions.

A.2 Definitions

A.2.1 Basis functions

The BIE domain is spanned by RWG basis functions. For the sake of simplicity, these are defined here without scaling factors, hence we have

$$\mathbf{RWG}_i(\mathbf{r}) = \mathbf{r}-\mathbf{b}_i. \tag{A.6}$$

In the FE domain, both edge and face basis function exist. These basis are defined based on triangle barycentric coordinates $(\lambda_0,\lambda_1,\lambda_2)$ and form a second order basis. The first and second order edge elements are

$$\mathbf{E}_1 = \lambda_0\nabla\lambda_1 - \lambda_1\nabla\lambda_0, \tag{A.7}$$

$$\mathbf{E}_2 = \lambda_0\nabla\lambda_1 + \lambda_1\nabla\lambda_0, \tag{A.8}$$

and the second order face element is defined as

$$\mathbf{F} = 4\lambda_0\left(\lambda_1\nabla\lambda_2 - \lambda_2\nabla\lambda_1\right). \tag{A.9}$$

A.2.2 Shorthand notations

Some shorthand notations will be used for the ease of reading. These are

$$\alpha(\lambda_i) = \sum_{\mathbf{v}=\mathbf{a},\mathbf{p},\mathbf{q}} \mathbf{v}\cdot\nabla\lambda_i,$$

$$\beta(\lambda_i,\mu_j) = \sum_{\mathbf{v}=\mathbf{a},\mathbf{p},\mathbf{q}} (\mathbf{v}\cdot\nabla\lambda_i)(\mathbf{v}\cdot\nabla\mu_j),$$

$$\gamma(\lambda_i,\mu_j,\nu_k) = \sum_{\mathbf{v}=\mathbf{a},\mathbf{p},\mathbf{q}} (\mathbf{v}\cdot\nabla\lambda_i)(\mathbf{v}\cdot\nabla\mu_j)(\mathbf{v}\cdot\nabla\nu_k),$$

and

$$\alpha_\times(\lambda_i) = \sum_{\mathbf{v}=\mathbf{a},\mathbf{p},\mathbf{q}} (\mathbf{n}\times\mathbf{v})\cdot\nabla\lambda_i,$$
$$\beta_\times(\lambda_i,\mu_j) = \sum_{\mathbf{v}=\mathbf{a},\mathbf{p},\mathbf{q}} \big((\mathbf{n}\times\mathbf{v})\cdot\nabla\lambda_i\big)\,(\mathbf{v}\cdot\nabla\mu_j),$$
$$\gamma_\times(\lambda_i,\mu_j,\nu_k) = \sum_{\mathbf{v}=\mathbf{a},\mathbf{p},\mathbf{q}} \big((\mathbf{n}\times\mathbf{v})\cdot\nabla\lambda_i\big)\,(\mathbf{v}\cdot\nabla\mu_j)(\mathbf{v}\cdot\nabla\nu_k).$$

A.3 Integrals

A.3.1 RWG and RWG

The scalar product $\Phi(\mathbf{r})$ is given by

$$\Phi(\mathbf{r}) = \big(\mathbf{r}-\mathbf{b}_1\big)\cdot\big(\mathbf{r}-\mathbf{b}_2\big), \tag{A.10}$$

and the integral becomes

$$I = \frac{1}{12}\Big(\mathbf{a}\cdot(\mathbf{a}+\mathbf{p}+\mathbf{q})+\mathbf{p}\cdot(\mathbf{p}+\mathbf{q})+\mathbf{q}\cdot\mathbf{q}\Big) - \frac{1}{6}\Big((\mathbf{a}+\mathbf{p}+\mathbf{q})\cdot(\mathbf{b}_1+\mathbf{b}_2)\Big) + \frac{1}{2}\mathbf{b}_1\cdot\mathbf{b}_2. \tag{A.11}$$

A.3.2 n×RWG and RWG

The scalar product $\Phi(\mathbf{r})$ is given by

$$\big(\mathbf{n}\times\big(\mathbf{r}-\mathbf{b}_1\big)\big)\cdot\big(\mathbf{r}-\mathbf{b}_2\big), \tag{A.12}$$

and the integral is

$$I = \frac{1}{6}\Big(\mathbf{n}\times\big(\mathbf{a}+\mathbf{p}+\mathbf{q}\big)\Big)\cdot\big(\mathbf{b}_1-\mathbf{b}_2\big) + \frac{1}{2}\big(\mathbf{n}\times\mathbf{b}_1\big)\cdot\mathbf{b}_2. \tag{A.13}$$

A.3.3 Edge and RWG

The scalar product $\Phi(\mathbf{r})$ is given by

$$\big(\xi_0\nabla\xi_1 \mp \xi_1\nabla\xi_0\big)\cdot(\mathbf{r}-\mathbf{b}). \tag{A.14}$$

Now, define $\mathbf{c}$ as the centroid of the edge triangle and

$$\begin{aligned} b(\lambda_i) &= \mathbf{b}\cdot\nabla\lambda_i,\\ c(\lambda_i) &= \mathbf{c}\cdot\nabla\lambda_i,\\ A_i &= \alpha(\xi_i) - 3b(\xi_i),\\ B_{ij} &= \big(\alpha(\xi_i) - 4c(\xi_i)\big)\big(\alpha(\xi_j) - 4b(\xi_j)\big),\\ C_{ij} &= \beta(\xi_i,\xi_j) - 4c(\xi_i)b(\xi_j). \end{aligned}$$

Then, with

$$I_1 = \frac{1}{18}A_1 + \frac{1}{24}\left(B_{01} + C_{01}\right),$$
$$I_2 = \frac{1}{18}A_0 + \frac{1}{24}\left(B_{10} + C_{10}\right),$$

the integral becomes

$$I = I_1 \mp I_2. \tag{A.15}$$

A.3.4 Face and RWG

The scalar product $\Phi(\mathbf{r})$ is given by

$$\left(4\xi_0(\xi_1\nabla\xi_2 - \xi_2\nabla\xi_1)\right)\cdot(\mathbf{r}-\mathbf{b}). \tag{A.16}$$

Now, define $\mathbf{c}$ as the centroid of the face triangle and

$$\begin{aligned}
b(\lambda_i) &= \mathbf{b}\cdot\nabla\lambda_i,\\
c(\lambda_i) &= \mathbf{c}\cdot\nabla\lambda_i,\\
A_i &= \alpha(\xi_i) - 3b(\xi_i),\\
B_{ij} &= \left(\alpha(\xi_i) - 4c(\xi_i)\right)\left(\alpha(\xi_j) - 4b(\xi_j)\right) + \beta(\xi_i,\xi_j) - 4c(\xi_i)b(\xi_j),\\
C_{ijk} &= \left(\alpha(\xi_i) - 5c(\xi_i)\right)\left(\alpha(\xi_j) - 5c(\xi_j)\right)\left(\alpha(\xi_k) - 5b(\xi_k)\right),\\
D_{ijk} &= \left(\alpha(\xi_i) - 5c(\xi_i)\right)\left(\beta(\xi_j,\xi_k) - 5c(\xi_j)b(\xi_k)\right)\\
E_{ijk} &= \left(\alpha(\xi_i) - 5b(\xi_i)\right)\left(\beta(\xi_j,\xi_k) - 5c(\xi_j)c(\xi_k)\right)\\
F_{ijk} &= \gamma(\xi_i,\xi_j,\xi_k) - 5c(\xi_i)c(\xi_j)b(\xi_k).
\end{aligned}$$

Then, with

$$I_1 = \frac{2}{27}A_2 + \frac{1}{18}\left(B_{02} + B_{12}\right) + \frac{1}{30}\left(C_{012} + D_{012} + D_{102} + E_{201} + 2F_{012}\right),$$
$$I_2 = \frac{2}{27}A_1 + \frac{1}{18}\left(B_{01} + B_{21}\right) + \frac{1}{30}\left(C_{021} + D_{021} + D_{201} + E_{102} + 2F_{021}\right),$$

the integral becomes

$$I = I_1 - I_2. \tag{A.17}$$

A.3.5 Edge and n×RWG

The scalar product $\Phi(\mathbf{r})$ is given by

$$\left(\xi_0\nabla\xi_1 \mp \xi_1\nabla\xi_0\right)\cdot(\mathbf{n}\times(\mathbf{r}-\mathbf{b})). \tag{A.18}$$

Now, define **c** as the centroid of the edge triangle and

$$\begin{aligned} b_\times(\lambda_i) &= (\mathbf{n}\times\mathbf{b})\cdot\nabla\lambda_i, \\ c(\lambda_i) &= \mathbf{c}\cdot\nabla\lambda_i, \\ A_i &= \alpha_\times(\xi_i) - 3b_\times(\xi_i), \\ B_{ij} &= \big(\alpha(\xi_i) - 4c(\xi_i)\big)\big(\alpha_\times(\xi_j) - 4b_\times(\xi_j)\big), \\ C_{ij} &= \beta(\xi_i,\xi_j) - 4c(\xi_i)b_\times(\xi_j). \end{aligned}$$

Then, with

$$\begin{aligned} I_1 &= \frac{1}{18}A_1 + \frac{1}{24}\left(B_{01} + C_{01}\right), \\ I_2 &= \frac{1}{18}A_0 + \frac{1}{24}\left(B_{10} + C_{10}\right), \end{aligned}$$

the integral becomes

$$I = I_1 \mp I_2. \tag{A.19}$$

A.3.6 Face and n×RWG

The scalar product $\Phi(\mathbf{r})$ is given by

$$\big(4\xi_0(\xi_1\nabla\xi_2 - \xi_2\nabla\xi_1)\big)\cdot(\mathbf{n}\times(\mathbf{r}-\mathbf{b})). \tag{A.20}$$

Now, define **c** as the centroid of the face triangle and

$$\begin{aligned} b_\times(\lambda_i) &= (\mathbf{n}\times\mathbf{b})\cdot\nabla\lambda_i, \\ c(\lambda_i) &= \mathbf{c}\cdot\nabla\lambda_i, \\ A_i &= \alpha_\times(\xi_i) - 3b_\times(\xi_i), \\ B_{ij} &= \big(\alpha(\xi_i) - 4c(\xi_i)\big)\big(\alpha_\times(\xi_j) - 4b_\times(\xi_j)\big) + \beta_\times(\xi_j,\xi_i) - 4c(\xi_i)b_\times(\xi_j), \\ C_{ijk} &= \big(\alpha(\xi_i) - 5c(\xi_i)\big)\big(\alpha(\xi_j) - 5c(\xi_j)\big)\big(\alpha_\times(\xi_k) - 5b_\times(\xi_k)\big), \\ D_{ijk} &= \big(\alpha(\xi_i) - 5c(\xi_i)\big)\big(\beta_\times(\xi_k,\xi_j) - 5c(\xi_j)b_\times(\xi_k)\big) \\ E_{ijk} &= \big(\alpha_\times(\xi_i) - 5b_\times(\xi_i)\big)\big(\beta(\xi_j,\xi_k) - 5c(\xi_j)c(\xi_k)\big) \\ F_{ijk} &= \gamma_\times(\xi_k,\xi_i,\xi_j) - 5c(\xi_i)c(\xi_j)b_\times(\xi_k). \end{aligned}$$

Then, with

$$\begin{aligned} I_1 &= \frac{2}{27}A_2 + \frac{1}{18}\left(B_{02} + B_{12}\right) + \frac{1}{30}\left(C_{012} + D_{012} + D_{102} + E_{201} + 2F_{012}\right), \\ I_2 &= \frac{2}{27}A_1 + \frac{1}{18}\left(B_{01} + B_{21}\right) + \frac{1}{30}\left(C_{021} + D_{021} + D_{201} + E_{102} + 2F_{021}\right), \end{aligned}$$

the integral becomes

$$I = I_1 - I_2. \tag{A.21}$$

A.3.7 Edge and edge

The scalar product $\Phi(\mathbf{r})$ is given by

$$\left(\xi_0\nabla\xi_1 \mp \xi_1\nabla\xi_0\right)\cdot\left(\chi_0\nabla\chi_1 \mp \chi_1\nabla\chi_0\right). \tag{A.22}$$

Now, define $\mathbf{c}$ as the centroid of the first edge triangle, $\mathbf{d}$ as the centroid of the second edge triangle and

$$\begin{aligned}
c(\lambda_i) &= \mathbf{c}\cdot\nabla\lambda_i,\\
d(\lambda_i) &= \mathbf{d}\cdot\nabla\lambda_i,\\
A_{ij} &= \alpha(\xi_i)+\alpha(\chi_i)-3\big(c(\xi_i)+d(\chi_i)\big),\\
B_{ij} &= \big(\alpha(\xi_i)-4c(\xi_i)\big)\big(\alpha(\chi_i)-4d(\chi_i)\big),\\
C_{ij} &= \beta(\xi_i,\chi_j)-4c(\xi_i)d(\chi_j).
\end{aligned}$$

Then, with

$$\begin{aligned}
I_1 &= \left(\frac{1}{18}(1+A_{00})+\frac{1}{24}(C_{00}+E_{00})\right)\left(\nabla\xi_1\cdot\nabla\chi_1\right),\\
I_2 &= \left(\frac{1}{18}(1+A_{01})+\frac{1}{24}(C_{01}+E_{01})\right)\left(\nabla\xi_1\cdot\nabla\chi_0\right),\\
I_3 &= \left(\frac{1}{18}(1+A_{10})+\frac{1}{24}(C_{10}+E_{10})\right)\left(\nabla\xi_0\cdot\nabla\chi_1\right),\\
I_4 &= \left(\frac{1}{18}(1+A_{11})+\frac{1}{24}(C_{11}+E_{11})\right)\left(\nabla\xi_0\cdot\nabla\chi_0\right).
\end{aligned}$$

the integral for the two first order elements becomes

$$I = I_1 - I_2 - I_3 + I_4, \tag{A.23}$$

the integral for a first order and a second order edge element is

$$I = I_1 + I_2 - I_3 - I_4, \tag{A.24}$$

the integral for a second order and a first order edge element becomes

$$I = I_1 - I_2 + I_3 - I_4, \tag{A.25}$$

and the integral for the two second order elements is

$$I = I_1 + I_2 + I_3 + I_4. \tag{A.26}$$

A.3.8 Edge and face

The scalar product $\Phi(\mathbf{r})$ is given by

$$\left(\xi_0\nabla\xi_1 \mp \xi_1\nabla\xi_0\right)\cdot\left(4\chi_0(\chi_1\nabla\chi_2 - \chi_2\nabla\chi_1)\right). \tag{A.27}$$

Now, define $\mathbf{c}$ as the centroid of the edge triangle, $\mathbf{d}$ as the centroid of the face triangle and

$$\begin{aligned}
c(\lambda_i) &= \mathbf{c}\cdot\nabla\lambda_i,\\
d(\lambda_i) &= \mathbf{d}\cdot\nabla\lambda_i,\\
A_{ijk} &= \alpha(\xi_i)+\alpha(\chi_j)+\alpha(\chi_k)-3\big(c(\xi_i)+d(\chi_j)+d(\chi_k)\big),\\
C_i &= \alpha(\xi_i)-4c(\xi_i),\\
D_i &= \alpha(\chi_i)-4d(\chi_i),\\
E_i &= \alpha(\xi_i)-5c(\xi_i),\\
F_i &= \alpha(\chi_i)-5d(\chi_i),\\
G_{ij} &= \beta(\xi_i,\chi_j)-4c(\xi_i)d(\chi_j),\\
H_{ij} &= \beta(\chi_i,\chi_j)-4c(\chi_i)d(\chi_j),\\
J_{ij} &= \beta(\xi_i,\chi_j)-5c(\xi_i)d(\chi_j),\\
K_{ij} &= \beta(\chi_i,\chi_j)-5c(\chi_i)d(\chi_j),\\
L_{ijk} &= \gamma(\xi_i,\chi_j,\chi_k)-5c(\xi_i)d(\chi_j)d(\chi_k).
\end{aligned}$$

Then, with

$$\begin{aligned}
I_{ijk} = \Big(&\frac{2}{27}(1+A_{ijk})+\frac{1}{18}(C_iD_j+C_iD_k+D_jD_k+G_{ij}+G_{ik}+H_{jk})\\
&+\frac{1}{30}(E_iF_jF_k+E_iK_{jk}+F_jJ_{ik}+F_kJ_{ij}+2L_{ijk})\Big)(\nabla\xi_{1-i}\cdot\nabla\chi_{3-j-k}),
\end{aligned}\tag{A.28}$$

the integral for the first order edge element and the face element becomes

$$I = I_{001}-I_{002}-I_{101}+I_{102}.\tag{A.29}$$

and the integral for the second order edge element and the face element is

$$I = I_{001}-I_{002}+I_{101}-I_{102}.\tag{A.30}$$

A.3.9 Face and face

The scalar product $\Phi(\mathbf{r})$ is given by

$$\big(4\xi_0(\xi_1\nabla\xi_2-\xi_2\nabla\xi_1)\big)\cdot\big(4\chi_0(\chi_1\nabla\chi_2-\chi_2\nabla\chi_1)\big).\tag{A.31}$$

Now, define $\mathbf{c}$ as the centroid of the first face triangle, $\mathbf{d}$ as the centroid of the second face triangle and

$$
\begin{aligned}
c(\lambda_i) &= \mathbf{c}\cdot\nabla\lambda_i,\\
d(\lambda_i) &= \mathbf{d}\cdot\nabla\lambda_i,\\
A_i &= \alpha(\xi_i) - 3c(\xi_i),\\
B_i &= \alpha(\chi_i) - 3d(\chi_i),\\
C_i &= \alpha(\xi_i) - 4c(\xi_i),\\
D_i &= \alpha(\chi_i) - 4d(\chi_i),\\
E_i &= \alpha(\xi_i) - 5c(\xi_i),\\
F_i &= \alpha(\chi_i) - 5d(\chi_i),\\
G_i &= \alpha(\xi_i) - 6c(\xi_i),\\
H_i &= \alpha(\chi_i) - 6d(\chi_i),\\
J_{ij} &= \beta(\xi_i,\xi_j) - 4c(\xi_i)c(\xi_j),\\
K_{ij} &= \beta(\xi_i,\chi_j) - 4c(\xi_i)d(\chi_j),\\
L_{ij} &= \beta(\chi_i,\chi_j) - 4d(\chi_i)d(\chi_j),\\
M_{ij} &= \beta(\xi_i,\xi_j) - 5c(\xi_i)c(\xi_j),\\
N_{ij} &= \beta(\xi_i,\chi_j) - 5c(\xi_i)d(\chi_j),\\
O_{ij} &= \beta(\chi_i,\chi_j) - 5d(\chi_i)d(\chi_j),\\
P_{ij} &= \beta(\xi_i,\xi_j) - 6c(\xi_i)c(\xi_j),\\
Q_{ij} &= \beta(\xi_i,\chi_j) - 6c(\xi_i)d(\chi_j),\\
R_{ij} &= \beta(\chi_i,\chi_j) - 6d(\chi_i)d(\chi_j),\\
S_{ijk} &= \gamma(\xi_i,\xi_j,\chi_k) - 5c(\xi_i)c(\xi_j)d(\chi_k),\\
T_{ijk} &= \gamma(\xi_i,\chi_j,\chi_k) - 5c(\xi_i)d(\chi_j)d(\chi_k),\\
U_{ijk} &= \gamma(\xi_i,\xi_j,\chi_k) - 78c(\xi_i)c(\xi_j)d(\chi_k),\\
V_{ijk} &= \gamma(\xi_i,\chi_j,\chi_k) - 78c(\xi_i)d(\chi_j)d(\chi_k),\\
W_{ijk} &= \alpha(\xi_i)\alpha(\xi_j)\alpha(\chi_k) - \alpha(\xi_i)\beta(\xi_j,\chi_k) - \alpha(\xi_j)\beta(\xi_i,\chi_k) - \alpha(\chi_k)\beta(\xi_i,\xi_j)\\
&\quad + 2\gamma(\xi_i,\xi_j,\chi_k),\\
X_{ijk} &= \alpha(\xi_i)\alpha(\chi_j)\alpha(\chi_k) - \alpha(\xi_i)\beta(\chi_j,\chi_k) - \alpha(\chi_j)\beta(\xi_i,\chi_k) - \alpha(\chi_k)\beta(\xi_i,\chi_j)\\
&\quad + 2\gamma(\xi_i,\chi_j,\chi_k).
\end{aligned}
$$

Then, with

$$
\begin{aligned}
I_{i,j,k,l} &= \frac{8}{81}(1 + A_i + A_j + B_k + B_l)\\
&+ \frac{2}{27}(C_iC_j + C_iD_k + C_iD_l + C_jD_k + C_jD_l + D_kD_l + J_{ij} + K_{ik} + K_{il} + K_{jk} + K_{jl} + L_{kl})
\end{aligned}
$$

$$
\begin{aligned}
&+\frac{2}{45}(E_iE_jF_k+E_iE_jF_l+E_iF_kF_l+E_jF_kF_l\\
&+E_iN_{jk}+E_iN_{jl}+E_iO_{kl}+E_jN_{ik}+E_jN_{il}+E_jO_{kl}\\
&+F_kM_{ij}+F_kN_{il}+F_kN_{jl}+F_lM_{ij}+F_lN_{ik}+F_lN_{il}\\
&+2(S_{ijk}+S_{ijl}+T_{ikl}+T_{jkl}))\\
&+\frac{2}{45}(G_iG_jH_kH_l+P_{ij}R_{kl}+Q_{ik}Q_{jl}+Q_{il}Q_{jk}\\
&+2(G_iV_{jkl}+G_jV_{ikl}+H_kU_{ijl}+H_lU_{ijk}))\\
&+\frac{14}{15}(\beta(\xi_i,\xi_j)-\alpha(\xi_i)\alpha(\xi_j)d(\chi_k)d(\chi_l)+\\
&\beta(\xi_i,\chi_k)-\alpha(\xi_i)\alpha(\chi_k)c(\xi_j)d(\chi_l)+\\
&\beta(\xi_i,\chi_l)-\alpha(\xi_i)\alpha(\chi_l)c(\xi_j)d(\chi_k)+\\
&\beta(\xi_j,\chi_k)-\alpha(\xi_j)\alpha(\chi_k)c(\xi_i)d(\chi_l)+\\
&\beta(\xi_j,\chi_l)-\alpha(\xi_j)\alpha(\chi_l)c(\xi_i)d(\chi_k)+\\
&\beta(\chi_k,\chi_l)-\alpha(\chi_k)\alpha(\chi_l)c(\xi_i)c(\xi_j))\\
&+\frac{2}{15}(W_{ijk}d(\chi_l)+W_{ijl}d(\chi_k)\\
&+X_{ikl}c(\xi_j)+X_{jkl}c(\xi_i))\\
&+112c(\xi_i)c(\xi_j)d(\chi_k)d(\chi_l),
\end{aligned}
\tag{A.32}
$$

the integral becomes

$$
I=I_{0101}-I_{0102}-I_{0201}+I_{0202}. \tag{A.33}
$$